

**Impact of Solar Proton Events
and Planetary Wave Activity on Noctilucent
Clouds**

Nabiz Rahpoe

Universität Bremen

Impact of Solar Proton Events
and Planetary Wave Activity
on Noctilucent Clouds

Vom Fachbereich für Physik und Elektrotechnik
der Universität Bremen

zur Erlangung des akademischen Grades eines

Doktor der Naturwissenschaften (Dr. rer. nat.)

genehmigte Dissertation

vorgelegt von

Dipl. Phys. Nabiz Rahpoe

aus Kabul

December 22, 2010

1. Gutachter: Prof. John P. Burrows
2. Gutachter: Prof. Otto Schrems

Eingereicht am: 23 Dec. 2010

*Tarzis',
the Giants on whom's shoulders,
I touched the sky with passion and ambition...*

Abstract

Noctilucent clouds (NLCs), also known as Polar Mesospheric Clouds (PMCs) are a rare phenomenon observed at polar latitudes during the summer season. These optically thin clouds are situated in the mesopause region at about 83 km altitude. We study the possible impact of solar proton precipitation in the Earth's atmosphere and the behaviour of the noctilucent clouds during the solar proton event. For this purpose we use SBUV/2 (Solar Backscatter Ultraviolet) NLC observations that cover the last 30 years. The proton fluxes measured by GOES (Geostationary Operational Environmental Satellite) cover the same time period. A statistical investigation between solar proton events (SPEs) and a possible depletion of NLCs is aimed at in this work. This is done for both hemispheres separately.

It is shown that solar proton events are well correlated with the depletion of NLCs. The majority of SPEs lead to significant reductions in the observed NLC residual albedo and occurrence rate time series. The extraction of the SPE forcing on the NLCs is disturbed by other forcings such as planetary wave activity, causing large scale perturbations in meridional wind circulation which can occur simultaneously. We assume, that therefore the reduction of NLCs albedo and occurrence rate during SPEs due to an increase of temperature in the mesopause region is a combination of several forcings and effects which contribute to the total variation in NLC signal.

The last part of the work is dedicated to the possible influence of planetary waves such as the 2-day wave and 5-day wave on the mesopause temperatures at mid and polar latitudes. The planetary wave (PW) signatures retrieved from the SBUV/2 and SCIAMACHY (SCanning Imaging Absorption spectroMeter for Atmospheric CHartography) NLC data are in good agreement with the observed PW signatures in temperature data from MLS (Microwave Limb Sounder). Moreover, since the NLC perturbation is mainly triggered by temperature in the mesopause region, temperature increases at polar latitudes are compared with the peak amplitudes of the PWs activity at mid-latitudes. The 2-day wave activity at mid-latitudes coincides with the temperature pulses at polar latitudes for the seasons 2004/05, 2005/06 and 2006/07. For the seasons 2007/08 and 2008/09 the 5-day wave activity at mid-latitudes is responsible for the temperature pulses at polar latitudes. Peak 2-day wave amplitudes are anti-correlated with the peak 5-day wave amplitudes at mid-latitudes. Comparison of peak amplitudes at polar latitudes show that the peak 5-day wave amplitudes are higher at polar latitudes in comparison to the 2-day wave peak amplitudes at these latitudes except for the January 2005 in the southern hemisphere. A combined forcing on temperature due to the SPE and 2-day wave activity in the summer polar mesopause region can be assumed to be responsible for the warming and massive depletion of NLCs for mid January 2005 in the southern hemisphere.

Structure of the Thesis

The thesis is divided into 6 chapters, with chapters 1 and 2 providing general overviews on the Sun and the Earth atmosphere. Instrumentation and data sets are described in chapter 3. Chapter 4 deals with properties of NLCs and in chapter 5 and 6 we present the main part of the work and its results.

Chapter 1 describes the general structure of the Sun and the coronal mass ejections (CMEs) followed by propagation of CMEs into the space accompanied by highly energetic particle precipitation in the Earth's atmosphere and its interaction with the magnetosphere.

Chapter 2 describes the atmospheric structure in general and the dynamical processes in the Earth's atmosphere. The atmospheric waves, especially the planetary and gravity waves and their important role in the Earth's atmosphere is the last topic in this chapter.

Chapter 3 deals with the description of the satellite instruments SBUV/2, SEM, MLS and SCIAMACHY and data products derived from observation with these instruments that have been used in this work. The status of the instruments, measurement characteristics and the main reason for using these data sets can be found here.

Chapter 4 gives an overview of noctilucent clouds and the results of 125 years of investigations derived from different workgroups and epochs. The NLCs and their occurrence, altitude and particle size are discussed here.

Chapter 5 is the first main part of the thesis. Here we present results of a statistical comparison between solar proton flux time series and NLC occurrence rate and albedo residual time series.

Chapter 6 The planetary wave activity of the 2-day wave and 5-day wave in temperature and NLC radiance and albedo residuals is described in Chapter 6. Here a possible impact of planetary waves on the temperature increase in the polar mesopause region is presented.

Publication List

Journal articles

- Rahpoe, N., von Savigny, C., DeLand, M., Robert, C., Burrows, J. P., 2010. Impact of Solar Proton Events on Noctilucent Clouds. *J. Atmos. Sol.-Terr. Phys.*, doi:10.1016/j.jastp.2010.07.017
- Robert, C., von Savigny, C., Rahpoe, N., Bovensmann, H., Burrows, J. P., DeLand, M., Schwartz, M. J., 2010. First evidence of a 27 day solar signature in noctilucent cloud occurrence frequency. *J. Geophys. Res.*, Vol. 115, D00I12, 12 PP., doi:10.1029/2009JD012359

Conference contribution

- Rahpoe, N., von Savigny, C., DeLand, M., Robert, C., Burrows, J. P., 2008. Impact of Solar Proton Events on Noctilucent Clouds. *37th COSPAR General Assembly, Montreal, July 2008.*
- von Savigny, C., Robert, C., Rahpoe, N., Burrows, J. P., Morris, R., Schwartz, M. J., DeLand, M. T., Petelina, S., Llewellyn, E. J., 2008. Impact of Solar Proton Events on Noctilucent Clouds. *HEPPA workshop, May 28 – 30, 2008, Helsinki.*
- Rahpoe, N., von Savigny, C., DeLand, M., Robert, C., Burrows, J. P., 2008. Impact of Solar Proton Events on the Occurrence of Noctilucent Clouds. *9th International Workshop on Layered Phenomena in the Mesopause Region, Stockholm, July 2009.*
- Rahpoe, N., von Savigny, C., Baumgaertner, A., DeLand, M., Robert, C., Burrows, J. P., 2010. Increase of summer mesopause temperature and reduction of NLC occurrence during and after enhanced quasi 2-day wave activity. *38th COSPAR General Assembly, Bremen, July 2010.*
- Winkler, H., Rahpoe, N., von Savigny, C., Burrows, J. P., Wissing, J. M., Kallenrode, M.-B., 2010. Ion-chemical impacts of solar particle events on noctilucent clouds. *38th COSPAR General Assembly, Bremen, July 2010.*

Contents

Table of Contents	1
1 The Sun and the effects of CMEs on the Atmosphere	3
1.1 The Solar Body	3
1.2 Coronal Mass Ejection	4
1.3 Solar Proton Precipitation	9
2 Structure and Dynamics of the Earth's Atmosphere	12
2.1 The atmosphere of the Earth	12
2.2 Dynamics of the Atmosphere	14
2.2.1 Geostrophic Wind	15
2.2.2 Eddy forcing in the Atmosphere	17
2.3 Atmospheric Waves	19
2.3.1 Rossby and planetary waves	19
2.3.2 Gravity Waves	21
3 Data and Instrumentation	24
3.1 SBUV and SBUV/2	24
3.1.1 Data Quality Issues	27
3.1.2 Detection algorithm for NLC	27
3.2 SEM on GOES	29
3.3 MLS on Aura	30
3.4 SCIAMACHY	31
4 The nature and characteristics of NLC	33
4.1 Occurrence rate of NLC	33
4.2 NLC season	34
4.3 Altitude of NLCs	36
4.4 Particle Size	38
4.5 Influence of the 11-year Solar Cycle on NLC	43
5 Solar Proton Precipitation and its impact on NLCs	47
5.1 Solar Proton Events	47
5.1.1 SPE and NLC reduction	47
5.2 Correlation method	50
5.2.1 Statistical Test on Correlated Time Series	51
5.2.2 Summary of Analysis	52
5.3 Results	53
5.4 Discussion	57
5.5 Conclusions	58

6	Planetary Wave Activity in the Mesopause Region	64
6.1	Introduction	64
6.2	Wave Analysis	65
6.2.1	Least Square Fitting	65
6.2.2	Application of the LSF-Method	67
6.3	Latitudinal Extent of Q2DW activity	74
6.4	Dynamical effect of PWs on Temperature variations	80
6.4.1	PW activity and Temperature increase in the Polar Mesopause . . .	80
6.4.2	Climatology of the PW Activity	84
6.5	Discussion and Conclusions	85
7	Concluding Remarks	87

Chapter 1

The Sun and the effects of CMEs on the Atmosphere

The Sun is the main source of energy that drives the dynamics of the Earth's atmosphere. In this section we introduce the Sun and the particle precipitation that leads to changes in our atmosphere. The short-term impact of the Sun's energy outbursts, the so called Coronal Mass Ejections (CMEs), which lead to acceleration of charged particles which are observed as Solar Proton Events (SPEs) on Earth is the main focus of our work. The Solar Energetic Particles (SEPs) are found to interact with the atmosphere by entering the Earth's atmosphere through the polar caps. The SEPs can lead to ionization and chemical reactions of the atmospheric species and to an imbalance of the atmospheric chemical state. In the following we would like to describe the Sun and then continue with the CMEs and SPEs and their possible impact on the Earth's atmosphere.

1.1 The Solar Body

The central star, which our planet Earth revolves around, is the main source of energy for life and the dynamical and chemical processes in the Earth's atmosphere. It is a main sequence star with a spectral classification of G2V, a surface temperature of 5226 K and luminosity of $L_{Sun}=3.86 \times 10^{33}$ ergs/s (Sackmann et al., 1993).

The variation in the Sun's luminosity and radius can be observed on short time scales of 13 days, 27 days, the 11 year scale and on large time scales of > 1000 years. At the present it has a radius of $109 \times$ Earth's radius and a mass of 1.989×10^{30} kg. It is the largest body in our solar system and contributes to 99.86% to its mass. Given the total amount of hydrogen available in the Sun and the rate of nuclear fusion of hydrogen to helium, it leads to a life time of the Sun of approximately 11 Gyr (1 Gyr = 10^9 years). At the end of its lifetime, 6.5 Gyr from now, its mass and size will change dramatically. The radius of the Sun will increase to 0.99 AU (astronomical units) and the Sun will lose 40 % of its mass. This stage of a star is classified as the Red Giant (fortunately our Earth will be then shifted to 1.69 AU). After the radiation pressure can not withstand the gravity pressure anymore the outer Helium-shell is expelled as a nebula. The free falling material is then compressed and the Sun ends up as a white dwarf with a total mass of $0.51 M_{Sun}$ (Sackmann et al., 1993) and a radius of $\approx 0.01 - 0.02 R_{Sun}$ (Shipman, 1979).

The Sun consists of several zones: the core, the radiative zone, the convection zone and the photosphere (Page and Hirsch, 1999). The high temperature in the core governs the

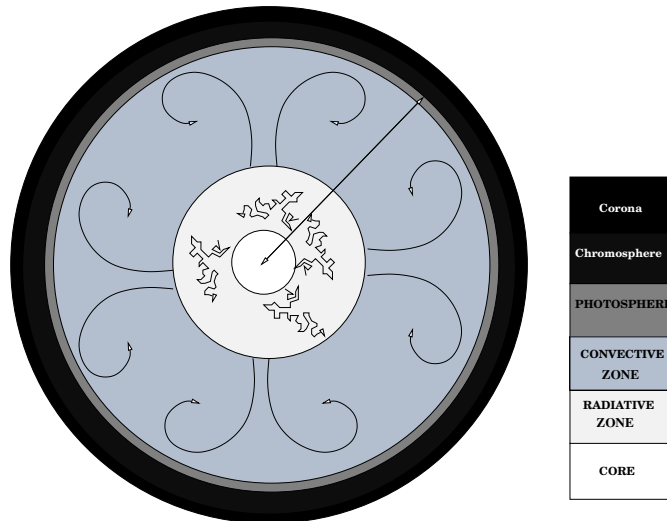


Figure 1.1: A sketch drawing of the inner structure of the Sun. The core, where the nuclear fusion takes place. The released energy then emitted and re-emitted in the radiative zone and transported by adiabatic motion of matter blobs in the convective zone to the photosphere.

nuclear fusion process. In the radiative zone, the photons produced in the core start their odyssey. In this layer, the energy transport is mainly dominated by radiative processes rather than convection, because the temperature gradient in this layer does not allow convection. In the convective zone on the other hand with a temperature of 2.02 Mio K (Cahen et al., 1986) adiabatic processes can take place which start at a radius of $0.7 R_{Sun}$. From here the heat and energy transport is established by motion of macroscopic matter blobs within a few weeks which appear as granulation on the surface of the Sun. Reaching a level where the density of the Sun falls rapidly, the energy from the convective zone is converted into radiation, which can be observed at the outer layer of the Sun which is called the photosphere. This transfer of energy by radiation leads to a constant temperature of 4000 – 5000 K. Above the photosphere the chromosphere extends its mighty bow around the Sun. The chromosphere is dominated by acoustic waves and perturbations due to outbursts from the sunspots. The outer layer of the Sun's atmosphere is the so-called corona. This layer is more a plasma-like atmosphere which is 10^{-12} times as dense as the photosphere and has temperatures of up to 10^6 K. The heat source for the corona is thought to be come from the induction of the Sun's magnetic field which can be observed as coronal magnetic loops in which ionized material is trapped. Sonic waves are also thought to be a possible source for the energy of the corona. Since the density is very low the propagation of these waves can lead to high plasma speeds and hence to conversion of kinetic energy into heat by friction (Page and Hirsch, 1999).

The most interesting phenomena in the Sun's outer layers are the coronal mass ejections (CMEs), which are thought to originate from the release of the magnetic energy of large coronal magnetic structures surrounding the sunspots and which are observed as solar flares and erupting prominences.

1.2 Coronal Mass Ejection

One of the most important processes on the Sun's 'surface' are the detachment of the energy bubbles, which are observed as either coming from flares or erupting prominences and

thought to be connected with the CMEs. These motions can build up stressed magnetic fields and Lorentz forces, which result in instability and outward movement of CMEs (Wu et al., 1991).

The massive CMEs are a result of large magnetic energy trapped in the coronal magnetic field structure. The conversion of magnetic energy into kinetic energy leads to high velocities and a wider extent of the CME in the heliolatitudinal and heliolongitudinal arc. These large flares are followed by radio spectra, light arcs and solar energetic particles (SEPs) and the conversion of released energy into kinetic and thermal forms.

A connection between the increase of solar activity accompanied with CMEs and an increase in the occurrence of magnetic storms in the Earth's magnetosphere is concluded by Tsurutani et al. (1992). A statistical study by St. Cyr and Webb (1991), who analysed various forms of solar activity with CMEs observed by SMM (Solar Maximum Mission) during the years 1984 – 1986, found that a high percentage of CMEs is associated with erupting prominences and X-ray events, which are observed as bright regions. A small number of CMEs is connected with H_α flares. By deriving the time lag between CME and flare onset, 92 cases of CMEs between June 1984 – December 1987 have been investigated (Harrison, 1991). The result is that CMEs lead the H_α flare or a X-ray event in 63 – 65 % of the cases and the flare leads the CME in 35 – 37 % of the cases. Kahler et al. (1988) found in their observation that the eruption of filaments and accompanying CMEs are not a consequence of the energy release in the flare impulsive phase or pressure pulse. They concluded that rather a global magneto-hydro-dynamic (MHD) instability in the surroundings of the flare is the main source for the CMEs.

Theoretical studies by Low (1993) indicate that the total energy required to drive a CME can only be provided due to an equilibrium between the cross-field electric currents of the detached closed magnetic fluxes and pressure or gravitational forces. Wu et al. (1983) demonstrated in a footpoint motion 2D MHD simulation the build-up of free magnetic energy in the corona by stressed magnetic fields. An example of the simulation by Wu et al. (1991) is shown in Fig. 1.2. In these plots the simulation of magnetic field lines are shown. By shearing motion out of the plane and into the plane (due to a bi-polar structure in the x-z plane) a magnetic component B_z is induced. This leads to an additional upward magnetic pressure gradient, which induces the horizontal v_x and upward v_y motions. At the beginning, the field lines will move upward due to the induced Lorentz force. At the footpoint the shearing force is zero. When the vertical speeds exceed the Alfvén speed, MHD instability occurs and the Lorentz force is now directed in upward and downward direction. The field lines are then pinched together due to downward component of the Lorentz force and an arch filament system is formed (See Fig. 1.3). Upward mass transport takes place due to vertical motion of the magnetic field lines in the first stage. This mass transport is related to the coronal mass ejection. Wu et al. (1991) concluded from these simulations, that the shearing motion can induce linear MHD instability in a cross-section between two bi-polar sun spots and because plasma velocities exceed their local Alfvén speeds (with $V_{Alfv} = \frac{B_0}{\sqrt{4\pi\rho_0}} = 4.6 \text{ km/s}$; B_0 is the magnetic field and ρ_0 the plasma density in CGS system) a nonlinear MHD instability occurs. This latter situation can be visible as a small X-ray burst which has been confirmed by the observations of CMEs by Harrison and Sime (1989).

The average speed of CMEs during the solar minimum in the years 1984 – 1986 of 73 CME cases was 237 km/s (St. Cyr and Webb, 1991). The *Skylab* NASA measurements yielded speeds on the order of 470 km/s between 1973 – 1974 which is in line with

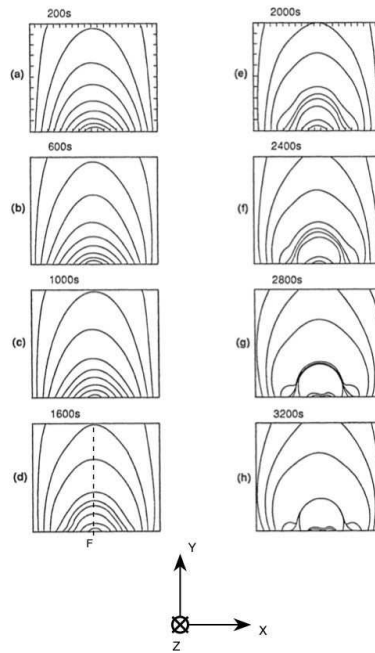


Figure 1.2: Magnetic field line evolution as a function of time (with Alfvén time $\tau_A = 1700$ s) during induced shearing motion into the z-direction (orthogonal into the plane right to the footpoint F and out of plane left to the footpoint F). At the footpoint F the shearing is zero. The x-axis represents the horizontal distance on the surface of the Sun and the y-axis is the distance from the Sun's surface in direction to the corona (Taken from Wu et al. (1991)).

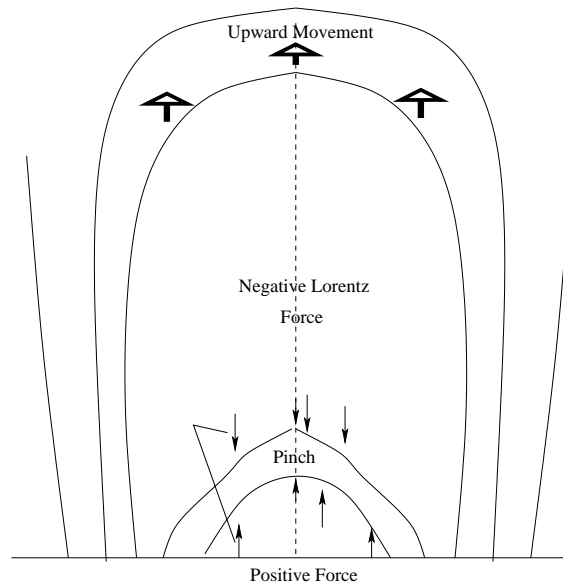


Figure 1.3: Scenario for the formation of an arch-filament system and coronal upper-level outward movement in the initial stage of a CME as a result of footpoint-shearing-induced instability. The dashed line is the position of the footpoint F as described in Fig. 1.2 (Taken from Wu et al. (1991)).

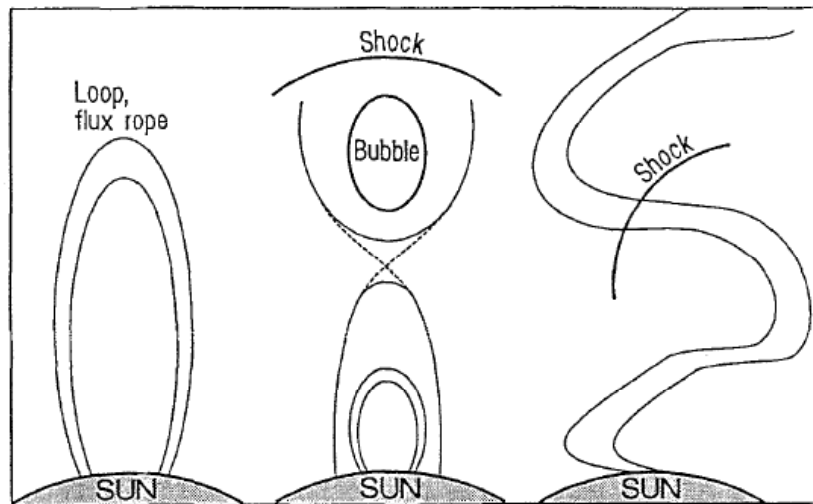


Figure 1.4: Three possible configurations for ICMEs. The envelopes are the outer magnetic field lines. (Based on summary discussions at the first SOLTIP Symposium, 30 September-5 October, 1991, Liblice, Czechoslovakia.) (Taken from Dryer (1994)).

2D simulations of CME-produced shocks by Steinolfson and Hundhausen (1990). They found that slow, intermediate and fast shocks have speeds of 200 – 300 km/s, 300 – 900 km/s and > 900 km/s respectively. The CMEs propagating into interplanetary space are referred to as the ICMEs (interplanetary CMEs) which are classified as magnetic clouds, flux ropes and bottles (Burlaga et al., 1990), as shown in Fig. 1.4 in schematic sketches. The configuration in Fig. 1.5 (upper panel) shows both ends of the ICME connected to the Sun, where the energetic particles, due to mirroring, perform streaming at one end of the loop to the other end of the plasma bubble if the ends are reconnected. A shock can build up, after the plasma interacts with the interstellar magnetic field (IMF) as shown in Fig. 1.5 (lower panel).

Kahler and Reames (1991) found that 2 MeV electrons and 22 MeV protons, with gyroradii smaller than the ICME extension have been observed during the passage of the ICME to the ISEE-2 (International Sun Earth Explorer) spacecraft and found that the solar energetic particles (SEPs) were connected to the Sun. Several calculations and 3D simulations of ICME shocks in the interplanetary magnetic field showed, that there are several possibilities for building of magnetic trapping regions and mirroring of the particles within the ICME. Thus the precipitating highly energetic particles observed in the magnetosphere between the Earth and the Sun are a result of combined effects of SEPs and shock-accelerated energetic storm particles (ESPs) (Sanahuja and Heras, 1992).

These accelerated highly energetic particles that propagate into the interstellar medium with speeds of up to 3000 km/s (Dryer et al., 1984) can lead to perturbations in the Earth's magnetosphere and enter the Earth's atmosphere through the magnetic poles. This impact is related to the solar proton events (SPEs) observed at high latitudes.

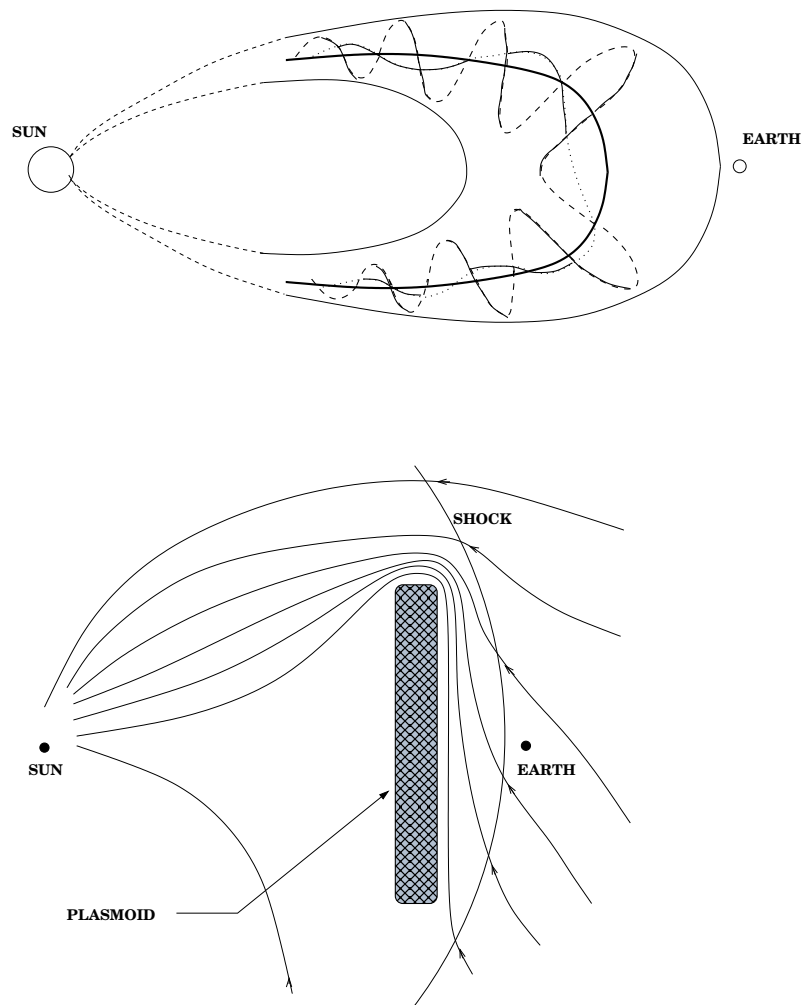


Figure 1.5: Idealized, cartoon sketches of interplanetary coronal mass ejections (ICMEs) as either a loop or flux rope (top panel; Adopted from Burlaga et al. (1990)), or plasmoid with draped interstellar magnetic field (IMF) lines (bottom panel; Adopted from McComas and Gosling (1988)).

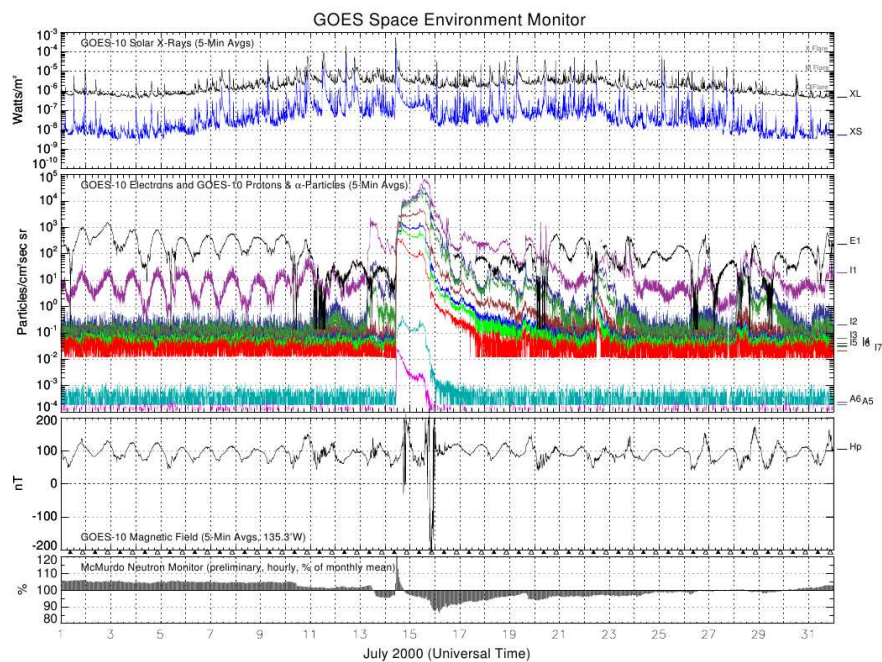


Figure 1.6: Intensity plot of different parameters recorded by GOES – 10 satellite onboard the SEM for the month July 2000 (Taken from: <http://goes.ngdc.noaa.gov/data/plots/2000/>).

1.3 Solar Proton Precipitation

Solar proton events (SPEs) associated with the activity in the Sun’s atmosphere, mainly due the CMEs, are a phenomenon observed in the polar cap region of the Earth’s atmosphere. An example of solar flares followed by a solar proton event recorded near the Earth from a geostationary orbit with the GOES – 10 satellite (Geostationary Operational Environmental Satellite) is shown for July 2000 in Fig. 1.6. In this plot the so-called Bastille Day Storm can be observed starting on July 14 associated with peak signals in X-ray emission, magnetic field perturbation, flux of highly energetic protons, electrons, α -particles and neutrons. If an ICME is in the transmission crossing sector between the Sun and Earth, these particles can enter the Earth’s atmosphere through the magnetic poles by following the magnetic field lines (Patterson et al., 2001). During the years 1976 – 2006 a total of 222 SPEs with different energies and flux ranges have been recorded (Verronen et al., 2007). Different energies lead to different energy deposition altitudes of the SEPs in the atmosphere.

The deposition of precipitating highly energetic particles leads to dissociation and ionization of the chemical species due to secondary electrons as described by Crutzen et al. (1975). He determined the production of NO_x during the SPEs of Nov. 1960, Sep. 1966 and Aug. 1972. The increase in NO_x was mainly due to dissociation of N_2 by the secondary electrons which have been produced during the precipitation of energetic particles. Nitric oxide is then formed via the reactions of ionized and dissociated nitrogen with oxygen and ozone molecules. A schematic sketch of the relevant chemical reactions is shown in Fig. 1.7. Similar processes were found for the production of odd hydrogen ($\text{OH}+\text{H}$) during solar proton events (Solomon et al., 1981). By ionization of the major constituents like O_2 , which can combine with water vapor and water vapor complex chains, a net outcome

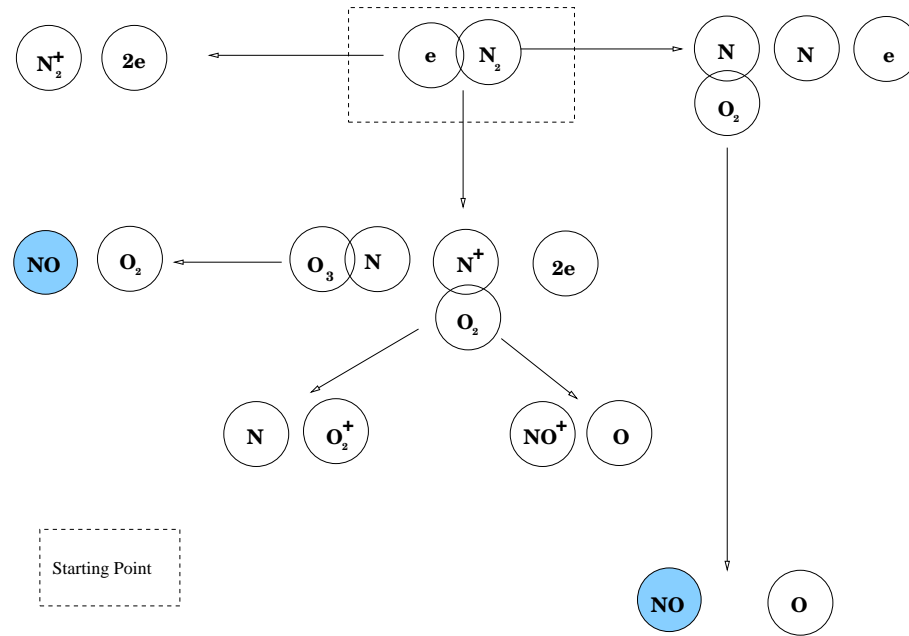


Figure 1.7: A sketch of the possible chemical reactions for the N_2 molecule due to secondary electrons (starting point) and production of NO_x (shaded circles) (Adapted from Crutzen et al. (1975)).

of odd hydrogen is produced (Fig. 1.8). The catalytic NO_x and HO_x ozone destruction cycles are found to be the main sinks of ozone in the stratosphere and mesosphere during and after SPEs (Weeks et al., 1972; Swider and Keneshea, 1973; Crutzen et al., 1975; Solomon et al., 1983; Jackman and McPeters, 1985).

Further investigation and observation for different SPEs based on measurements and numerical simulations showed that disturbances in the chemical balance during SPEs can lead to severe ozone depletion in the stratosphere and lower mesosphere (McPeters et al., 1981). Note, that the effect of SPEs on the total ozone column is rather small, and will generally not exceed 1%. Recently model simulations of possible dynamical and thermal effects of SPEs followed by strong ozone depletion for the July 2000 SPE (Bastille Day Storm) (Jackman et al., 2001; Krivolutsky et al., 2006) and October 2002 SPE (Halloween Event) (Jackman et al., 2007) have been established and discussed. The qualitative result is that due to ozone depletion followed by cooling of lower polar mesosphere, a warming in the polar summer mesopause region is induced due to dynamical processes. Verronen et al. (2007) found a dependency of the latitudinal extent of solar proton forcing in the polar cap region due to shifting of the geomagnetic cutoff rigidity threshold for the January 2005 SPE using hydroxyl measurements. Simulations with a mechanistical model (KMCM: Kühlungsborn Mechanistic general Circulation Model) by Becker and von Savigny (2010) showed changes of the gravity wave drag in the mesopause region associated with a deceleration of the zonal wind. The chain of effects proposed and tested by Becker and von Savigny (2010) is as follows:

By depletion of ozone the established meridional temperature gradient in the upper stratosphere and lower mesosphere is disturbed. The change in meridional temperature gradient leads to weakening of the zonal mean wind. Since the mean zonal wind and residual meridional circulation are connected with each other, this leads to weakening of the residual

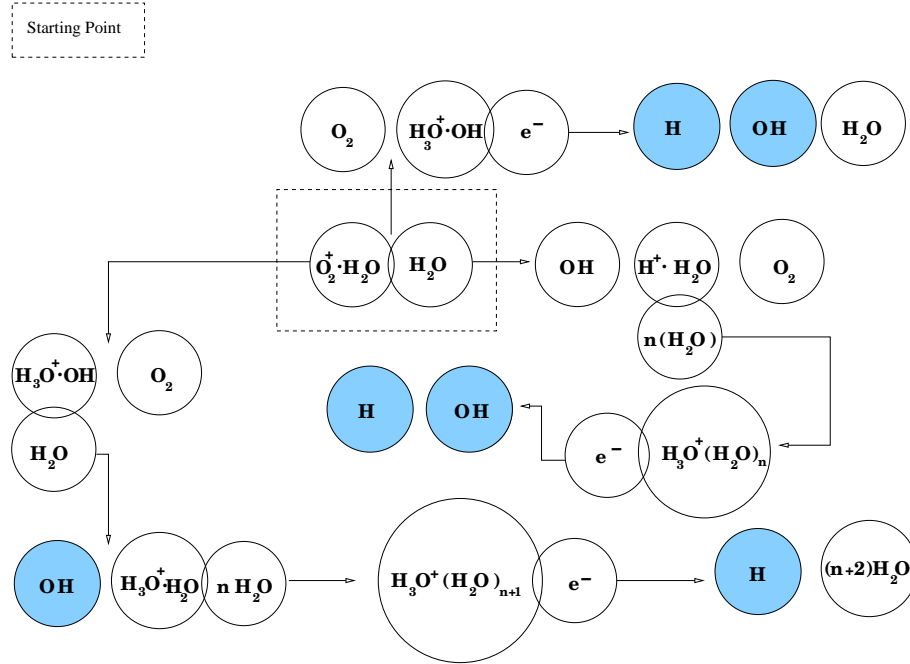


Figure 1.8: Same as Fig. 1.7 but for the production of HO_x during the solar proton event. (Adopted from Solomon et al. (1981)).

meridional circulation in the mesosphere. The prior established vertical upwelling at the polar summer mesopause is reduced and therefore the adiabatic cooling of the polar summer mesopause region decreases. Consequently, a warming of the polar summer mesopause region is expected due to reduced dynamical heating (See Chapter 2.2 for better understanding).

In an earlier study von Savigny et al. (2007a) investigated the massive reduction in NLC occurrence rate in the southern hemisphere during the SPE of January 2005 using the SCIAMACHY limb measurements. They found that NLC occurrence rate and temperature in the mesopause region were anti-correlated with a cross correlation coefficient of $r \approx -0.6$ for different latitude bands. A temperature increase of 2K/day at the southern polar mesopause has been observed for a period of 6 days during the SPE. Their conclusion was, that Joule heating due to ionization and dissipation at the NLC heights was the main reason for the NLC reduction. These chemical and dynamical processes initiated by the precipitation of SEPs leads to a warming of the polar mesopause region. Meteoric smoke particles will not be affected, but the NLC particles sublimate.

Given these facts, we expect that solar proton events should impact the NLCs as mentioned above in this manner. This is the main reason to search for a connection between the occurrence of SPEs during the NLC season and a possible depletion of NLCs during or shortly after a solar proton event, which is one of the main aims of this study. The question will be how strong does an impact of an SPE could affect the mesopause region. We hope to be able to answer this question which is the main topic in chapter 5.

We can summarize that solar proton events are a part of the external forcing in the upper atmosphere, and beside the observed and predicted significant effects on the chemical balance in the Earth's atmosphere, they should have a dynamical and thermal impact in the mesopause region as well.

Chapter 2

Structure and Dynamics of the Earth's Atmosphere

In this chapter we want to provide an overview of the Earth's atmosphere and its structure. Then we will give a description of the dynamics and its importance. In the last part we will provide a background on planetary waves especially the Rossby waves and gravity waves, which are important for understanding the last chapter of this work. A descriptonal and general approach is aimed at and therefore we recommend the reader to use the references for further and detailed understanding.

2.1 The atmosphere of the Earth

The atmosphere of the Earth consists of three major constituents: molecular nitrogen N_2 , molecular oxygen O_2 and argon Ar which can be found in precentages of 78.1%, 20.9% and 0.9% (Frederick, 2008). The trace gases which make up a total of 0.1 % are mainly carbon dioxide CO_2 with 0.0380 % and ozone O_3 of about 8×10^{-4} % at 30 km. These small but important quantities of trace gases play a major role in the chemistry and the radiative equilibrium of the atmosphere.

The pressure force on an air parcel for a given height is dependent on the total differential pressure above and below it. If the total force is zero the gravity force and pressure must be in equilibrium. We can write for a given altitude the following hydrostatic balance equation:

$$P(h) - P(h + dh) - mg/A = 0 \quad (2.1)$$

$P(h)$ is the pressure for a given altitude h and g the acceleration due to gravity, m is the mass of the air parcel and A its normal surface. We can expand the equation for the mass $m = M \cdot n \cdot dV = M \cdot n \cdot A \cdot dh$ with dV being the volume of the air parcel and M and n the molar mass and mole density of the air into:

$$dP = -M \cdot g \cdot n \cdot dh \quad (2.2)$$

where, dP is the differential pressure and dh the thickness of an air parcel respectively. Applying the ideal gas law for number density n and by using equation (2.2):

$$n = \frac{P}{R \cdot T} \implies \quad (2.3)$$

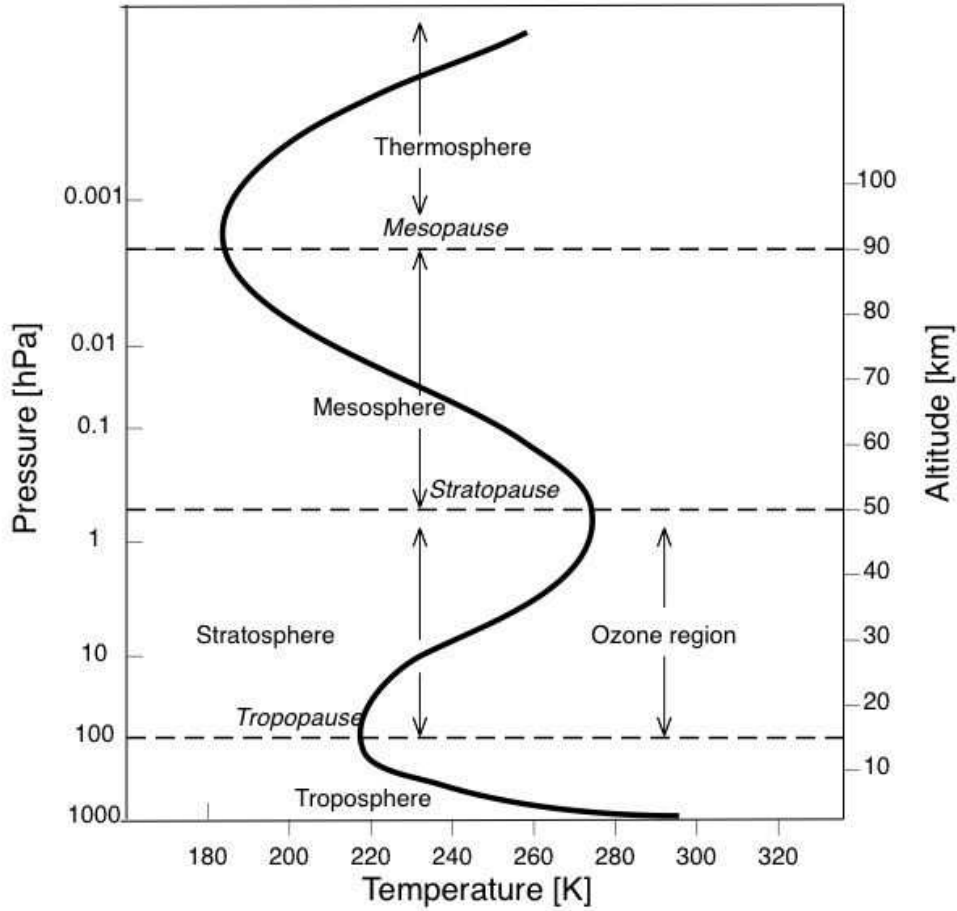


Figure 2.1: Vertical thermal structure of Earth's atmosphere up to 120 km (Adapted from Brasseur and Solomon (1984)).

$$\frac{dP}{P} = -\frac{M \cdot g \cdot dh}{R \cdot T} \quad (2.4)$$

By assuming a constant temperature, constant acceleration due to gravity and no change in density for an infinitesimally thin layer, one can derive the following equation by integrating the equation (2.4):

$$P = P_0 \cdot e^{-h/H} \quad (2.5)$$

where $H := \frac{R \cdot T}{M \cdot g}$ is denoted scale height and is dependent on temperature. A typical average scale height for the troposphere and stratosphere is ≈ 7 km. The pressure is reduced exponentially with altitude in an isothermal atmosphere. To construct a pressure or density profile, one needs to know the temperature profile. For each pressure layer, one can then assume a constant temperature for this layer and construct step by step the unknown pressure or density.

The atmosphere is divided into distinct layers that resemble the structure of the temperature profile as shown in Fig. 2.1. In this plot the troposphere, stratosphere, mesosphere and thermosphere are shown. The transitions from one layer to the other are

defined as pauses, which coincide with zero vertical temperature gradient. The temperature decreases with altitude (negative lapse rate) in the troposphere and mesosphere and increases in the stratosphere and thermosphere. The unexpected increase in temperature in the stratosphere is explained by absorption of solar ultraviolet (UV) radiation by ozone in the ozone layer ($\approx 20 - 50$ km). On the other hand the intense solar radiation and photolysis of N_2 and O_2 leads to high temperatures in the thermosphere (Mohanakumar, 2008). A given temperature gradient determines whether the atmospheric region is vertically stable or not. If Γ_d is the adiabatic lapse rate for a dry atmosphere (Γ_d is 10 K/km for the Earth's atmosphere) then a given atmospheric region is stable for $-dT/dz < \Gamma_d$ and it is unstable for $-dT/dz > \Gamma_d$ (Houghton, 2002).

Since 99 % of water vapor is contained in the troposphere, the major part of the weather including clouds, storms and precipitation takes place in this layer. The tropopause marks the first minimum in the temperature profile and its position is dependent on the latitude and ranges from ≈ 16 km at the equator to about 8 km in polar regions. As the zero temperature gradient prevents vertical motion, the moist water vapor is trapped in this region and less mixing of air takes place between the troposphere and stratosphere. The tropopause is followed by the stratosphere which extends up to an altitude of about 50 km before the stratopause is reached. In this layer the presence of ozone leads to absorption of UV radiation which leads to an increase of temperature. The stratosphere can reach temperatures as at the surface of the Earth of up to 275 K. The positive lapse rate leads to warmer air parcels above the colder air parcels. This inversion leads to stable conditions that prevents convection and upward motion and thus even distinct aerosol layers can exist and last for a long time.

The mesosphere is the layer above the stratopause, where the temperature lapse rate changes its sign. The lowest temperatures in the Earth's atmosphere are observed in mesosphere namely near the polar summer mesopause. The lower concentration of ozone together with gravity wave activity in the mesosphere leads to temperatures dropping as low as 130 K at the polar summer mesopause (Gadsden, 1982) and can lead to deposition of water vapor into ice and building of ice particles which are observed as noctilucent clouds in the polar summer mesopause region.

The thermosphere is the layer above the mesopause region and is characterized by a positive lapse rate and high temperatures. The thermosphere which includes the ionosphere extends vertically some hundreds of kilometres. The density in this region is very low and due to high solar radiation the oxygen O_2 and nitrogen N_2 can be photodissociated. Temperatures of up to 500 – 2000 K are observed because the X-ray radiation can lead to ionization as well as heating.

2.2 Dynamics of the Atmosphere

Our atmosphere is heated more at lower latitudes and less at higher latitudes due to the spherical shape of the planet Earth and an angle of only $\approx 23.5^\circ$ between the equatorial plane and the ecliptic. The tilted rotation axis of the Earth toward the ecliptic plane is responsible for the occurrence of seasons. The meridional temperature gradient caused by difference in solar insolation leads to large-scale circulation in the atmosphere. In the troposphere in the equatorial region convection takes place, followed by subsidence of air at midlatitudes. Due to upward movement of air at polar latitudes and mass continuity there is a meridional poleward movement of air in the lower troposphere and an equatorward wind in the higher troposphere at midlatitudes. These two circulations in the troposphere

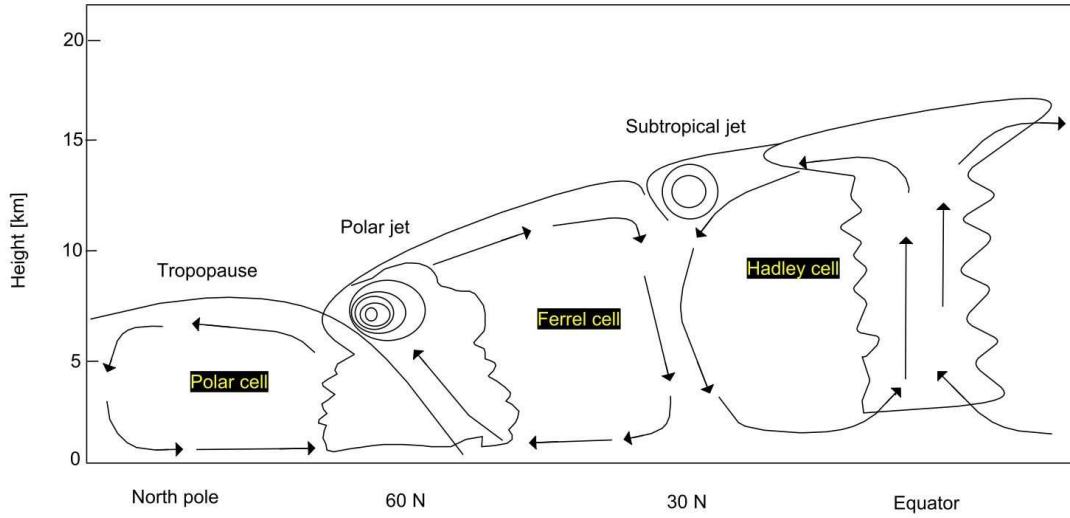


Figure 2.2: Positions of jet streams in the meridional circulation (Adapted from National Weather Service).

are called the Hadley cell and Ferrel cell respectively (See Fig. 2.2). In the upper summer stratosphere the higher latitudes are heated more in comparison to the winter stratosphere due to continuous solar illumination and absorption of UV radiation due to ozone in these altitudes. One expects higher temperatures in the summer mesosphere compared to winter mesosphere due to radiation as well. The difference between the summer mesosphere temperature distribution and winter mesosphere is shown in Fig. 2.3. Here we can see that the observations show large differences from the purely radiative situations, especially in the upper polar mesosphere. The reason for the observed temperature departure of the atmosphere at polar latitudes from a purely radiatively driven atmosphere and temperature distribution is the presence of the large scale residual meridional circulation (Dunkerton, 1979).

2.2.1 Geostrophic Wind

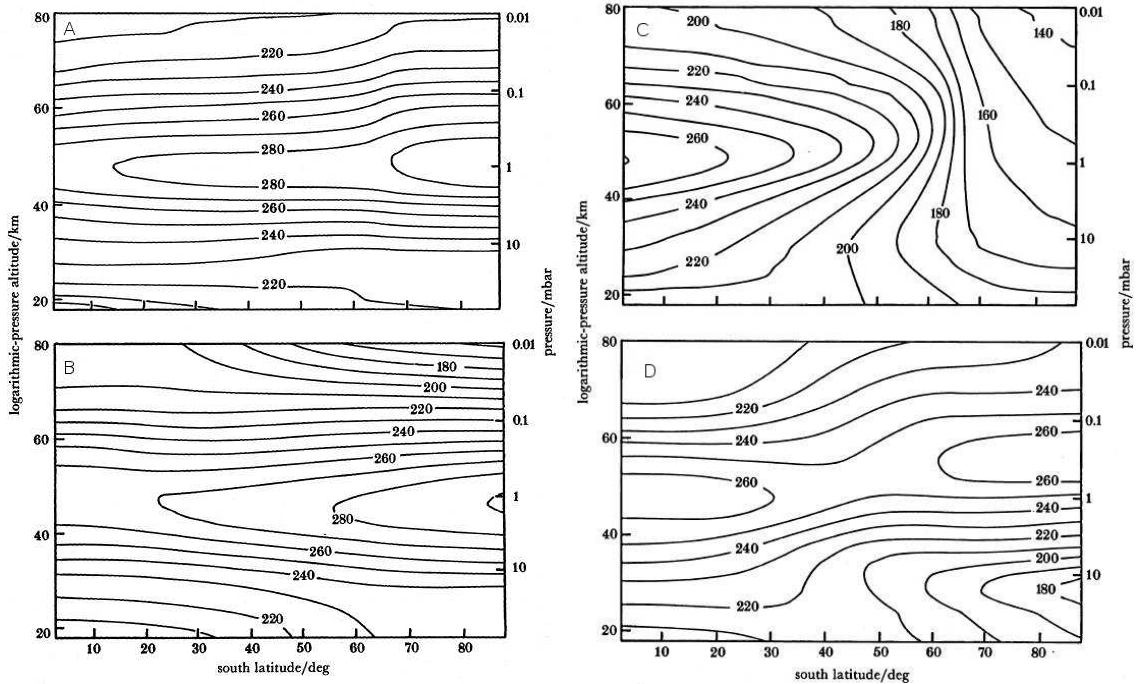
The latitudinal temperature gradient is the main source for the pressure gradient force. Since the Earth presents a rotating reference frame, any atmospheric motion will be affected by the Coriolis force. The balance of the pressure gradient force and the Coriolis force leads to the horizontal geostrophic wind if there is no friction (Fig. 2.4). The geostrophic wind equation in the zonal and meridional components can be written as

$$u_g = -\frac{1}{\rho \cdot f} \frac{\partial p}{\partial y} \quad (2.6)$$

$$v_g = +\frac{1}{\rho \cdot f} \frac{\partial p}{\partial x} \quad (2.7)$$

p is the pressure, f is the Coriolis parameter and ρ the mass density of an air parcel (Andrews et al., 1987a; Roedel, 1992; Holton, 2004; Pidwirny, 2006). The thermal wind can be written in terms of the geostrophic wind by using the hydrostatic equation:

$$\frac{\partial \vec{V}_g}{\partial \ln p} = -\frac{R}{f} \cdot \vec{k} \times \nabla_p T \quad (2.8)$$



(a) A: Radiatively determined summer solstice temperatures. B: Summer solstice temperature observation.

(b) C: Radiatively determined winter solstice temperatures D: Winter solstice temperature observation

Figure 2.3: Difference between pure radiative equilibrium (A and C) for the Earth’s atmosphere and real observed temperature (B+D) distribution (Adapted from Andrews (1987)).

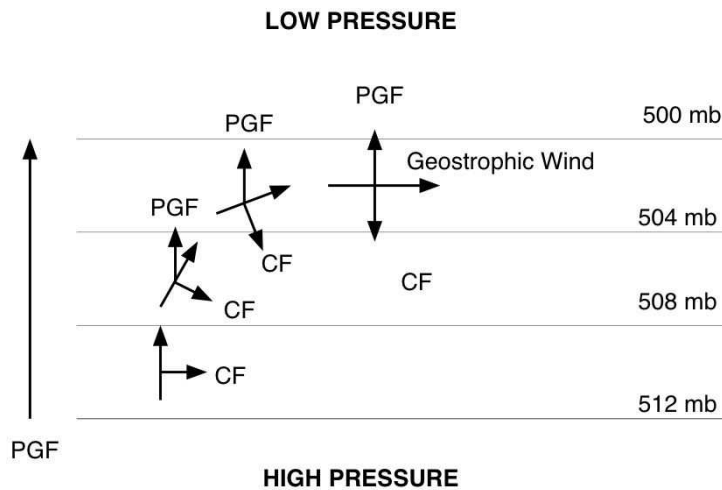


Figure 2.4: Geostrophic wind flow parallel to straight isobars, which is maintaining the balance between horizontal pressure gradient force (PGF) and the Coriolis Force (CF) (Adapted from Pidwirny (2006)).

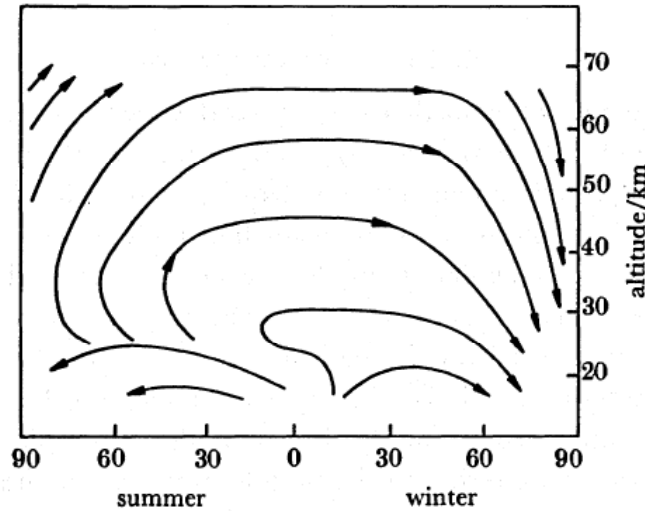


Figure 2.5: Schematic streamlines of the solstice diabatic circulation in the middle atmosphere (Adapted from Dunkerton (1979)).

with the pressure p , the gas constant R and k being the normal vector to the plane. The thermal wind originates from a horizontal temperature gradient $\nabla_p T$. The zonal and meridional components of the thermal wind (u, ν) are then defined as (Holton, 2004):

$$\frac{\partial u_g}{\partial \ln p} = \frac{R}{f} \left[\frac{\partial T}{\partial y} \right]_p \quad (2.9)$$

$$\frac{\partial \nu_g}{\partial \ln p} = -\frac{R}{f} \left[\frac{\delta T}{\delta x} \right]_p \quad (2.10)$$

The consequence of a temperature gradient are the zonal and meridional winds.

2.2.2 Eddy forcing in the Atmosphere

Another description of the Earth's dynamics is based on the Eliassen-Palm theory that describes the interaction of excited waves and eddies with the mean zonal flow. The Eliassen-Palm (EP) flux \vec{F} is a measure of internal forcing of the mean state of the disturbances that is dependent mainly on zonal and meridional winds (Eliassen and Palm, 1960). The consequence of $\nabla \cdot \vec{F} = 0$ (zero EP-flux divergence) is the steady mean state which is also denoted as non-acceleration theorem (Charney and Drazin, 1961). This implies that zonal mean flow is steady, the residual meridional ν^* and residual vertical w^* velocities are zero. This is the case for strictly conservative eddy and steady mean flow.

Adiabatic motions of air parcels together with EP-flux divergence and convergence leads to residual circulation. Without the eddies and wave excitations there will be no divergence of the EP flux and no drag will occur on the mean flow.

The eddies drive the atmosphere away from thermal equilibrium in this manner. The non-radiative equilibrium is observed in the polar winter stratosphere and summer and winter mesosphere (Andrews, 1987). A model calculation of radiative and non-radiative observations of temperature distribution is shown in Fig. 2.3.

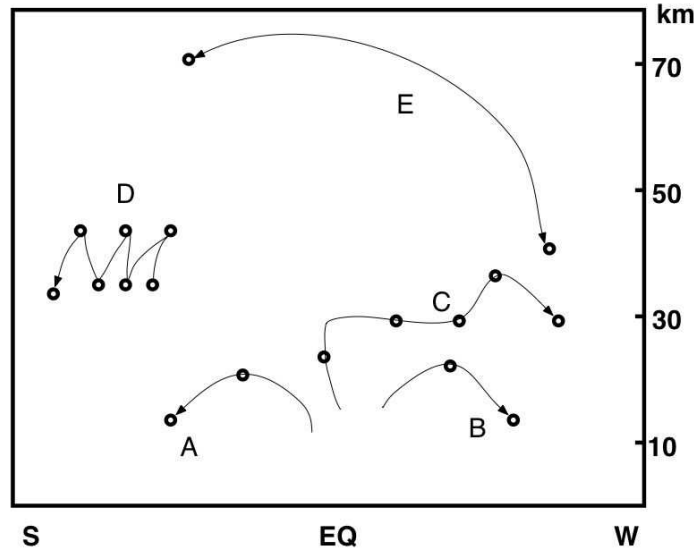


Figure 2.6: Representative trajectories (model) for the stratosphere and mesosphere. Circles indicate position after six-month periods. S and W refer to initial solstice condition (Adapted from Dunkerton (1979)).

In the winter and summer hemisphere, the internal gravity waves (buoyancy) propagate from the troposphere into the mesosphere and deposit their energy by wave breaking. An analogy can be seen with water surface waves near the coast, where the amplitude of the waves increases because of the dispersion relation due to decreasing water depth and the amplitude of the wave decreases by depositing its kinetic energy at the coastline. The deposition of energy due to gravity waves slows down the zonal mean wind. From the stationary mean zonal mean momentum equation:

$$-f \cdot \nu^* = G \quad (2.11)$$

where G is the wave drag force per unit mass and ν^* the residual meridional velocity, one can deduce the change on zonal mean flow due to change of ν^* and wave drag in the upper stratosphere and mesosphere. The geostrophical readjustment leads to the large scale residual meridional circulation.

In the northern winter hemisphere with $f > 0$ the wave drag will be $G < 0$ and thus westward. The residual meridional velocity must be > 0 , which implies a negative residual vertical velocity at high northern latitudes due to continuity, and air descends and warms. In the southern hemisphere the opposite is the case which corresponds to a northward drift and hence ascending air and cooling above the pole (Fig. 2.5). This explains the warm polar winter mesosphere and cold polar summer mesosphere. The latter is the main reason for polar summer mesopause temperatures dropping below 150 K and for the formation of noctilucent clouds (NLCs).

Generally one can say that the summer to winter pole meridional residual circulation in the stratosphere and mesosphere leads to departure from radiative equilibrium. Without the large scale meridional circulation there will be no transport of trace gases from one pole to the other and no upwelling of stratospheric and mesospheric water vapor to the polar summer upper mesosphere where NLCs can form. The first attempt to model the transport of trace gases, that led to the formulation of Lagrangian mean flow, is shown in

Fig. 2.6. Due to the residual circulation the air parcels are found in the other hemisphere after 6 months in the mesosphere which are then transported down to the stratosphere at high latitudes in the winter hemisphere (Dunkerton, 1979).

2.3 Atmospheric Waves

A general wave in the x-direction is defined as follows (Beer, 1974):

$$A(t, x) = A_0 e^{i(kx - \omega t)} \quad (2.12)$$

where A is the wave function, A_0 is the amplitude, k the wavenumber, ω the frequency and $(kx - \omega t)$ the phase. The wave crests and troughs propagate through the fluid medium at a speed called the phase speed ω which is defined by

$$c_x = \frac{\omega}{k} \quad (2.13)$$

where we can define the wavenumber k as $k := \frac{2\pi}{\lambda_x}$ through its wavelength λ_x . On the other hand the kinetic energy of a wave propagates with the group velocity

$$v_g = \frac{\partial \omega}{\partial k} \quad (2.14)$$

In a nondispersive wave, the phase velocity of the individual wave crests is equal to the group velocity. The classification of atmospheric waves is made according to their physical or geometrical properties. Forced waves must be maintained by excitation mechanisms, while the free waves do not. For example, the thermal tide due to diurnal fluctuation in solar heating is a forced wave, while the free waves are a group of global normal modes. Another class of atmospheric waves are evanescent or trapped waves which can only propagate in a given direction. For example horizontally propagating planetary waves are trapped in the vertical. The same is for the equatorial Kelvin waves which are trapped at higher latitudes.

2.3.1 Rossby and planetary waves

C. G. Rossby explained the wave patterns in the weather system in the early 40s of the last century. The main cause of the Rossby waves is the latitudinal (north-south) gradient of potential vorticity or the latitudinal dependence of the Coriolis parameter (Rossby, 1940). *'If there were no latitude variation of the Coriolis force, then Rossby waves would degenerate into a geostrophic wind: one in which the Coriolis force and the pressure gradient are in equilibrium'* (Beer, 1974). Those waves that are generated by large-scale surface topography like the Rocky Mountains or the Himalaya-Tibet complex are called forced stationary planetary waves. Such waves propagate upward when eastward zonal winds are weak and deposit their momentum in the stratosphere. The dispersion relation for the Rossby waves is defined as follows (Beer, 1974):

$$\omega = Uk - \frac{\beta}{k} \quad (2.15)$$

with U being the mean zonal wind speed, k the wave number and β the latitudinal Coriolis parameter derivative $\beta := \frac{\partial f}{\partial \phi}$.

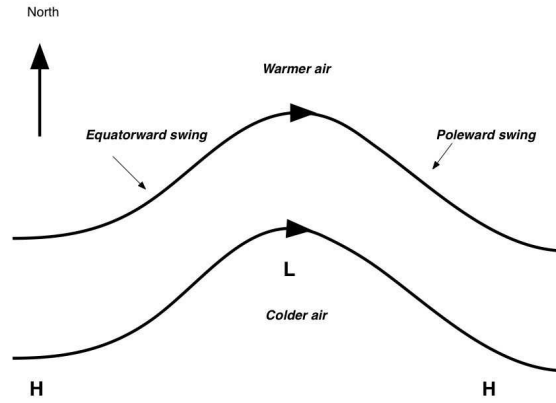


Figure 2.7: Propagation characteristics of Rossby waves in the southern hemisphere (Adapted from J. Brandon).

The phase speed of the Rossby waves can be written as

$$c_x = U - \frac{\beta}{k^2} \quad (2.16)$$

Since the sign of the relative wind speed $c_x - U$ is negative, the zonal propagation of Rossby waves is always westward relative to the mean zonal wind. As in Fig. 2.7 the Rossby waves are established if a meridional displacement of the zonal flow occurs and the result is a sinusoidal motion, which gives decreased vorticity for the equatorward swing (anti-cyclonically curved flow) and increased vorticity for the poleward swing (cyclonically curved flow) (Rossby, 1940). Since $\beta > 0$ in the northern hemisphere the zonal phase speeds of Rossby waves are $c_x < U < 0$ and therefore they propagate westward relative to the mean wind. In a quiescent atmosphere Rossby waves travel westward with a wave speed c_x , dependent on the wavelength:

$$c_x = -\frac{\beta\lambda^2}{4\pi^2} \quad (2.17)$$

It should be noted that the forced Rossby waves can only propagate westward, while the free Rossby waves can propagate in both directions. An example of free Rossby waves in the upper stratosphere and mesosphere with wavenumber 3 and a period of 2 days is shown in Fig. 2.8. The propagation of the local maxima of the potential vorticity in this plot can be observed, e.g. as a periodic temperature variation of a fixed location with a period of 2 days. For vertical propagation of Rossby waves, the Charney-Drazin criterion is used where the condition $0 < U - c < U_c$ must be fulfilled. Thus the background wind must be eastwards and less than c for Rossby waves to propagate vertically (Charney and Drazin, 1961). In addition only Rossby waves with large wavelengths > 4000 km are allowed for vertical propagation. The critical speed U_c for large scale planetary waves can be approximated by (Mohanakumar, 2008):

$$U_c = \frac{110}{S^2 + 3} [m/s] \quad (2.18)$$

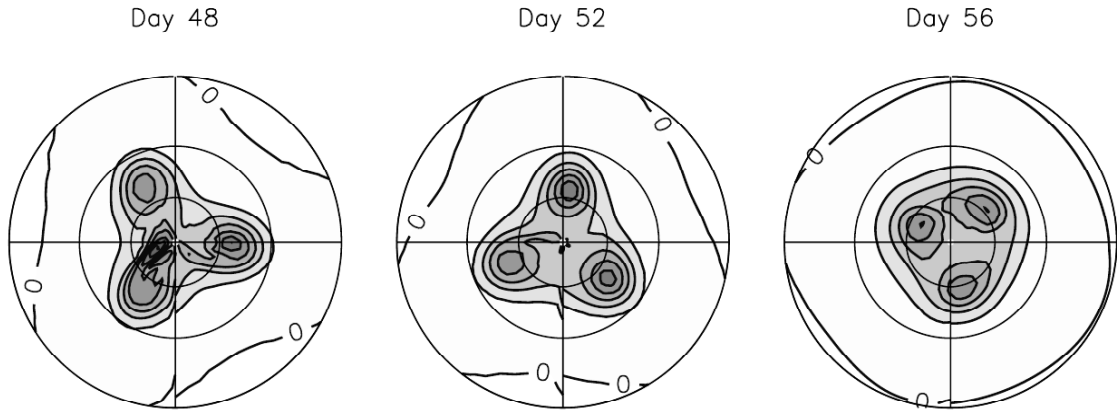


Figure 2.8: An example of 2-day wave with wavenumber 3 showing the potential vorticity from SMM integration (dark areas correspond to higher PV with contours every 3 PVU: $\text{PVU} = 10^{-6} \text{m}^2 \text{s}^{-1} \text{Kkg}^{-1}$) using a stereographic projection for the northern hemisphere, circles at 30° , 60° and 90° latitude, respectively (Adapted from Rojas and Norton (2007)).

where S is the zonal wavenumber. Thus stationary Rossby waves with $S=1$ and $S=3$ propagate in westerlies of $U_c < 28$ m/s and $U_c < 9$ m/s respectively. Weakening of the mean zonal flow leads to propagation of Rossby waves in the upper atmosphere (McLandress et al., 2006).

Another exotic class of the planetary waves that can propagate vertically up to the mesosphere are those with normal modes. The prominent candidate of these normal mode planetary waves are 2-day, 5-day, 10-day and 16-day waves. As described by Lieberman (1999), McLandress et al. (2006) and Salby and Callaghan (2008) the source of excitation of 2-day waves is the instability of the background state that generates unstable normal modes that grow in time (Salby and Callaghan, 2003). Due to strong shear in the easterly zonal mean winds in the summer hemisphere 2-day waves can be excited in-situ in the mesosphere and propagate up to the higher altitudes. As proposed by Plumb (1983) the zonal mean easterlies near solstice are baroclinically unstable. They observed this in the annual amplification of 2-day wave which is thought to be related to annual instability of the summer easterly jet. The 2-day wave can break in the upper mesosphere but deposit its momentum in opposite direction to the gravity wave drag and therefore resulting in acceleration of the zonal mean flow, which leads to weakening of meridional circulation and warming of the mesopause region at the end of the summer solstice (Norton and Thuburn, 1996).

2.3.2 Gravity Waves

Gravity waves or buoyancy waves are induced if an air parcel is displaced in the atmosphere. The gravity force tries to restore the initial position of the air parcel. The result is an oscillation of the air parcel about the equilibrium state. Gravity waves can also be generated by air flow over mountain system and the amplitude increases exponentially as they propagate vertically to higher altitudes (Beer, 1974). The zonal mean flow is the mechanism which is responsible for the vertical filtering of gravity waves in the upper mesosphere. A sketch plot is shown for allowed upward propagation of gravity waves in summer and winter (Fig. 2.9). The filtered waves are with velocities of $c_x > U$ in the

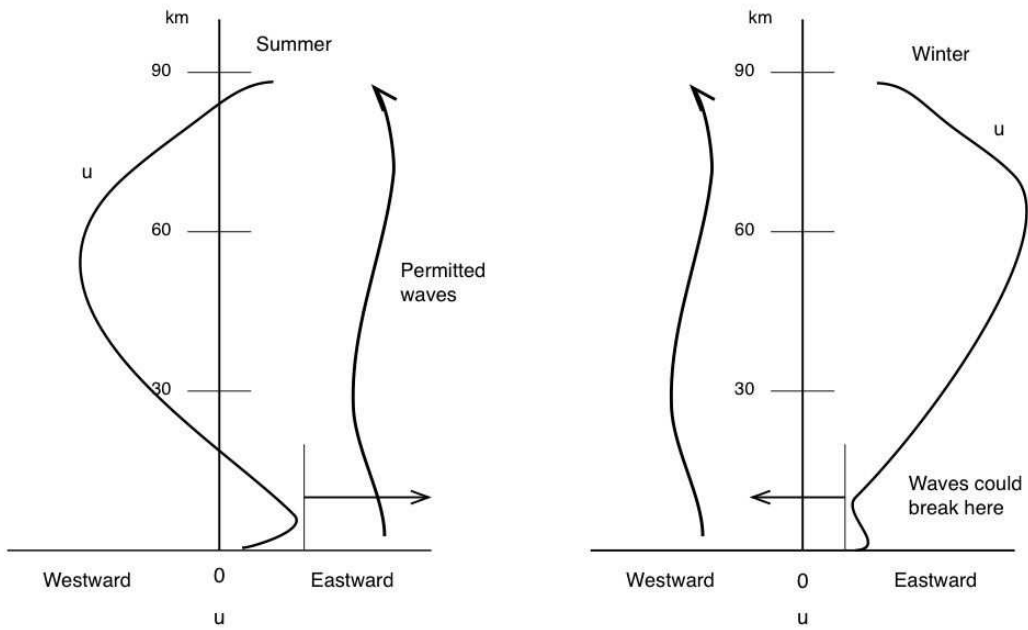


Figure 2.9: Condition for the vertical propagation of gravity waves (Adapted from Andrews et al. (1987a)).

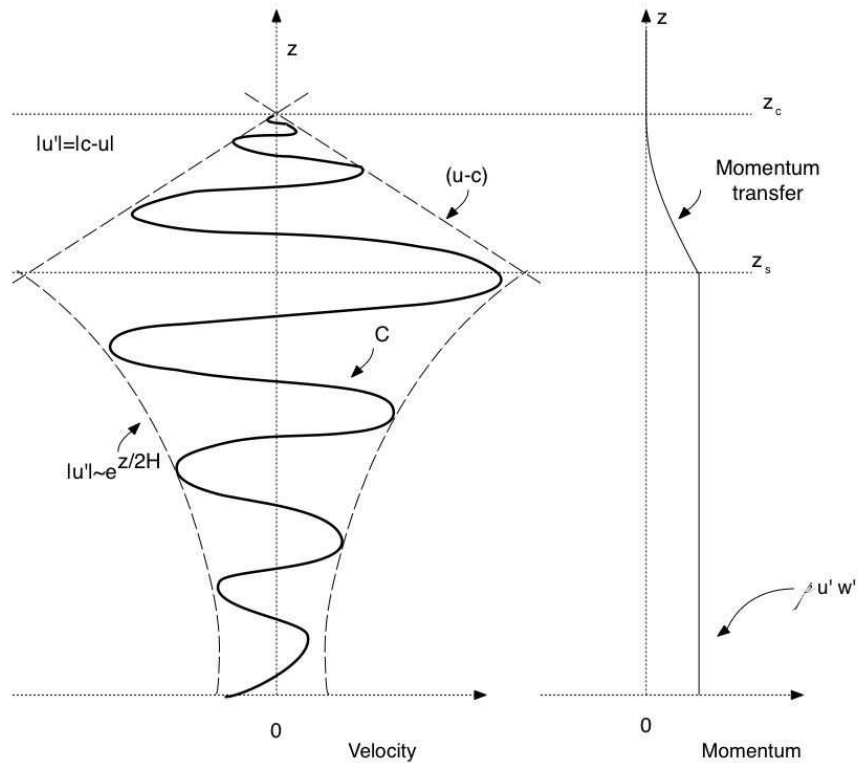


Figure 2.10: Illustrating the behaviour of a gravity wave as it propagates upward into the mesosphere. When at saturation level z_s , the amplitude of the horizontal velocity of the wave reaches $(u - c)$, c being the phase velocity of the wave and u the velocity of the mean zonal flow, saturation of the wave is said to occur and momentum transfer from the wave to the mean flow begins to take place, until the critical level z_c is reached where $(u - c) = 0$ (Adapted from Fritts (1984)).

summer, but $c_x < U$ in the winter. The vertically propagating waves typically break in the upper mesosphere since their amplitudes increase exponentially with altitude (Fig. 2.10). The wave breaking leads to deposition of their momentum and energy in the saturation zone where it leads to deceleration or acceleration of the mean zonal flow.

Chapter 3

Data and Instrumentation

In this chapter we will describe the data and instruments used for this work. These datasets are the backbone of our analysis. The main part of this work is based on the SBUV/2 data in order to investigate possible SPE effects and planetary wave signatures in NLCs. In the following parts of this chapter we will give an overview of the additional data sets that were used.

3.1 SBUV and SBUV/2

The backscattered ultraviolet technique for the measurement of stratospheric ozone was first proposed by Twomey (1961). The basic method uses measurements of Earth radiance at discrete wavelengths in the mid-ultraviolet, coupled with periodic measurements of solar irradiance at the same wavelengths. A radiative transfer model coupled with an inversion scheme is applied to retrieve ozone profiles from measurements of albedo values for each wavelength (Klenk et al., 1980). The UV experiment was first launched onboard the Nimbus-4 in April 1970 (Heath et al., 1973) orbiting at 1100 km altitude in a 10° retrograde sun-synchronous orbit.

The three-axis stabilized satellite orbits Earth every 107 min and passes through the ascending node near local noon. The longitude differences for equator-crossings in consecutive orbits is 26° . The observations cover the Earth's surface up to polar latitudes of 80° . With the SBUV experiment, the albedo is measured at 12 different discrete wavelengths from 255 to 340 nm within 32 s. The slit function which has been used has a triangular shape with a FWHM (Full Width at Half Maximum) of 1.0 nm. The swath is 200×200 km² with the subsatellite point in the center. One complete day of data consists of 14 orbit strips from south to north. Nimbus-4 data were affected by proximity to the South Atlantic Anomaly (SAA) (McPeters, 1980). Nimbus-7 (SBUV) was launched in October 1978 into a 950 km sun-synchronous orbit with a period of 104 min and an equator crossing time of 12:00 local time. In this instrument a chopper wheel has been added to eliminate SAA effects in radiance measurements. After February 1987 data quality is reduced, as the chopper wheel lost the synchronization.

The second generation SBUV experiments (SBUV/2) have been flown on Polar Orbiting Environmental System (POES) operational satellites. The NOAA POES series of satellites flies in sun-synchronous polar orbits at an altitude of approximately 850 km and a 98.9° inclination angle. With a grating as a dispersive device and a calibration system for monitoring of solar diffuser reflectivity, this instrument has a better data quality and long-term accuracy. The first SBUV/2 instrument has been flown on the NOAA-9 satel-

Instrument	Launch Date	Data Available for NLC Analysis
Nimbus-4 BUUV	4 April 1970	April 1970 to July 1972
Nimbus-7 SBUV	31 October 1978	November 1978 to June 1990
NOAA-9 SBUV/2	12 December 1984	March 1985 to February 1998
NOAA-11 SBUV/2	24 September 1988	December 1988 to April 1995, July 1997 to March 2001
NOAA-14 SBUV/2	30 December 1994	January 1996 to September 2001
NOAA-16 SBUV/2	21 September 2000	October 2000 to present
NOAA-17 SBUV/2	24 June 2002	27 September 2002 to present
NOAA-18 SBUV/2	20 May 2005	30 August 2005 to present

Table 3.1: SBUV/2 Instrument Observations based on DeLand et al. (2007).

lite, launched in December 1984 (Frederick et al., 1986). NOAA-9 has been complemented by NOAA-11, NOAA-14, NOAA-16, NOAA-17 and NOAA-18 satellites in later years. In Table 3.1 the operating times for all satellites are shown, which have been collecting ozone data for more than 20 years.

Channel	Nominal Wavelength [nm]
1	252.0
2	273.6
3	283.1
4	287.6
5	292.3
6	297.5
7	301.9
8	305.8
9	312.5
10	317.5
11	331.2
12	339.8

Table 3.2: Standard SBUV/2 Wavelengths. Taken from DeLand et al. (2003).

The overall collected data covers the years between 1978 – 2009 and new satellites are scheduled for the future. The long lifetimes of the SBUV and SBUV/2 instruments, and the overlap between multiple instruments provide the basis for a continuous multidecade NLC data set.

The SBUV/2 experiment consists of a double pointing Ebert-Fastie monochromator which is mounted perpendicular to the satellite flight direction and measures total ozone and the ozone vertical profile. All measurements are corrected for change in instrument gain, temperature dependence, and instrument response. SBUV/2 measurements are processed by NOAA/NESDIS using the NASA V6 algorithm (Bhartia et al., 1996) and are output to Product Master File (PMF) data sets. The retrieval uses the following model for calculation of the theoretical atmosphere backscattered radiance:

$$I(\lambda, \theta) = F_0(\lambda)(3\beta_\lambda/16\pi)(1 + \cos^2\theta) \int_0^1 e^{-(1+\sec\theta)(\sigma_\lambda X_p + \beta_\lambda p)} dp \quad (3.1)$$

where F_0 is the extraterrestrial solar irradiance ($\text{ergs/cm}^2/\text{sec}/\text{\AA}$), I is the atmospheric radiance ($\text{ergs/cm}^2/\text{sec}/\text{\AA}/\text{ster}$), β_λ the atmospheric scattering coefficient (atm^{-1}), σ_λ is the ozone absorption coefficient (atm cm) $^{-1}$, X_p the amount of ozone above pressure p (atm cm) and θ is the solar zenith angle. The solar irradiance is measured by using a diffuser plate on top of the satellite with nadir direction measuring the atmospheric backscatter radiance. To retrieve information on the ozone vertical profile in the atmosphere, the inversion method can be applied, since the radiance at a particular wavelength originates from a certain scattering layer. To derive the total ozone column, the attenuation of the Albedo ($\text{Albedo} = \frac{I(\lambda, \theta)}{F_0(\lambda)}$) for two given wavelength pairs with $\Delta\lambda \approx 20$ nm is measured and compared with the model calculations for different solar zenith angles (0° to 90°), two pressure boundaries (100 and 1000 mb), and a series of standard ozone profiles and Lambertian reflectance coefficients.

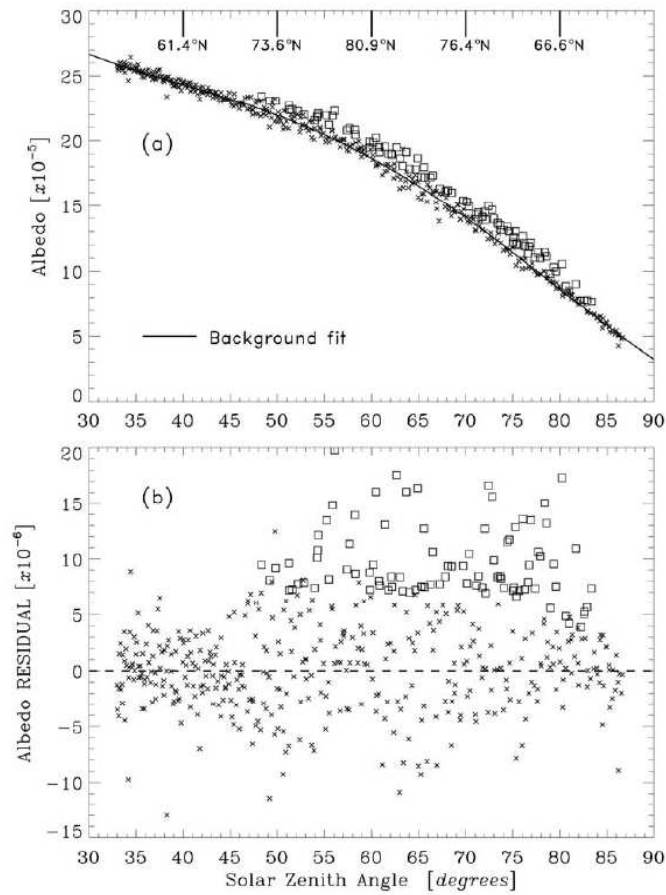


Figure 3.1: Panel a: NOAA-9 SBUV/2 252 nm albedo values for all measurements northward of 50°N on day 180 in 1985. Squares indicate measurements identified as NLCs by the detection algorithm. The solid line is a 4th order polynomial fit to all non-NLC measurements. Heavy tick marks show approximate latitudes corresponding to reference solar zenith angle values. Panel b: 252 nm albedo residuals (data-fit) for the measurements shown in panel a. NLC detections are indicated by squares. Figures taken from DeLand et al. (2003)

Since the NLC signal is on the order of the albedo variability due to ozone, the detections of NLC must be restricted by certain rules. The random instrument noise is on

the order of 0.1 % and can affect the NLC signal as well. The total albedo is enhanced if an NLC is present, but also a decrease of ozone leads to increased UV albedo signal due to Rayleigh scattering (McPeters, 1980). The NLC detection is still possible, because the enhanced albedo signal after an ozone depletion, has a different spectral signature than the NLCs. During the winter, the standard deviation of the albedo signal is on the order of NLC enhancement, and detection of NLCs during the summer season is only possible, since the summer polar region albedo is stable. The standard deviation of the albedo signal in the polar cap is on the order of 2 to 5% and is much higher compared to the variability caused by ozone variability during high latitude summer that is between 1 to 2 %.

3.1.1 Data Quality Issues

The BUUV and SBUV channel 1 with a wavelength of 255.7 nm is contaminated by NO γ -band emission (McPeters, 1989), which led to a change in wavelength of the channel 1 to approximately 252.0 nm for all SBUV/2 instruments. But the effect of the NO- γ band emission is rather small (< 2%) and no qualitative difference in the results has been found (DeLand et al., 2003). In order to characterize the diffuser degradation, some of the descending node data have been omitted during selected periods in NH spring and summer for solar zenith angle > 72°. Using the limited solar zenith angle (SZA) range data in the analysis, no difference has been found in the statistical behaviour of detected NLCs between the two data sets with full and selected SZA range. For NOAA-9, NOAA-11, and NOAA-14 the orbit drift led to later equator-crossing times of $\Delta t \approx 30$ min/year, from initial equator crossing times of 14:00 UT. The orbits crossed the terminator after approximately 6 years, and therefore the descending node data are from morning equator-crossing time. Since the NLC analysis is rather difficult for high SZA values as it is the case for near-terminator data the results for the NOAA-9 1990 NH, 1990/91 SH, and NOAA-14 2001/2002 SH NLC season must be regarded with caution. The orbit drift issues have been reduced for NOAA-16 to delay the beginning of significant orbit drift by 4-5 years (Price, 1991). Errors in the optical grating system appeared after 4-5 years of operation, that lead to wrong wavelength selection. An error of 1-2 grating positions (1 GPOS = 0.074 nm) has been observed for NOAA-9 and NOAA-11. With processor version 6 these errors have been corrected (Flynn et al., 2000). Since the terrestrial backscattered radiance increases by four orders of magnitude over the 252 – 340 nm wavelength range, measurements in Channels 1-2 are thus sensitive to out-of-band (OOB) contamination from long wavelength signals. This leads to errors of 5-6 % over bright surfaces. This error has been defined as a function of surface reflectivity and SZA. In the PMF data the OOB correction has been included.

3.1.2 Detection algorithm for NLC

The NLC detection algorithm applied to SBUV observations was first developed by Thomas et al. (1991), who used several wavelengths between 252 nm and 292 nm to determine the daily cloud-free background albedo as a function of SZA by applying a least squares fit of a fourth-degree polynomial to all data points for each day (about 14 orbits) in the polar cap region. Avoiding backscatter albedo at longer wavelengths is motivated by the fact, that the signals at these wavelengths originate in the troposphere and can be highly variable. The fit is now the definition of the background albedo. This background is then subtracted from all data to calculate a residual ϵ_λ . Since ozone depletion can mimic a high residual as

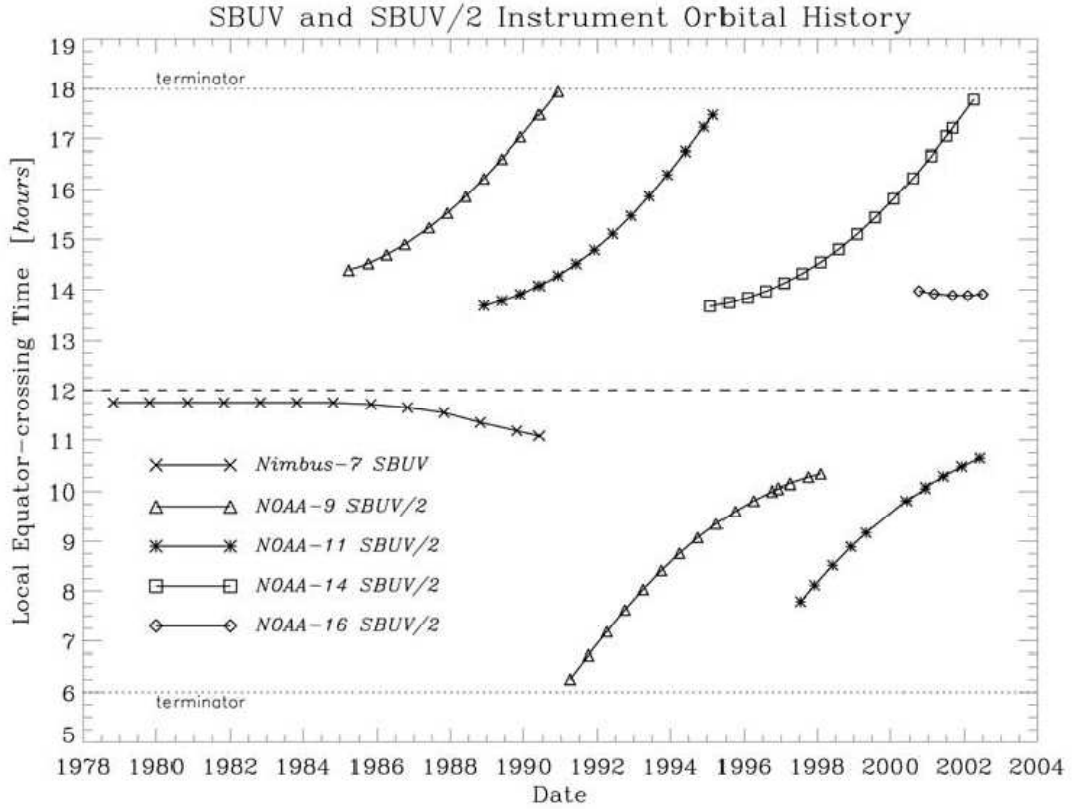


Figure 3.2: Time history of equator-crossing times for SBUV and SBUV/2 instruments. Measurements transition from ascending node to descending node when an instrument's orbit crosses the terminator. Taken from DeLand et al. (2003).

well, it is crucial to be aware of these false-positive signals. To distinguish between NLC enhancements and ozone variability, the following conditions have to be fulfilled:

- (1) Use only positive residuals $\epsilon_{252}, \epsilon_{273}, \epsilon_{283} > 0$.
- (2) The residual ϵ_{λ} should decrease monotonously with wavelength λ .
- (3) ϵ_{252} must exceed the ratio of local albedo to the albedo at 81° latitude multiplied by the standard deviation σ_{252} at the polar cap region:

$$\epsilon_{252} > \sigma_{252} \cdot \frac{\langle A \rangle}{A_{81^\circ}} \quad (3.2)$$

- (4) $\epsilon_{252} > \epsilon_{273}$

These assumptions have been chosen a posteriori after a trial and error process by comparing residuals for cloud-free latitudes before or after the NLC season. Additional tests have been made by simulating normally distributed ozone variations, and calculating the fraction of the 'false' clouds. The width of the distributed residuals has been determined by the standard deviation of the data for a given day and random residuals have been simulated. The rate of 'false positive' NLCs was of the order of 1 to 2 %, which is

close to the ozone variability of the detected clouds outside the NLC region and season (Thomas et al., 1991).

The quality of NLC detection is quantified with a NLC detection flag, $\text{FLAG} = T_0 + T_1 + T_2 + T_3 + T_4$, which consists of the following contributions:

- $T_0=16$: ϵ_{252} exceeds threshold
- $T_1=8$: $\epsilon_{252}, \epsilon_{273}, \epsilon_{283} > 0$
- $T_2=4$: $\mu_\lambda < 0$
- $T_3=2$: $\epsilon_{252} < S \times \sigma_{273}, \sigma_{252}(\phi)$
- $T_4=1$: $\epsilon_{252} > \epsilon_{273}$

where ϵ_{252} is the residual albedo at 252 nm, μ_λ is the slope of regression fit to albedo residuals, S is the scale factor and is set to $S = 1.3$ and $\sigma_{252}(\phi)$ is the standard deviation of the quadratic fit for a given latitude at 252 nm from non-NLC data. In this work we used only data with $\text{FLAG} > 29$. Using a high threshold for the NLC flag is driven by the intention to improve the data product quality.

The selection criteria fail to identify weak NLC due to temperature variability, as the chemical rates of ozone loss are temperature dependent (Brasseur and Solomon, 1984). Since the temperature changes in the upper stratosphere are mainly driven by planetary wave activity, the ozone variability increases with height, since the amplitude of the wave increases with height as well. This affects the albedo variability which maximizes at the shortest wavelengths, and leads to failure of selection criteria 2 and 4 to detect real NLCs (Thomas et al., 1991). On the other hand the ozone variation is normally distributed and can lead to both positive and negative residuals. Given this fact, the assymetry in the residual can only be explained due the presence of NLCs (see criterion 1). Figure 5 of Thomas et al. (1991) shows that for $\epsilon > 5 \cdot 10^{-6}$ the number of NLCs exceeds the number of 'non cloud' residuals. Based on this consideration the SBUV NLC data are used for further analysis with residuals of $\epsilon > 5 \cdot 10^{-6}$ only. Still there can be a very small fraction of data of 'false positive' cloud detections upon brightness, latitude and time within the season, which is due to ozone variations.

3.2 SEM on GOES

The proton flux measurements used in this study were performed by the Space Environment Monitor (SEM) instrument on the GOES (Geostationary Operational Environmental Satellite) series (GOES-5 to GOES-12). SEM is a subsystem executing in-situ measurements and monitoring the earth environment in a geostationary orbit and observing X-ray intensity, energetic particles flux and the magnetic field. The energetic particle sensor (EPS) and the high energy proton and alpha detector (HEPAD), which are mounted onboard the SEM, measure the incident flux density of protons, alpha particles and electrons over an extensive range of energy levels. The EPS makes a seven-channel differential analysis of protons from 0.8 to 500 MeV. It consists of a telescope subassembly, a dome subassembly, a signal analyzer unit and data processing unit. The telescope with a field of view (FOV) of 1.1 steradian uses signal amplifiers converting the charge pulses into voltage pulses. These detectors sense low energy protons in the range of 0.8 to 15 MeV (with detector thickness of 50 μm and area 100 mm^2) and are surrounded by tungsten

Particle Type	Channel Designation	Nominal Energy Range [MeV]	Detector Assembly
Proton	P1	0.8 to 4	Telescope
Proton	P2	4 to 9	Telescope
Proton	P3	9 to 15	Telescope
Proton	P4	15 to 40	Dome
Proton	P5	40 to 80	Dome
Proton	P6	80 to 65	Dome
Proton	P7	165 to 500	Dome

Table 3.3: Energy ranges for the Energetic Particles Sensor (EPS), adapted from Chesters (1996).

shielding. Tungsten collimators define the field of view of 70° and eliminate detector edge effects. The dome (FOV=2.0 steradian) employs three sets of two (thickness of $1500 \mu\text{m}$ and area of 25 mm^2) silicon surface barrier detectors, each with different thickness moderators covering independent fields of view, thus providing three different energy thresholds. The output provides data for four proton energy bands, ranging from 15 to 500 MeV.

3.3 MLS on Aura

In chapter 6 - dealing with a planetary wave analysis in NLC and temperature - we use the temperature data from MLS (Microwave Limb Sounder) on-board the Aura satellite. This experiment has been launched on 15th of July 2004 into a sun-synchronous orbit with a 13:45 LT ascending equator-crossing time and an inclination of 98° (a retrograde orbit) at 705 km altitude. EOS MLS is an enhanced version of the Upper Atmosphere Research Satellite (UARS) MLS experiment. It measures the thermal microwave limb emissions from atmospheric species at the frequencies 118 GHz, 190 GHz, 240 GHz, 640 GHz and 2.5 THz (Waters et al., 2006). The retrieval of the temperature profile is based on measurements of the thermal emission of O_2 near 118 and 234 GHz (Schwartz, 2008). These 'double sideband' measurements are made above and below the local oscillator frequencies and then combined to form an 'intermediate frequency' signal. The instrument performs a continuous vertical scan from the surface to about 90 km in a period of 20 s. The first published validation study by Froidevaux et al. (2006) states precisions of 0.52 K and reports a warm bias between 1 and 2 K when compared with other satellite and balloon measurements in the stratosphere. The vertical resolution of the retrieved temperature profiles decreases with height. In Table 3.4 the vertical resolution and precision of temperature profiles is shown as a function of pressure. The resolution of a single temperature profile near the mesopause is about $15 \times 220 \times 6 \text{ km}$ (vertical \times horizontal along-track \times horizontal cross-track). In this work we use the temperature profile data from the MLS Level 2.2 geophysical product, which is stored in HDF5 format and can be downloaded from: <http://disc.sci.gsfc.nasa.gov/Aura>.

\approx Altitude [km]	Pressure [hPa]	Precision [K]	Resolution Vert. \times Horiz.[km]
97	0.001	± 2.5	15×220
81	0.01	± 2.2	14×185
73	0.1	± 2.0	9.1×170
64	0.316	± 1.0	8.3×165
48	1	± 1.0	7.9×165
38	3.16	± 0.8	6.2×165
32	10	± 0.6	4.3×165
30	14.7	± 0.6	3.9×165
20	31.6	± 0.6	3.5×165
19	56.2	± 0.8	3.8×165
17	100	± 0.8	5.2×165
10	215	± 1.0	5.0×170
7	316	± 1.0	5.3×170
<7	>318	-	-

Table 3.4: Summary of MLS Temperature product, adapted from Livesey et al. (2007).

3.4 SCIAMACHY

In addition to SBUV/2 data that we use to retrieve wave characteristics in NLC signatures we include the SCIAMACHY NLC data as well. This provides a more robust comparison of the results for the wave analysis, since SCIAMACHY is independent from SBUV retrieved signals. The NLC retrieval in this work is based on limb radiance data from Scanning Imaging Absorption spectrometer for Atmospheric CHartography (SCIAMACHY). SCIAMACHY is a research instrument on-board the European satellite Envisat. It has been launched in March 2002 into a sun-synchronous orbit, with a descending equator crossing time of 10:00. SCIAMACHY observes the Earth's atmosphere in 3 different viewing geometries (limb, nadir and solar/lunar occultation) in the 212-2380 nm spectral range. In limb mode, SCIAMACHY scans the atmosphere in 3.3 km steps and measures radiation coming from a field of view of 3 km vertically, ≈ 400 km along-track and 960 km across-track.

Channel	Wavelength [nm]	Resolution [nm]
1	212-314	0.21
2	309-404	0.22
3	392-605	0.47
4	598-790	0.42
5	776-1056	0.55
6	991-1750	1.56
7	1940-2040	0.21
8	2261-2380	0.24

Table 3.5: SCIAMACHY spectral coverage and resolution for channels 1-8, adapted from Bovensmann et al. (1999).

Since the nanometer-sized NLC particles scatter efficiently the Sun's incoming UV radiation, the NLC detection algorithm looks for a peak or a strong gradient in limb radiance between 76 and 88 km at different wavelengths. More information on NLC detection and retrieval from SCIAMACHY can be found in Robert et al. (2009). The present NLC data set is based on fully calibrated SCIAMACHY level 1 data version 6.03. The SBUV/2 and SCIAMACHY data sets overlap in the years 2004-2009 with the MLS temperature profiles and should improve the intercomparison between temperature and NLC data.

Chapter 4

The nature and characteristics of NLC

In this chapter we want to introduce the properties of NLCs and the physical processes behind their formation and evolution. For the analysis of the NLC occurrence rate we used the SBUV/2 data, which we described in chapter 3.

NLCs or noctilucent clouds which have been observed for the first time in the year 1885 by several observers (Backhouse, 1885; Jesse, 1885; Leslie, 1885) are very thin ice clouds that occur during the summer season in the high latitudes near the mesopause. The backscatter albedo of these clouds is on the order of $10^{-6} Sr/cm^2$. Since these clouds are very thin and exhibit very low luminosity due to backscattering of the incident solar light, the observation from the ground is only possible after sunset, where the lower part of the atmosphere is in darkness. This is the main reason for their historical name of 'noctilucent' (visible during the night) clouds. These clouds are visible after the sunset because they can be found only at an altitude of ≈ 83 km. These ice clouds are formed by nucleation of water vapor into ice particles. Detailed descriptions of the NLC season, NLC altitude and nucleation mechanism as well as the particle size of these ice clouds can be found in sections 4.2, 4.3 and 4.4 respectively. The NLCs are also referred to PMCs (Polar Mesospheric Clouds) in some studies. In order to avoid any misunderstanding we will use only the term NLC.

4.1 Occurrence rate of NLC

The SBUV/2 instruments, that have been used to quantify the NLC characteristics, were meant to measure the ozone layer and changes in ozone signal, rather than the observation of NLCs. The idea was to use the backscatter signals of ozone measurements to extract the NLC signal. For ground-based and visual observations of NLCs the number of nights with NLC displays is often used for quantitative analysis. This is rather a subjective quantification of NLC observations compared to a more sophisticated mathematical definition. Moreover the ground based observation is limited due to weather conditions, observation geometry, subjective impression and experience of the observer regarding the classification of NLC features. Last but not least it is restricted to a given location. Some of these handicaps are eliminated by using the LIDARs. Still it is a local observation of the NLC property. The use of satellites for NLC observation makes longterm and global observations of this phenomenon possible. Calibration and comparison with different satellites is still necessary. Since satellite measurements are available for most of the locations, it is

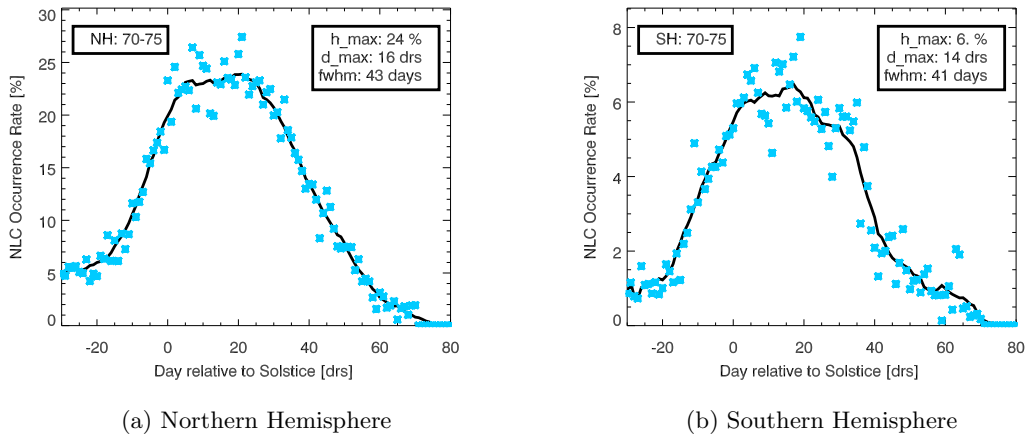


Figure 4.1: Averaged occurrence rate of all NLC seasons (blue cross) from SBUV/2 data for the satellites NIMBUS 07 – NOAA 18 for the years 1978 – 2008 and latitude band $70^\circ \text{ N} - 75^\circ \text{ N}$ (panel a) and $70^\circ \text{ S} - 75^\circ \text{ S}$ (panel b), and smoothed with a 10-day box car function. The Gaussian fit parameters shown in the right box, corresponds to height of the curve, position of the maximum and the full width at half maximum.

even possible to compare and validate with ground based measurements.

The question arises, how to quantify the occurrence rate of NLCs using satellites data. The intuitive step toward the quantification of NLCs is to define the occurrence rate of NLCs for a given latitude and longitude bands for a given day as follows:

$$\text{Occurrence Rate}(\Delta\phi, \Delta\theta) = \frac{\sum NLC_{\Delta\phi, \Delta\theta}}{\sum Data_{\Delta\phi, \Delta\theta}} \quad (4.1)$$

where $\Delta\phi$ and $\Delta\theta$ are the latitudinal and longitudinal bands. The ratio corresponds to number of NLCs detected to the total number of observations for the given bin. By applying this method we get a distribution of NLCs for each day, each longitude and latitude bin over the entire season.

4.2 NLC season

Comparing different years, the overall structure of the seasonal evolution of the NLC occurrence rate is similar. Figure 4.1 (panel a) shows the average occurrence rate of all seasons from the SBUV data of the satellites data NIMBUS 07 – NOAA 18 and the years 1978 – 2008 and for the northern hemisphere. Figure 4.1 (panel b) shows the same average but for southern hemisphere. The blue symbols correspond to the average of all data, and the black curve is generated by convolution with a 10-day box car function. A Gaussian fit to this curves gives the occurrence rate maximum, its position in the season and the width of the NLC season, as noted in the legend in the top right box.

The NLCs cover most of the summer polar cap region of the Earth on a single day, especially in the middle of the NLC season. A contour plot of the NLC occurrence rate as a function of longitude and time, also known as Hovmöller-plot is shown in Figure 4.2 for the year 2000 in the northern hemisphere. The presence of waves in the NLC occurrence rate field is found as well. The maximum of the occurrence rate during the summer polar

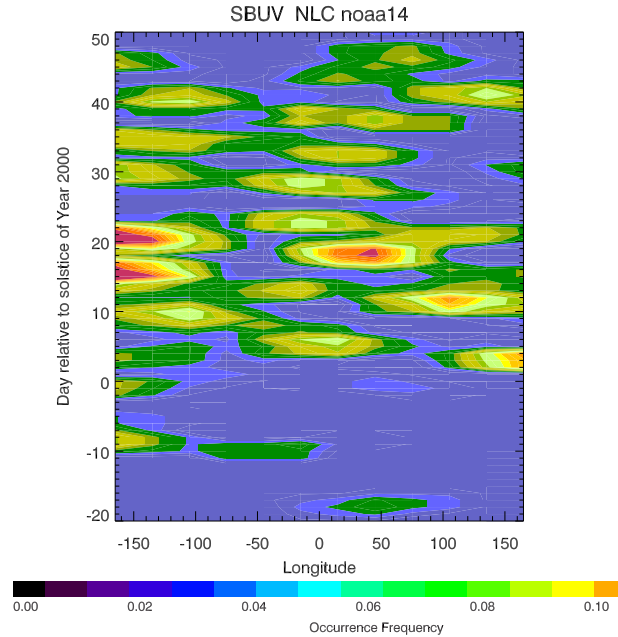


Figure 4.2: Contour plot of NLC occurrence rate as a function of longitude and time for the season 2000 in the northern hemisphere and for the latitude band $60^\circ - 70^\circ$.

season is observed between solstice and day 20 after solstice. In Fig. 4.3 the zonal mean of the occurrence rate is plotted for three different latitude bands for the season 2004/05. The data is smoothed with a box-car function with a width of 5 days. Here we can see that the higher latitudes correspond to higher NLC occurrence rate.

The beginning of the NLC season is 30 days before solstice and the end of the NLC season is around 60 days after solstice corresponding to end of May and mid August in the northern hemisphere, end of November and mid of February in the southern hemisphere. For a given season the fluctuation is quite large. Planetary waves in the mesospheric temperature and H_2O fields with short time periods as well as ≈ 13 -day and 27-day wave patterns as a result of Sun rotation can affect the signal significantly (Robert et al., 2010).

The temporal evolution of the NLCs shows huge differences between the $60^\circ - 70^\circ$ and $70^\circ - 80^\circ$ latitudinal bands as shown in Figure 4.3. The position of the maximum as well as the FWHM of the curve, which corresponds to the beginning and the end of a NLC season, depends on the latitude band. Furthermore, the occurrence rate in the lower latitude band is less perturbed and more stable compared to the higher latitudes. Despite this, the occurrence rate is higher for the higher polar latitudes. Similar differences between different latitudes are observed for the southern hemisphere. Examples of the latitudinal and temporal variation of NLC radiance and NLC residual albedos derived from SCIAMACHY and SBUV observations of the year 2008 in the northern hemisphere are shown in Fig 4.4 panel a and panel b, respectively. Both instruments show good qualitative agreement in terms of the seasonal variation of NLC albedo, even though they measure with different techniques. The double peak around day 195 is visible in both

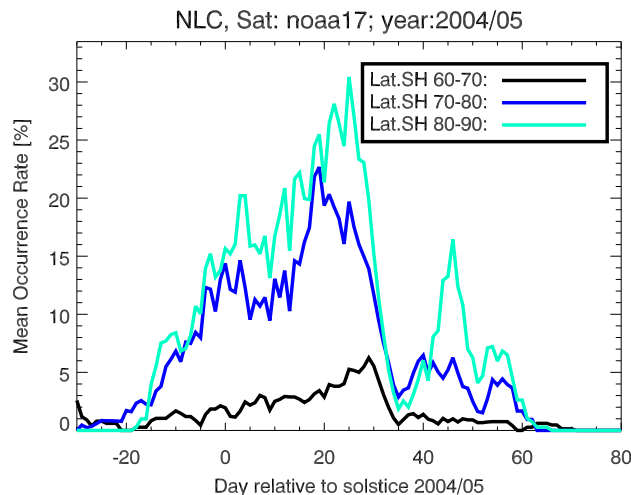


Figure 4.3: An example of zonal mean NLC occurrence rate for the season 2004/05 in the southern hemisphere and three different latitude bands.

contour plots. It is obvious from these plots, that the NLC albedo is highest for the latitude band $70^{\circ} - 80^{\circ}$, and decreases with decreasing latitudes. The NLC core season, where larger NLC albedos occur seems to begin at solstice and lasts until 40 days after solstice (days 175 – 215 of the year).

4.3 Altitude of NLCs

The altitude of NLCs varies during the summer season and with latitude, which has already been observed and modeled by different groups. In the southern hemisphere the altitude of the NLC is higher than in the northern hemisphere, since the SH is warmer compared to NH and the height of the temperature minimum is higher (Fig. 4.5). The seasonal distribution of NLC altitude for a given latitude band that has been retrieved by Rusch et al. (2008) using the Student Nitric Oxide Experiment (SNOE) NLC data is shown in the right panel of Figure 4.6 (Rusch et al., 2008).

The explanation for this variability is the thermodynamical process of super saturation which is very sensitive with respect to temperature changes. At the beginning of the season when the mesopause region is not cold enough to form ice particles and the super saturation state is not reached, no NLCs can be observed. As the mesopause region gets colder and NLC particles start to grow, sedimentation of the grown particles takes place. If the water vapor partial pressure exceeds the saturation pressure, then growing can also take place for constant H_2O vmr (volume mixing ratio). Since growth of the NLC particles is limited to a certain altitude range because the temperature increases with decreasing altitude, further sedimentation is not possible and leads to sublimation of NLCs at lower heights as they fall down (Witt, 1969; Chu and Gardner, 2003).

Reversal of the large scale meridional circulation leads to warming of the lower mesopause and more sublimation of the lower part of the NLC layer due to weakening of the meridional circulation and decreased upwelling in the summer mesopause region takes place (Rusch et al., 2008). In addition, the lower part of the NLC sublime and only NLCs at higher altitudes can be observed. Thus the NLC particles 'gain' height and can be observed at the nearly same position as at the beginning of the NLC season. This symmetrical behaviour of the NLC altitude through the summer season is driven by four factors: temperature

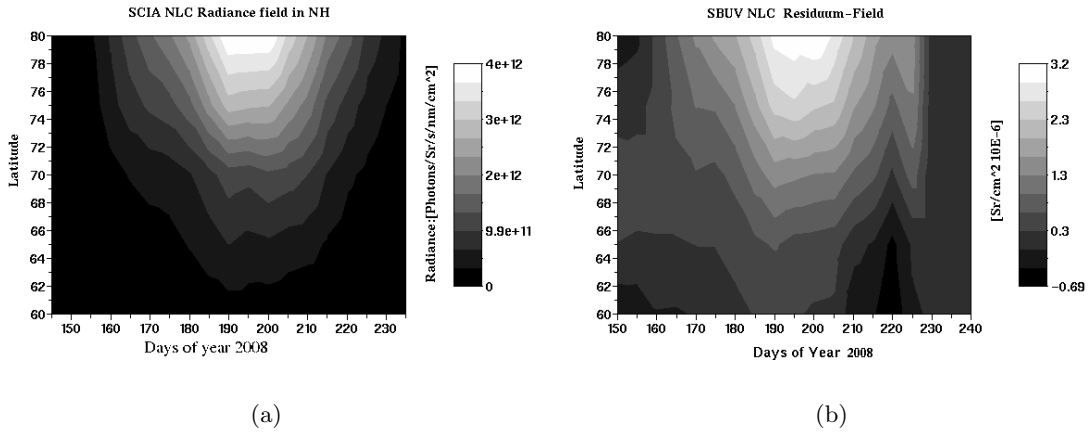


Figure 4.4: A contour plot of the SCIAMACHY NLC radiance field during the NLC season 2008 in the range of 83 – 86 km in the northern hemisphere (panel a) and the SBUV NOAA – 17 satellite data of the NLC residual albedo for the same year and hemisphere.

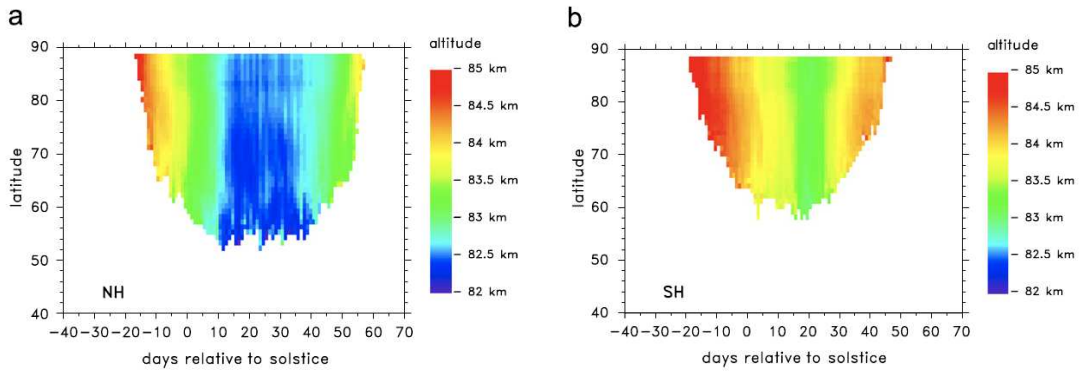


Figure 4.5: Mean altitude (daily zonal mean) of NLC with backscatter coefficients $4 \times 10^{-10} / (srm)$ as a function of latitude and season in the NH summer of 2001 (panel a) and in the SH summer of 2004/2005 (panel b). Taken from Lübken and Berger (2007).

evolution, sedimentation of NLC particles, the rate of sublimating particles at the lower end of the NLC layer and last but not least the water vapor transport. The altitude of the NLC layer can not be retrieved with SBUV data, since the nadir viewing geometry does not provide altitude information. The diagrams on altitude variations of the NLC layer that we present here are based on SNOE (Rusch et al., 2008), HALOE (Wrotny and Russel III, 2006) and GOMOS (Global Ozone Monitoring by Occultation of Stars) (Perot et al., 2010).

The seasonal variation of NLC altitude in Figure 4.5 was modeled with LIMA (Lübken and Berger, 2007). The decrease of the altitude and increase after day 40 relative to solstice is reproduced well. The southern hemisphere shows higher altitudes and shorter duration of the stable state at lower altitudes. The interhemispherical difference in NLC property is due to stability of winter polar vortex in the southern hemisphere that leads to stable temperatures in the northern hemisphere in the mesopause region (interhemispheric coupling). The short period of NLC enhancement in the southern hemisphere is due to complicated behaviour of the northern polar vortex in the northern hemisphere during the

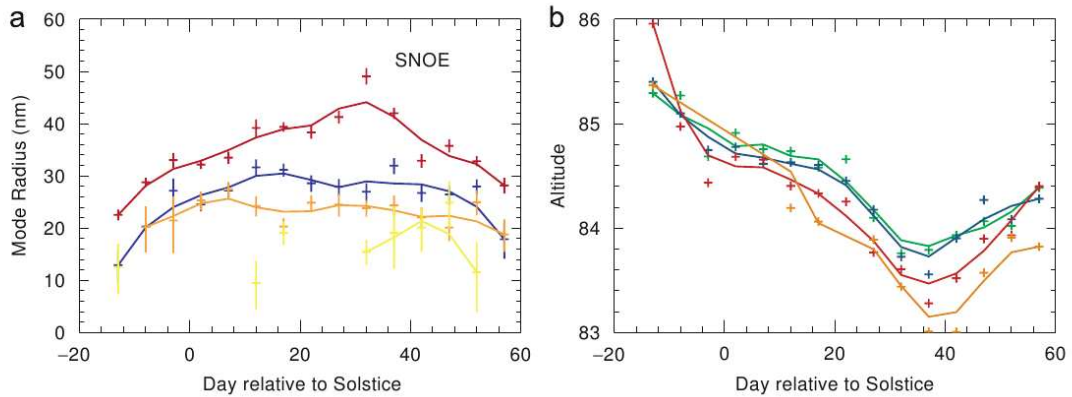


Figure 4.6: Panel a): Particle radius vs. day from solstice for the northern hemisphere of the year 2000; 77.5 – 82.5°N (green); 72.5 – 77.5°N (blue); 67.5 – 72.5°N (red) and 62.5 – 67.5°N (yellow). Panel b): Cloud altitudes for the four latitude bands shown in (a) (Taken from Rusch et al. (2008)).

same season (Becker and Fritts, 2006). For the northern hemisphere the minimum altitude is around 82 km. This is in good agreement with altitude results derived from SNOE data (Fig. 4.6). The optically visible NLC layer is around 82 km during the core season, but may be as large as 86 km. As pointed out earlier the altitude of the NLC layer decreases until day 20 after solstice and increases again afterwards. This observational finding is in agreement with the theoretical explanation.

The GOMOS, SNOE and LIMA results agree well regarding the symmetry of the seasonal evolution of the NLC altitude. All of them show the symmetrical behaviour in the northern hemisphere. The asymmetrical behaviour of the NLC altitude in the southern hemisphere is observed in SNOE and reproduced in LIMA model simulations. The height of the NLC layer is larger in the southern hemisphere than in the northern hemisphere. This interhemispheric difference of the NLC layer altitude has been reported in GOMOS (Fig. 4.7) and HALOE (Fig. 4.8).

If the height of the NLC altitude is determined in part by sedimentation, sublimation and temperature fluctuations, one can expect a diurnal variation in height, since there are diurnal tides occurring at the mesopause region. Jensen et al. (1989), using model simulations was not able to find diurnal variations of NLC heights using a one dimensional NLC model. However, LIDAR observations made by von Zahn et al. (1998) clearly show a semi-diurnal variation of the NLC altitude for the season 1997 in the NH at the Alomar observatory. The result of their work is that the variation in backscatter ratio R_{max} and NLC layer altitude z_c depends on the local time (LT). R_{max} and z_c are strongly dominated by a semidiurnal tide. The altitude of the NLC layer maximizes near 1300 LT and 0100 LT and has minima near 0700 LT and 1900 LT. The backscatter ratio R_{max} is in antiphase with z_c as shown in Figure 4.9.

4.4 Particle Size

From the first sighting of NLCs 125 years ago the question has arisen among scientists, what the nature of NLC particles is. The main properties of NLC particles are now established, but some details still remain unknown. An important step for explaining the nature of NLCs was to establish a nucleation site, on which the water vapor at pressures

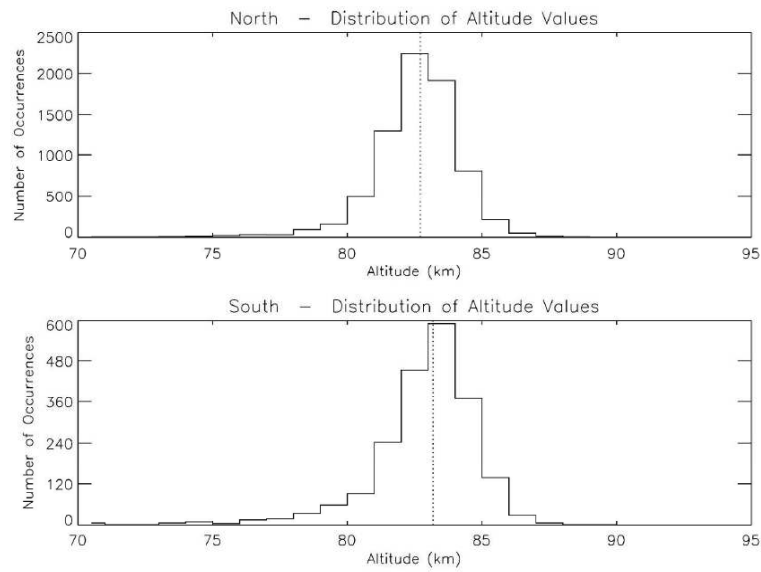


Figure 4.7: Distribution of NLC altitudes for each hemisphere derived from NLC observations with GOMOS on Envisat. The obtained median value is 82.7 km for the Northern Hemisphere and 83.2 km for the Southern Hemisphere. Adapted from Perot et al. (2010).

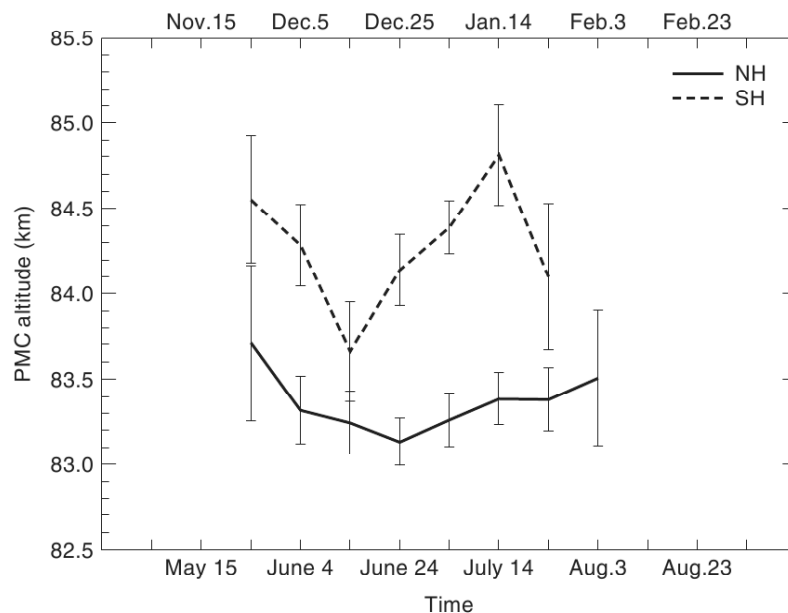


Figure 4.8: The seasonal distribution of NLC altitude for all NLCs observed by HALOE from 1991 to 2005 and latitudes between 55° and 70° . The timeline for the southern hemisphere summer is at the top of the plot. The uncertainty for each point in the distribution is defined as the standard error of the mean (standard deviation of the sample divided by the square root of the number of samples). Taken from Wrotny and Russel III (2006).

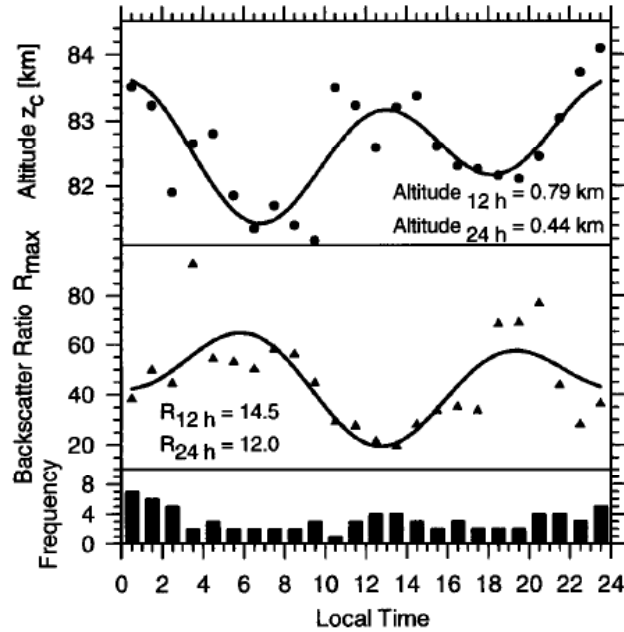


Figure 4.9: Hourly centroid altitudes z_c (upper panel, circles) and hourly maximum backscatter ratios R_{max} (middle panel, triangles) of NLCs observed during June/July 1997. Harmonic fits (solid lines) to the data show marked semi-diurnal variations of both parameters. The bars in the lower panel show the number of observed NLC events per hour of day. Taken from von Zahn et al. (1998).

of 0.004 mb and temperatures below 150 K is able to form ice crystals. The nucleation sites were assumed to originate from meteoric ablation in the upper atmosphere (Witt, 1969). However, since meteoric dust may be transported due to the large-scale meridional circulation away from the summer polar cap, there may not be enough dust particles in order to initiate the deposition of water vapor onto ice crystals (Megner et al., 2008). Several other nucleation nuclei have been proposed such as: ionic water clusters (Witt, 1969), sodium bicarbonate (Plane, 2000) and sulfuric acid aerosol particles (Mills et al., 2005). Recently charged meteoric smoke particles have been introduced as possible nucleation nuclei by Megner and Gumbel (2009). One has to be aware of the fact that the NLC layer is the visible part of a layer that contains particles and produces strong radar echo signals called Polar Mesospheric Summer Echoes (PMSE) (Rapp et al., 2003).

In order to define an ensemble of particles, the particle size distribution (PSD) of the NLCs and the physical shape of a single ice particle have to be specified. Assumptions on the shape of the NLC particle can be made due to its axis ratio. Following geometrical shapes like prolate spheroids, spheres, oblate spheroids and cylinders with axis ratios of 0.2, 1.0, 5.0 and 1.0 are proposed for the NLC particles. Making different assumptions on the particle shape may lead to significant differences in the particle size. Robert et al. (2010) obtained values of 60 nm, 45 and 55 nm for prolate, spheroid and oblate respectively for the NLC particle radius. They showed that there is no difference in the relative temporal variation in retrieved sizes for the different shapes of the NLC particles. Different studies of the NLC particle size show the growth of the particles from 15 nm at the beginning of the season to up to 75 nm in the core season (von Cossart et al., 1999; Alpers et al., 2000;

Carbary et al., 2002; Karlsson and Rapp, 2006; von Savigny and Burrows, 2007; Rusch et al., 2008; Lumpe et al., 2008; Robert et al., 2010). The reason for the seasonal variation of NLC particle size is the higher saturation ratios in the middle of the season. The particle size decreases at the end of the season again, as the saturation drops down with increasing temperatures. Similar particle size range has been observed due to latitudinal variation with smaller particles at lower polar latitudes and larger particles at higher polar latitudes.

The most frequently used particle size distribution (PSD) has been the log-normal distribution, which was generally used until a few years ago. Now a normal distribution (Gaussian) is used, because model simulations and observations are more consistent with a Gaussian PSD:

$$f(r) = \frac{1}{\sqrt{2\pi}\sigma} e^{-\frac{(r-r_0)^2}{2\sigma^2}} \quad (4.2)$$

with σ being the width of the PSD, r the particle radius, and r_0 the mean radius of the NLC particles. The retrieved particle radii for a lognormal PSD are smaller compared to a Gaussian PSD. Carbary et al. (2002) used UVISI (Ultraviolet Imaging and Spectrographic Imaging) on MSX-6 (Midcourse Space Experiment) measurements in the southern hemisphere assuming a log-normal PSD and $\sigma=1.43$ and found radii of 20-70 nm. A 6th moment function has been used by Rusch et al. (1991):

$$r_6 = r_0 [e^{18\ln^2\sigma}]^{1/6} \quad (4.3)$$

with a σ of 1.4 and an average value of $r_6 = 42.6 \pm 16.4$ nm has been found. von Cossart et al. (1999) used the LIDAR technique from the ground with a log-normal PSD and retrieved radii of $r_0=51 \pm 21$ nm with a $\sigma = 1.42 \pm 0.22$. The SCIAMACHY data that have been used by von Savigny and Burrows (2007) with normal distribution and $\sigma = 12$ nm. They found radii of $r_0 = 66 \pm 13.9$ nm for the latitude band of $65^\circ - 75^\circ$ N. The radii modelled by Rapp and Thomas (2007) are smaller by a factor of 0.4 compared to the SCIAMACHY radii. von Zahn et al. (1998) found a semidiurnal variation of the NLC backscatter signal, and since the backscatter radiance is highly dependent on the NLC particle radii, it is thought to be originating in part from a variation in NLC particle size. Gumbel and Witt (1998) used rocket sonde photometry, assumed a mono-disperse PSD and found radii between 60 – 70 nm. Microphysical modelling with the COMMA/IAP model yielded a normal PSD with mean radii of 10 – 25 nm and σ of 8 – 15 nm (Berger and von Zahn, 2002). CARMA simulations deliver NLC particle sizes of $r \approx 41$ nm and $\sigma = 11$ nm at $\phi = 69^\circ$ (Rapp and Thomas, 2006).

A latitudinal difference in NLC particle size is observed as well. As von Savigny and Burrows (2007) already showed for the NH 2005 season using SCIAMACHY data, the particle radii increase with latitude. Karlsson and Rapp (2006), using OSIRIS in the SH found the same relationship between particle size and latitude. A bimodal feature appeared in their data with $r = 85$ nm for $\phi > 85^\circ$. They concluded that the second radius mode comes from second-life cycle of NLC particles. The interpretation of the latitudinal dependence is based mainly on the polar summer temperature field. Mesopause temperatures generally decrease with increasing latitude, leading to the observed particle size gradient. Extensive use of SCIAMACHY data by Robert (2009) showed a particle size increase from $55^\circ - 83^\circ$ latitude where the exact values strongly depend on the assumed PSD and shape, for normal and lognormal PSDs and different particle shapes. No bimodal feature has been found using the NH data. The latitude dependence of radius is

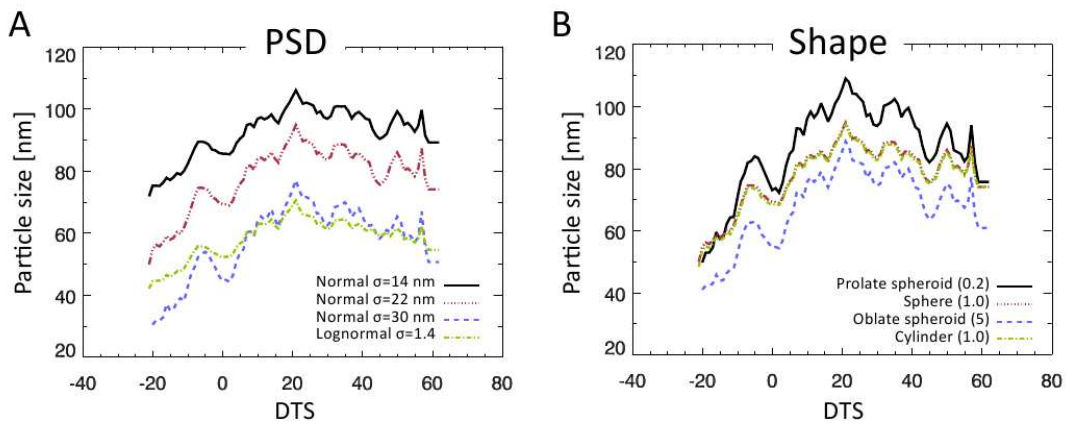


Figure 4.10: Panel A: mean seasonal variation of the NLC particle size retrieved using different PSD assumptions: Normal PSD with $\sigma = 14$ nm (solid), 22 nm (dotted), 30 nm (dashed) and lognormal PSD with $\sigma = 1.4$ nm (dashed-dotted). The particle sizes presented were between 75 – 83 nm and the shapes were assumed spherical. Panel B: Mean seasonal variation of the NLC particle size retrieved for different assumptions on the particle shape: spheroids with axis ratio 0.2 (solid), 1.0 (dotted), 5.0 (dashed) and cylinders with axial ratio 1.0 (dashed-dotted) (Adapted from Robert (2009)).

thought to be approximately on the order of $+1.4 \pm 0.1$ nm/deg for a normal PSD and $\sigma = 22$ nm.

As pointed out earlier the sedimentation of NLC particles takes place as the NLC particles start to grow in size. Due to gravity force they fall down to lower heights. Thus there is a high likelihood of finding a relationship between NLC particle size and altitude. Rocket sonde measurements by Gumbel and Witt (1998) showed the vertical dependence of the particle size of 15 nm/km. von Savigny et al. (2005) found for both hemispheres an increase of NLC radii with decreased altitude using OSIRIS (Optical Spectrograph and Infra Red Imager System) NLC data. Baumgarten et al. (2008) showed a similar anti-correlation of NLC particle radii and altitude (20 nm/km) using the LIDAR technique at Alomar.

The NLC PSD and shape are still under investigation and a workgroup has been established working on the optimal estimation of the size and shape of NLC particles using satellite data, ground based LIDAR and in-situ measurements of rocket-sonde experiments.

This includes the satellite missions like SCIAMACHY, OSIRIS, SOFIE, CIPS (Cloud Imaging and Particle Size Instrument) and SNOE as well as the LIDAR group at Alomar. Recent results and comparison of different parameters used lead to the conclusion that spheroid shaped ice particles with axis ratio of $AR = 0.5$ and PSD with a width which is dependent on the radius with $\sigma = r/2$ provides the best model for all data sets. This leads to radii up to 60 nm for the highest latitude. This consensus is a step in the right direction, but there is still room and a lot of work to do to improve the understanding of the PSD and particle shape of the NLCs in the future.

4.5 Influence of the 11-year Solar Cycle on NLC

The investigation of a possible connection between the 11-year solar cycle and NLC displays goes back to the 1930s, mainly based on the ground based observations. The insufficiency of the historical data base of cloud detection makes it difficult to establish a long-term validation of the relationship. Gadsden (1982) deduced an anti-correlation with a time lag of 2-3 years between solar activity and the number of NLC displays. A connection between the number of nights with NLC displays N and averaged sunspots number have been found (See Fig. 4.11) (Thomas et al., 1991). The number of sunspots is also regarded to be not a good proxy for solar Lyman- α flux during the solar maximum condition (Lean, 1983). They found, that the Lyman- α flux does not change smoothly over the solar cycle, but increases abruptly just before the solar maximum and decreases in the same manner afterwards. However, since it is the only available link for the historical data of NLC observations, this had to be used in this case. Figure 4.12 shows a plot of the number of NLC displays during a given season and number of sunspots from 1967 to 1987. An inverse relationship between two time series can be observed.

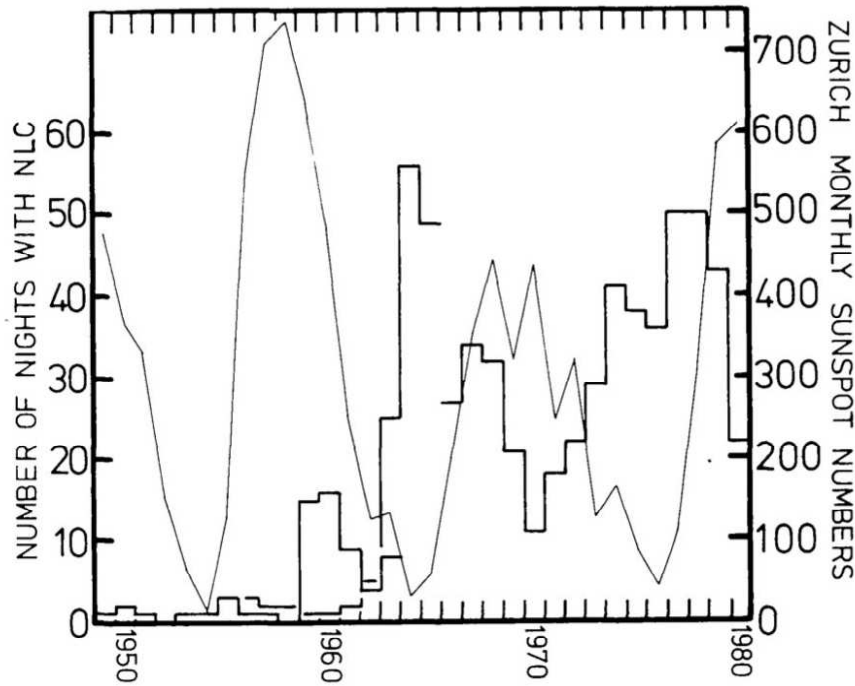


Figure 4.11: The variation in number of nights with noctilucent clouds from the year 1949 to year 1980. The 1949 – 1963 data are from Paton (1964), the 1956 – 1965 data from Fogle and Haurwitz (1966), and 1966 – 1980 (North European) data have been summed by Simmons and McIntosh (1983). The thin line shows the summer sums (May + June + July + August) of the Zürich monthly mean sunspot numbers. Taken from Gadsden (1982).

However, both Gadsden (1982) and Fogle and Haurwitz (1966) assumed that the connection of NLC reduction and solar activity is not particularly strong. According to Lean (1983) the Lyman- α radiation varied during cycle 21 by a factor of 1.8 in opposite to rocket and SME observations which recorded a factor of 2.5 for Lyman- α . The abrupt change in Lyman- α flux before solar maximum followed by a decrease does not correlate well with the number of sunspots or 10.7-cm radio flux. Thus it could be hard to find a

connection between NLC variation and number of sunspots or 10.7-cm radiation as has been pointed out by Garcia (1989).

Sonnemann and Grygalashvily (2005) showed a perturbation of water vapor content of up to 20% at 67° in 83 km altitude associated with the 11-year solar cycle. NLCs can be affected by a change in water vapor and thus show the solar cycle indirectly. However, only +4% change of water vapor at 80 km altitude has been observed from the ground between the years 1996 and 1999 at Alomar 69°N (Seele and Hartogh, 1999). They assumed a freeze-out drying effect of ice particles to reduce the water vapor Lyman- α response. Lübken (2000) found no significant solar cycle variation with temperature using rocket-sonde measurements in the latitude range of 66 – 71°N. But most of these data in the polar mesopause were made during the solar minimum period.

Results from the HALOE instrument aboard the UARS show significant solar cycle variation of the temperature at 80 km altitude around the latitudes of 40°N with an amplitude of 1.0-1.7 K which is in phase in the upper stratosphere but shows a time lag of 1-2 year in the upper mesosphere at NH midlatitudes with temperature lagging behind the solar UV flux forcing (Remsberg et al., 2002). The idea was, that the solar cycle signature in temperature originates from planetary wave activity coming from the solar cycle effects on stratospheric ozone. The V_{pmc} data (V_{pmc} HALOE data refers to the retrieval products of aerosol extinction profiles at four different wavelengths, where temperature, O_3 and water vapor retrievals are corrected for the presence of PMCs (NLCs)) have been used by Hervig and Siskind (2005) for the latitude range of 65° – 70° who found a temperature variation with solar cycle of the order of 5 K at 85 km. A significant phase lag between Lyman- α flux and NLC occurrence rate has been found of up to 1.2 years for the southern hemisphere and between 0 and 2 years for the northern hemisphere with NLC signal lagging the Lyman- α forcing. The reason for this time lag originates from observed anti-correlation between Lyman- α flux and water vapor. Here the water vapor lags the solar forcing of up to 1.8 years and 1.6 years for the northern and southern hemisphere respectively.

The first evidence with SBUV data of a possible relationship between solar influence and NLC response was provided by Thomas et al. (1991). They used the entire NLC season and the Mg-II index data from the solar ultraviolet instrument on SME. They found for the period 1981 – 1989 that the MgII index, which is the core-to-wing ratio in the MgII Fraunhofer lines (280 nm) and a proxy for Lyman- α flux, is highly correlated with NLC variation with a correlation coefficient of -0.973 for 1500 data points. They also found hemispherical discrepancies between the southern and northern hemisphere for the solar response of the NLC variation. They concluded that the northern hemisphere is less sensitive to the solar activity compared to southern hemisphere. DeLand et al. (2003) used the SBUV/2 data in order to find a relationship between NLC residual albedo and solar Lyman- α flux. They found for the years 1978 – 2002 an anti-correlation of -0.87 for the northern hemisphere with a lag of 0.5 year and the NLCs lagging behind the Lyman- α flux. For the southern hemisphere, a weaker relationship is found with anti-correlation of $R=-0.65$ and no time lag.

If the 11-year solar cycle influence is responsible for the depletion of NLC and the time constant for water vapor dissociation in the upper mesosphere is thought to be of the order of 10 days (Thomas et al., 1991), then they assumed to expect an observation of a 27-day response of NLC to the solar flux variation. The 27-day signal in NLC activity have been detected in the SME data for the years 1981 – 1989 (solar minimum activity period) (Simon (1990), unpublished research).

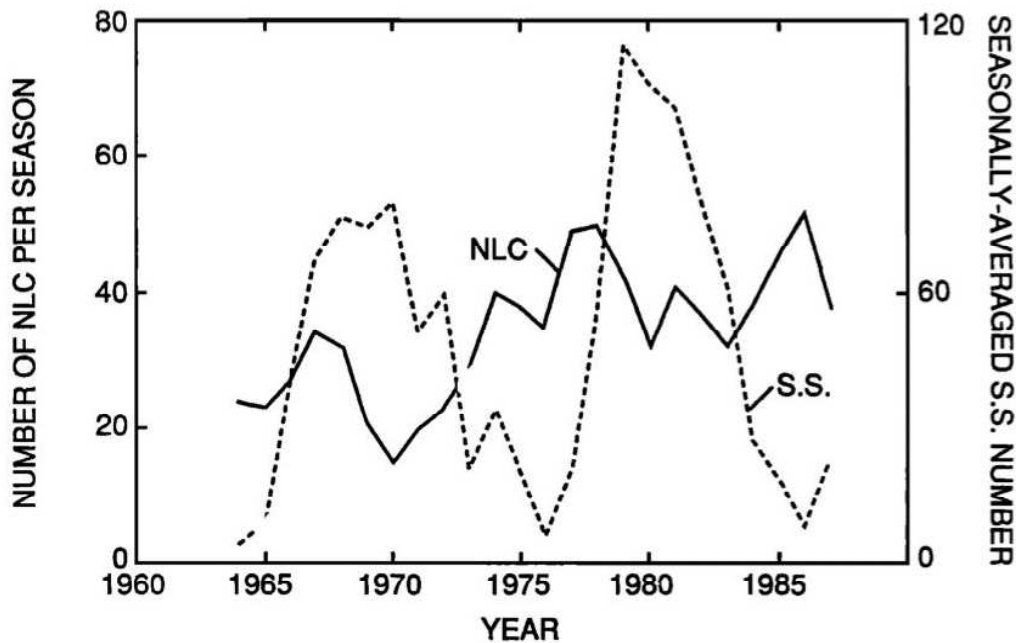


Figure 4.12: The solid curve shows the number of nights during which noctilucent clouds were sighted versus year. The dashed curve shows seasonally averaged sunspot number versus year. Taken from Thomas et al. (1991).

Garcia (1989) showed in a model calculation a decrease of water vapor of 35% – 40% at 80 km during the solar maximum period compared to solar minimum. They concluded, that two processes could be the driver for NLC reduction. Besides the reduction of water vapor, the increase of temperature due to high solar fluxes, which raises the saturation vapor pressure and decreases the partial pressure of water is significant. Thus this leads to NLC reduction during the phases of increased solar activity.

Gadsden (1998) showed from available mesopause temperature data of the years 1964 – 1994 a clear anti-correlation of the annual NLC occurrence number, but only for the secular component, not the solar component. This result means that the mesopause temperature has no important solar-cycle dependence, which is a surprising outcome, since NLC is strongly controlled by solar cycle (DeLand et al., 2003).

DeLand et al. (2007) used the SBUV/2 data to derive a correlation between solar cycle and NLC occurrence rate using 23 years of NLC data. They found that the highest correlation between solar Lyman- α flux and NLC albedo residuals had a time lag of 0.5-1.0 years with uncertainty of ± 1 year and the NLC albedo residuals lagging behind. Sensitivity studies showed rather marginal change in correlation values for change in time lag. The result agrees well with the ground based observations of the two processes. Stratospheric temperature might be an explanation, however Gadsden (1998) showed that stratospheric temperature is in phase with solar cycle. Another explanation comes from the fact that the mesospheric upward winds are lagging behind as well, and since these winds control significantly the adiabatic cooling, NLC growth and water vapor content (Rapp et al., 2002), it could contribute to the time lag observed.

Robert et al. (2010) investigated the relationship of Lyman- α flux and NLCs using the SCIAMACHY and SBUV/2 data. A significant anti-correlation between the Lyman- α anomaly and NLC occurrence rate anomalies has been found providing evidence for a

27-day solar cycle signatures in NLCs. This signature is more pronounced in the northern hemisphere than in the southern hemisphere. Comparison of MLS observations of mesospheric water vapor and Lyman- α flux, indicated that the water vapor does not explain the variation of NLC due to solar activity. On the other hand the temperature variation, which was found to be modulated by the solar activity is the main driver for the 27-day signal in the NLC time series.

Chapter 5

Solar Proton Precipitation and its impact on NLCs

The Sun plays a major role in the dynamics and variability of the Earth's atmosphere. The question addressed in this chapter is, whether the effects of the short period outbursts in the Sun followed by precipitation of highly energetic particles in the Earth's polar cap regions, show significant impact on the evolution and variation of NLCs or not. The effect of the 11-year solar cycle on NLCs has been discussed in Chapter 4.5. Here we want to investigate in detail the effect of every single solar proton event on NLCs during the NLC season, which is one of the main aspects of this thesis.

5.1 Solar Proton Events

The overall properties of a coronal mass ejection followed by the precipitation of highly energetic particles, that is called Solar Proton Events, were described in Chapter 1. Since these events are rare phenomena, the investigation of the effects of solar particle precipitation is accompanied with few datasets to study. On the other hand, the effects during and after such events on the chemical and dynamical balance in the Earth's atmosphere are remarkably significant. In this part we would not like to go into more detail about the variety of effects that an SPE may ignite, but concentrate more on the work that we have done so far. For a more general discussion of the influence of SPEs on the atmosphere, we refer to Chapter 1.

5.1.1 SPE and NLC reduction

The main parts of the work presented in this section have been already published (Rahpoe et al., 2010). As von Savigny et al. (2007a) (See Chapter 1) pointed out a possible connection between a strong SPE starting on 18 January 2005 that lasted for several days and the depletion of NLCs in the southern hemisphere in the following days after the proton precipitation, this is the major direction of our work. Therefore we want to investigate in more detail if the depletion observed after the SPE in January 2005 was rather an exception. We searched for possible SPEs which occurred during the NLC season in the northern and southern hemispheres. For this purpose, using long-term data of solar proton precipitation and NLC occurrence rate is appropriate.

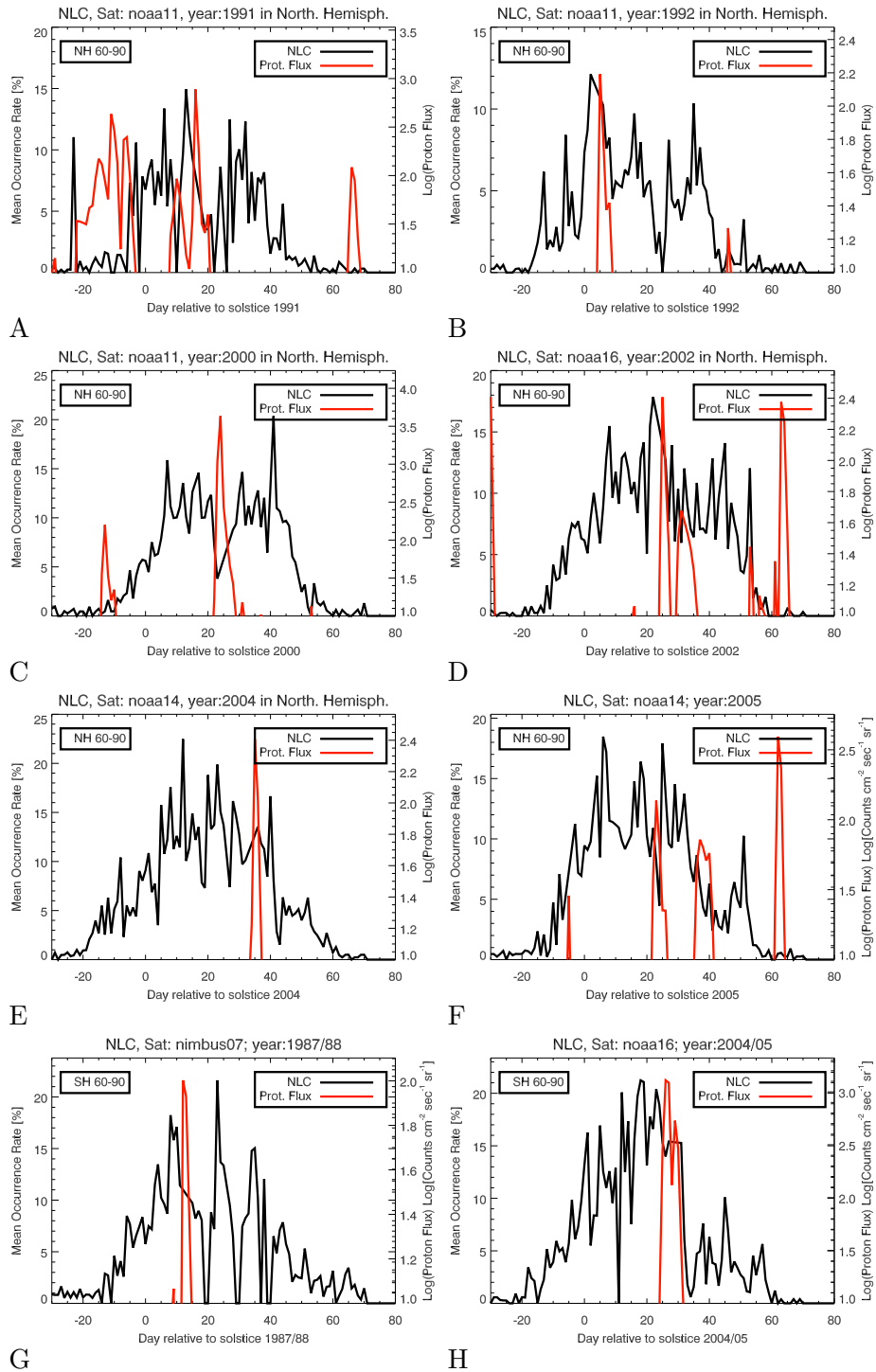


Figure 5.1: A-H: Zonally and daily averaged NLC occurrence rate time series (black line) for NLC seasons with SPEs. The solar proton flux (Channel 2: 5-10 MeV) is plotted for the same season (red line) using a logarithmic scale.

The NLC season begins about 30 days before solstice and can last for up to 90 days. Therefore, there are about 180 days of NLC observations during the entire year. That means that only a fraction of $90/180 \approx 50\%$ of all SPEs occur during the NLC seasons are equally distributed throughout the year. Using only the core NLC season which we define as solstice to 40 days after solstice, then only 20% of all SPEs can be covered. If there were on average 10 SPEs per year occurring during the active period of the Sun, then the outcome would be 2 SPEs for both NLC seasons. This is certainly a small number for an statistical ensemble. A result calculated for such an ensemble, would be very difficult to interpret in terms of underlying physical processes and effects, which we would like to unfold in such manner. But looking at individual SPEs, even few, might deliver a strong indication of a relationship between the proton flux enhancement observed in the Earth's atmosphere and depletion of NLCs in the mesopause region. In this case a long-term data set should be used to better identify any possible random features that could affect the result. Examples of some NLC seasons in the northern and southern hemispheres are shown in Fig. 5.1. The solar proton flux (red line) corresponds to the proton energy channel 2 (5 – 10 MeV) and the black line is the mean zonal NLC occurrence rate for the latitude range $60^\circ - 90^\circ$ derived from SBUV observations. The majority of SPE enhancements correspond visually to depletion of NLCs. On the other hand we can also observe depletion of NLCs without any solar proton event as seen in Fig. 5.1 (panel B) for the year 1992 for the day ≈ 25 relative to solstice. Such complicated behaviour may lead to reduced correlation coefficients for SPEs and NLCs time series.

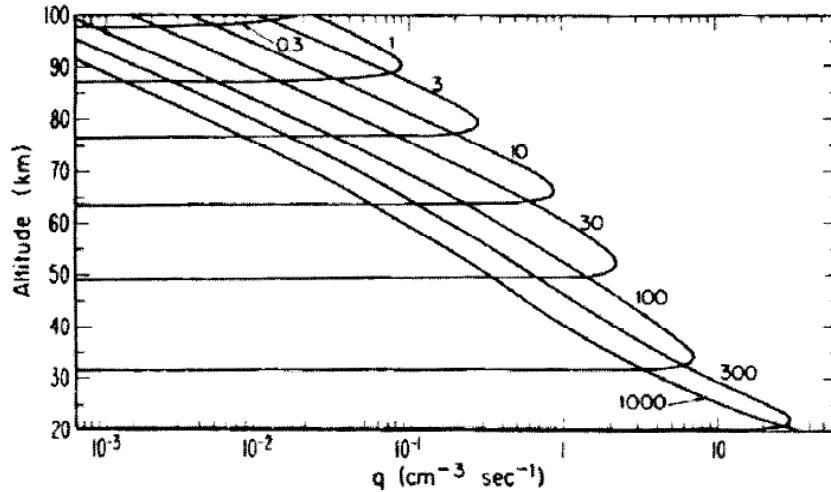


Figure 5.2: Penetration and ionization altitude range of energetic proton particles depending on the kinetic energy [MeV]. Taken from Jackman and McPeters (2004).

The proton flux measurements used in this study were performed by SEM (Space Environment Monitor) instruments on the GOES series (GOES 5 to GOES 12). SEM is a subsystem onboard the GOES satellites performing in-situ measurements of X-ray intensity, energetic particle fluxes and the magnetic field. For our purpose we use the proton energy channels 2 – 7. Channel 1, corresponding to proton energies between 1 and 5 MeV can be contaminated with trapped, magnetospheric protons, and therefore is not useful for our applications. Measurements with channels 2 – 7 are corrected for the impact of trapped protons and are called 'corrected integral proton fluxes'. These channels cover

proton energies ranging from 5 to 100+ MeV, corresponding to energy deposition altitudes between about 75 km and 30 km, respectively (See Fig. 5.2). The use of proton fluxes for energy ranges with energy deposition altitudes well below NLC altitude is mainly driven by the consideration, that the physical mechanism causing the NLC depletion is likely initiated by the catalytic O₃ depletion in the mesosphere (Becker and von Savigny, 2010) and not caused by a direct effect at NLC altitude. The effect of using different SEM channels on the results of this analysis are discussed in detail in section 5.3.

Two prominent cases have been found for the entire data set during the NLC core season. These are the SPEs of 14th of July 2000 (Bastille Day Storm) (Jackman et al., 2001) and of 16th – 22nd of January 2005. For these two cases the detection of proton flux enhancement has been observed throughout all energy channels of the GOES instrument. If we want to find any connection between SPEs and NLCs then using the of 5 – 30 MeV energy range for the solar proton flux should be sufficient. This kinetic energy range corresponds to deposition of highly energetic protons in the altitude range of 50 – 70 km (See Fig. 5.2) (Jackman and McPeters, 2004).

5.2 Correlation method

For this work we perform a cross-correlation analysis between the temporal derivatives of NLC and proton flux time series within a finite time window (with widths between 15 and 30 days) centered at the SPE investigated. The analysis is applied to both the NLC occurrence rate and the albedo residual time series. The main reason for using the derivatives of the NLC (dNLC) and the proton flux time series (dSPE) (Figure 5.3) is that the time lag between a possible cause in the proton flux time series and a possible consequence in the NLC time series can then be estimated after a reduction during or shortly after an SPE more reliably. If there is no recovery in the NLCs time series, the time lag for which the extreme cross-correlation value is assumed depends on the width of the window used for the cross-correlation analysis.

In Fig. 5.4 the cross correlation function for a given scanning window (here 25 days) versus the time lag of the July 2000 SPE is drawn. The extremum in the correlation coefficients r_c and its time lag t_c are the two parameters being used in the following analysis. These parameters have been calculated by applying a Gaussian fit (dashed line) to the correlation function. The height and position of the fitted Gaussian curve gives the correlation coefficient r_c and time lag t_c . Time lags of $t_c < -1$ day and $t_c > 15$ days for the extremum of the curve are rejected by this procedure. The positive and negative correlation curves are fitted separately, and therefore both positive and negative correlations are considered. A cross-correlation analysis was also applied to the original time series, without taking derivatives, leading to a strong dependence of the obtained time lags for the extreme correlation coefficients on the length of the time series samples used for analysis. This means that the time lag between two signals will increase with the width of the sliding window (See Fig. 5.6). In order to avoid this artificial feature, we found that the use of derivatives is more appropriate and less sensitive in using different windows widths.

In the next step the extreme correlation coefficients r_c and time lags t_c obtained for different window widths w_i are averaged to yield the mean values \bar{r}_c and \bar{t}_c for a given solar proton event. If SBUV measurements are available from multiple satellites for a single season, then the correlation analysis is performed on any individual time series, and the

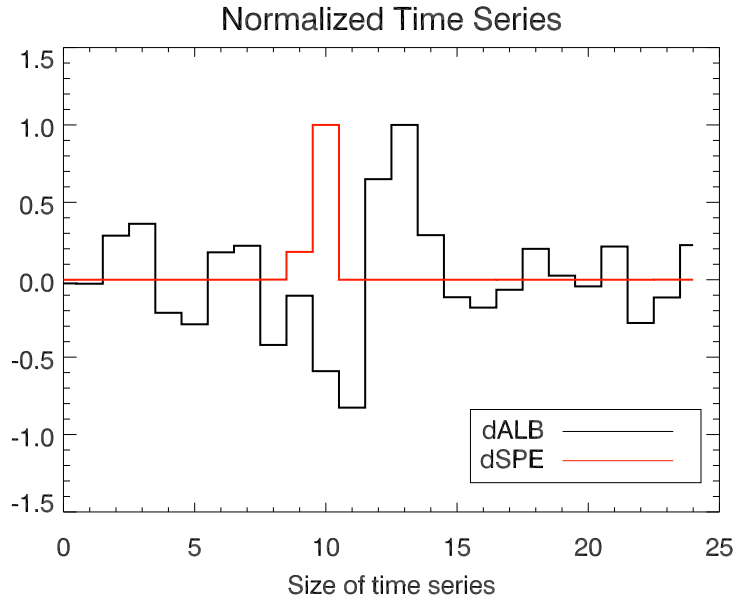


Figure 5.3: Sample normalized dALB and dSPE time series for a window of width 25 days and for the July 2000 SPE. One can see a maximum in dSPE (increase of solar proton flux) and a minimum of the NLC albedo derivative time series (decrease of NLC).

obtained correlation values and time lags are then averaged giving mean values for each season. The computed correlation coefficients (\bar{r}_c) for all SPEs that occurred during the northern and southern NLC seasons covered by SBUV(/2) observations are used to sort those seasons into two main categories, i.e., cases with positive ($\bar{r}_c^+ = \bar{r}_c > 0$) and negative ($\bar{r}_c^- = \bar{r}_c < 0$) correlation coefficients. Since the correlation function can have negative and positive correlation coefficients with different time lags for the same event, we consider only those parameters where the condition $\bar{t}_c(\bar{r}_c^\pm) < \bar{t}_c(\bar{r}_c^\mp)$ is fulfilled.

5.2.1 Statistical Test on Correlated Time Series

In addition a statistical test has been performed by applying the Ebisuzaki method (Ebisuzaki, 1997). Using this algorithm, which correlates resampled time series, we obtain a critical correlation coefficient r_{crit} . The resampling is done by adding a random-phase in Fourier space. Figure 5.7 shows an individual sample random-phase time series. The random-phase resampling is performed 100 times in order to establish r_{crit} , which is the main criterion for randomness of the time series at a given confidence level. Here we assume a confidence level of 95 %. If the calculated correlation coefficient r_c is lower than r_{crit} ($|r_c| < |r_{crit}|$) then the null hypothesis is accepted at a given confidence level, i.e., our derived correlation coefficient is then considered a purely random result. If, on the other hand $|r_c| > |r_{crit}|$, then the null hypothesis is rejected and we conclude that our correlation coefficient is statistically significant at the 95 % confidence level.

Figure 5.8 shows the dependence of r_c and r_{crit} as a function of window width for the January 2005 SPE. There is a slight decrease in r_c with increasing window width, but the condition $|r_c| > |r_{crit}|$ is fulfilled for all window widths. The dependence of the time lag t_c on window width is shown in Fig. 5.9. In contrast to the previous calculation (Fig. 5.6), the time lag remains constant for all window widths. As already mentioned above,

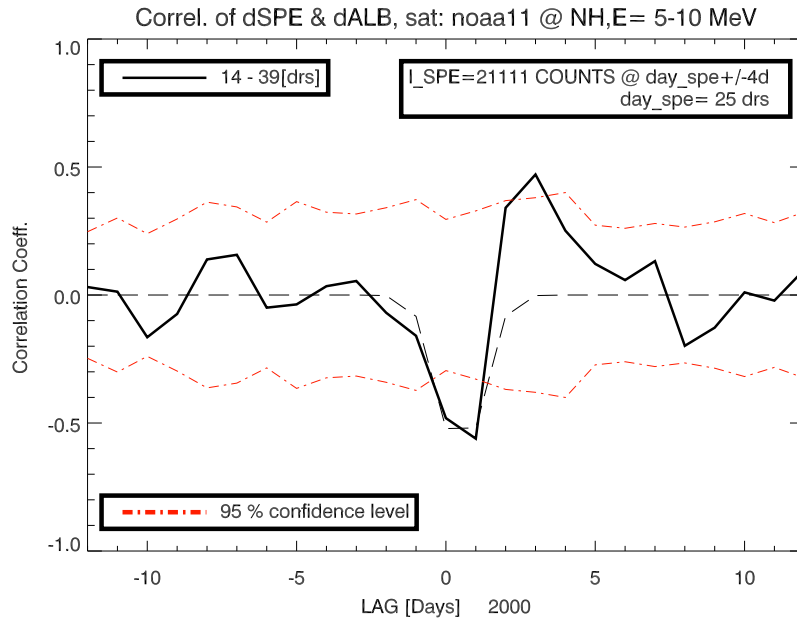


Figure 5.4: Sample cross-correlations of proton flux and albedo time series (derivatives dSPE & dALB) as a function of time lag for the July 2000 SPE, and a sliding window with a width of 25 days. The black dashed line is the Gaussian fit applied to the minima of the curve.

this is the main reason for using the derivatives of the proton flux and NLC time series rather than the original time series themselves. In the following we restrict the analysis to a window width range between 20 and 30 days, since it was found that this range delivers reliable results.

One has to be aware of the fact that the random-phase test is inappropriate for time series with lag-1 autocorrelation coefficients (β) close to 1, because then the test becomes too liberal (Ebisuzaki, 1997). Since in our case the low frequencies are poorly resolved, we only use time series with β lower than a certain threshold (here: $|\beta| < 0.75$). As demonstrated by Ebisuzaki (1997) the random-phase test allows for reliable significance testing for β values below 0.75.

5.2.2 Summary of Analysis

We now summarize the steps taken to determine the final parameters r_c and t_c :

1. The time series are daily and zonally averaged, latitudinally binned, as well as optionally smoothed (with a 3-day box-car).
2. Derivatives of proton flux, NLC albedo and occurrence rate time are determined.
3. Only increasing parts (dSPE $>$ 0) of the proton flux time series are used.
4. Cross-correlations of dSPE and dALB as well as dSPE and dNLC time series as a function of time lag are determined for different window widths w_i .
5. Application of the Ebisuzaki-method to obtain r_{crit} .
6. Determination of r_c and t_c for a given window w_i based on Gaussian fits for $r >$ 0 and $r <$ 0 separately.

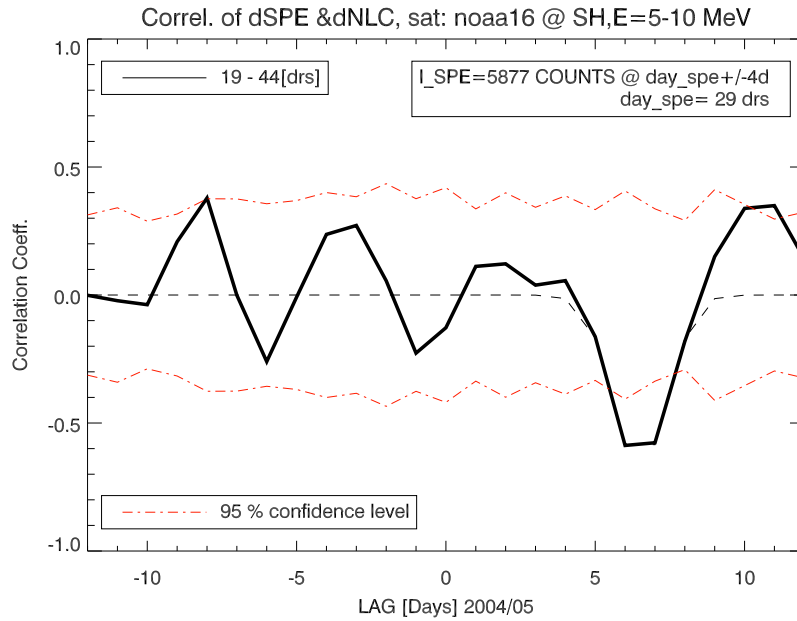


Figure 5.5: Same as 5.4 but for the January 2005 in the southern hemisphere.

7. Cases with time lags $t_c < -1$ and $t_c > 15$ days are not considered.
8. Calculation of mean values (\bar{r}_c, \bar{t}_c) by averaging over results for different window widths w_i .
9. Only cases with $|\bar{r}_c| > |\bar{r}_{crit}|$ are considered further.
10. Of the values $\bar{r}_c^+ > 0$ and $\bar{r}_c^- < 0$ for the same event only the one with shorter time lag is considered.
11. If \bar{r}_c and \bar{t}_c values are available from NLC measurements with different satellites for a given season, these are averaged yielding all-instrument means, where the standard deviation is an estimator for differences between individual satellites.

This procedure is applied to the times series for all northern and southern hemisphere NLC seasons – between 1986 and 2008 – in which at least one SPE occurred.

5.3 Results

Figure 5.10 shows scatter plots of the correlation coefficients and the time lags obtained by applying the analysis procedure discussed in the last section for the 5 MeV proton energy channel. The same plot for the 10 MeV proton energy channel is shown in Fig. 5.11. For the higher proton energies the number of data points is smaller, because these energies are reached by less SPEs. There are also cases with positive correlation coefficients – which is to be expected, given that NLCs are also affected by other processes. However, the majority (>60%) of correlation coefficients is negative. We can see, that for most of the SPEs the correlation coefficients are around $\bar{r}_c = -0.5$. There is no obvious dependency of time lag \bar{t}_c on \bar{r}_c . The time lags in Fig. 5.10 vary between 0 and 8 days. Important questions are, whether the observed range of time lags is consistent with an SPE-induced

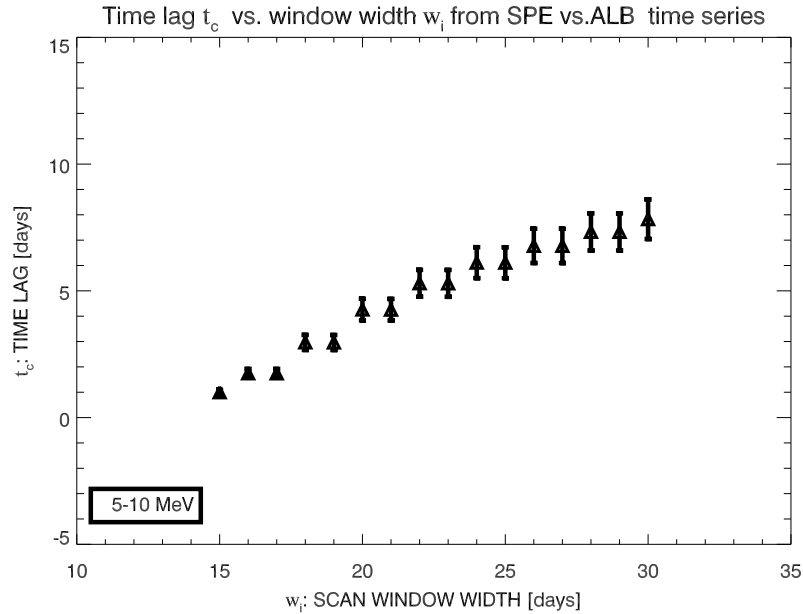


Figure 5.6: Dependence of the obtained time lag of the negative correlation extremum on window widths (here 15 – 30 days) for the January 2005 SPE and no derivation of the time series. As we can see, there is a strong increase of the time lag from $t_c = 1$ day for a 15-day window to $t_c = 8$ days for a 30-day window.

effect, and whether it is conceivable that time lags as long as 5 – 8 days can be caused by an SPE.

First we have to note that the durations of the individual SPEs vary between about 3 and about 8 days. Secondly, the temporal evolution of the ozone depletion and the subsequent dynamical effects associated with the precipitating particles during the SPE will strongly depend on the temporal variation in proton fluxes, which may also differ significantly from SPE to SPE. Some SPEs show pronounced double peak or even triple peak structures in the proton fluxes. Due to these reasons we expect that SPE induced effects are associated with a certain range of time lags. The model simulations by Becker and von Savigny (2010) show that the summer mesopause heating starts essentially with the proton flux enhancements, but the maximum heating is observed at the end of the anomalous mesospheric cooling period (assumed to last 5 days) caused by reduced diabatic heating due to catalytic ozone losses.

Fig. 5.12 and 5.13 show scatter plots of the calculated cross-correlation coefficients \bar{r}_c as a function of Ev_{prot} for the NLC albedo time series and the 5 – 10 MeV and the 10 – 30 MeV energy channel respectively. Ev_{prot} is the total integrated proton flux for a given energy channel during the SPE. As can be seen in Fig. 5.13, for the 10 – 30 MeV proton channels, the negative cross – correlation coefficients appear to decrease with increasing proton flux. For the 5 – 10 MeV channel this behaviour is not as pronounced.

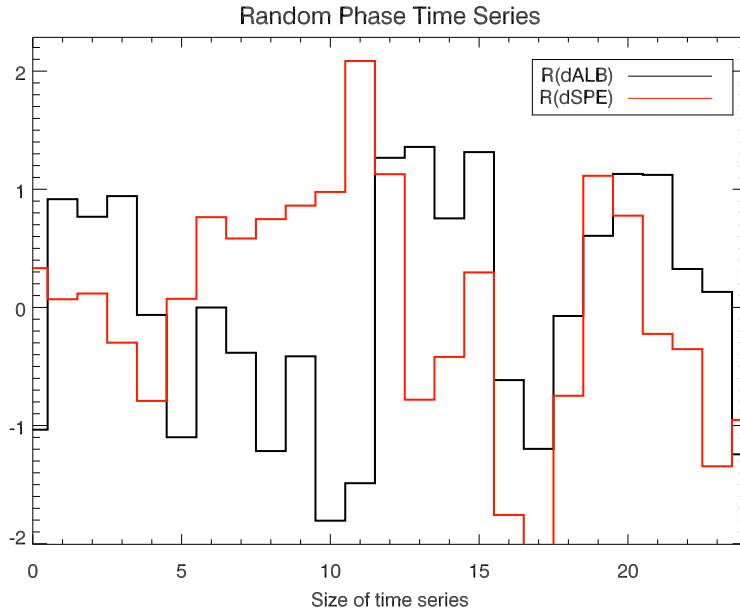


Figure 5.7: Example of resampled dALB and dSPE time series for a window of width 25 days. The phase of each sample is randomized between $R \cdot 2\pi - \pi$ where R is a random number $R \in [0,1]$. An ensemble of 100 random time series has been used to derive the critical correlation coefficient r_{crit} .

We note, that there are not only cases with significant negative correlation coefficients, but also a few cases with positive correlation coefficients significant at the 95% confidence level. All other cases with positive correlation coefficients fail the statistical test.

In order to examine the possible influence of smoothing and the choice of energy channel on the derived cross-correlations and time lags, we performed the analysis for all individual proton channels (2 – 7) corresponding to the energy ranges $E=[5-10,10-30,30-50,50-60,60-100,>100 \text{ MeV}]$ with and without smoothing. The smoothing applied was a convolution with a 3-day box-car function. Tables 5.1 and 5.2 show the analysis results for the July 2000 SPE, and the January 2005 SPE, respectively. As expected, the correlation coefficients as well as the lag-1 autocorrelation values β increase if the smoothing is applied. Note, that the correlation coefficients are statistically significant at the 95% confidence level even for the unsmoothed time series. For the July 2000 SPE (Table 5.1) the time lag \bar{t}_c is almost independent of the energy channel used and not strongly affected by the smoothing, either. For the January 2005 SPE (Table 5.2) the smoothing and choice of energy channel has a stronger influence on the derived time lags. For the unsmoothed case the time lag decreases with increasing energies. With the 3-day smoothing, the time lag remains nearly constant ($t_c \approx 5 - 6$ days) throughout all energy ranges. For the January 2005 SPE there is a general tendency of decreasing correlation coefficients for increasing energy.

In tables 5.3 and 5.4 the derived parameters for the cases that passed the statistical test are shown. Note, that only correlations with proton energy channel 2 (5 – 10 MeV) are shown. For most SPEs the proton fluxes in the higher energy channels are only weakly enhanced or not enhanced at all during the SPE, rendering a correlation analysis impossible. Only for the two strongest SPEs (July 2000 and January 2005, see Tables 5.1 and 5.2) the proton fluxes were elevated for all proton energy channels. The time lag

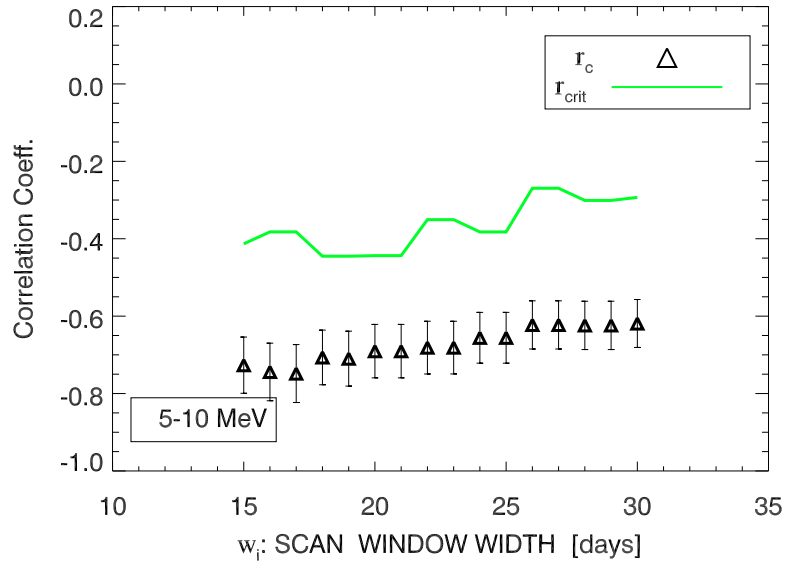


Figure 5.8: Comparison of negative r_c and r_{crit} for different widths of the scanning window for the January 2005.

seems to differ for albedo and NLC data for some cases, in particular the seasons 1990 and 2002 in the NH and 1987/88 in the SH. For the January 2005 and July 2000 SPEs the calculated parameters show no deviation.

The total number of SPEs with proton flux of $E_{v_{prot}} \geq 50$ counts $\text{cm}^{-2} \text{s}^{-1} \text{sr}^{-1}$ depends strongly on the energy channel. The total number of SPEs during the NLC core season for the northern and southern hemisphere is shown in Table 5.5. The overall results for both the NLC albedo and occurrence rate time series are shown in Table 5.5 and are as follows: In the northern hemisphere a total of 20 SPEs occurred during the NLC seasons, 12 of which occurred during the core NLC season (days 0 to 40 with respect to solstice). Of the 13 SPEs occurring during southern hemisphere NLC seasons, only 7 occurred during the core NLC season. Here we took all the relevant SPEs that occurred between the years 1986 – 2008. The correlation coefficients for the NLC albedo time series are statistically significant at the 95% confidence level for 8 out of 12 cases for energy channel 2 and the smoothed time series in the northern hemisphere and 4 out of 7 cases for channel 2 and the smoothed case in the southern hemisphere. Using unsmoothed time series generally leads to a smaller number of significant cases. If the NLC occurrence rate time series are used, then similar numbers of significant cases are obtained, as shown in Table 5.5. We also note that the number of statistically significant cases decreases with increasing proton energy. This is likely related to the fact that only for the strong SPEs the proton fluxes are enhanced for the higher energy channels.

Table 5.6 lists the average correlation coefficients R_c and the time lags T_c for all the SPE cases of NLC occurrence rate and albedo time series. The time lag T_c and the time lag range $T_c \pm \sigma_{T_c}$ is smaller for the albedo time series compared to NLC occurrence rate results. Thus, the time lag is sensitive to the data sets used.

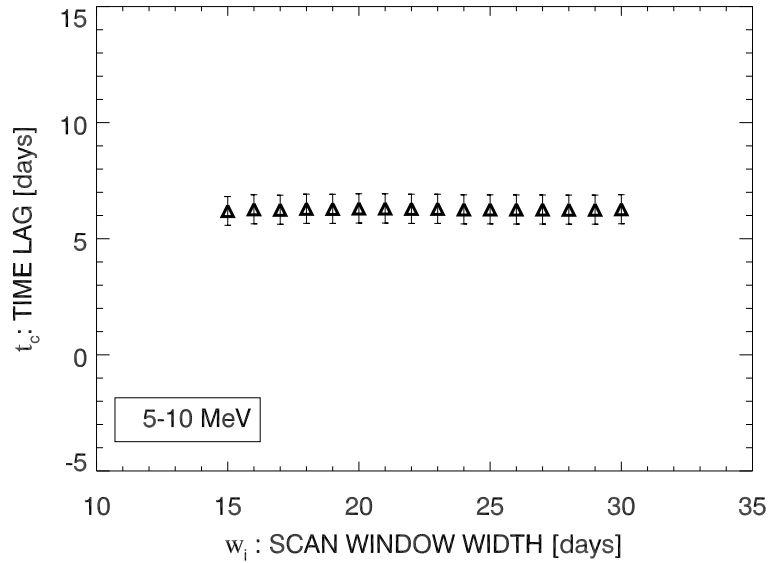


Figure 5.9: Same as Fig. 5.6 except for the derivative of the NLC albedo time series and for a window width range from 15 to 30 days.

5.4 Discussion

We now discuss the general implications of the results presented so far. The observed behaviour in terms of the January 2005 SPE is in line with the observations described by von Savigny et al. (2007a). We also note, that the NLC observations with all SBUV instruments operational during the July 2000 SPE (NOAA 11 and NOAA 14), and January 2005 SPE (NOAA16 and NOAA 17), respectively, show similar reductions in NLC occurrence rate and albedo, making instrumental problems or measurement anomalies of an individual instrument unlikely.

The NLC occurrence rates are quite variable even during times without SPEs, which makes the establishment of a causal relationship between proton precipitation and signatures in the NLC time series difficult in general. Any single point shown in Fig. 5.12 and 5.13 may be spuriously introduced by the high variability of NLCs observed during most seasons – particularly in the southern hemisphere – and may not be related to SPEs at all. However, this variability should also lead to positive cross-correlations. The fact, that only few statistically significant positive correlation coefficients are observed for all SPEs that occurred during the core NLC season of the years 1986 – 2008 may indicate, that the depletion of NLCs by an SPE is not an unusual phenomenon, but occurs frequently. Therefore, the effect described in von Savigny et al. (2007b) may not be an exception.

The depletion of NLCs during and after SPEs is also indirectly suggested by the available model simulations of the effects of precipitating and highly energetic solar protons (Krivolutsky et al., 2006; Jackman et al., 2007; Becker and von Savigny, 2010), which show an increase in the summer mesopause temperatures as a consequence of an induced dynamical effect. Krivolutsky et al. (2006) investigated the impact of the July 2000 SPE on atmospheric temperature and dynamics. Their model produced a temperature increase near the polar summer mesopause of more than 15 K. Near 60 km, where the catalytic O_3 depletion due to SPE-produced HO_x is strongest by a temperature decrease of up to 8 K is

E[MeV]	\bar{r}_c	σ_{r_c}	\bar{t}_c [d]	σ_{t_c}	r_{crit}	β	Smoothing
5-10	-0.59	0.01	0.51	0.01	-0.33	0.30	N
5-10	-0.70	0.02	0.31	0.01	-0.42	0.64	Y
10-30	-0.59	0.01	0.51	0.01	-0.33	0.30	N
10-30	-0.70	0.02	0.34	0.01	-0.44	0.64	Y
30-50	-0.59	0.01	0.51	0.01	-0.33	0.30	N
30-50	-0.74	0.03	0.51	0.01	-0.46	0.66	Y
50-60	-0.74	0.02	0.64	0.01	-0.38	0.30	N
50-60	-0.74	0.03	0.63	0.01	-0.47	0.66	Y
60-100	-0.62	0.01	0.68	0.02	-0.38	0.30	N
60-100	-0.74	0.03	0.74	0.01	-0.47	0.66	Y
>100	-0.59	0.01	1.51	0.01	-0.34	0.30	N
>100	-0.73	0.02	0.93	0.01	-0.46	0.66	Y

Table 5.1: Correlation results of NLC albedo time series and proton fluxes for different proton energies and for the July 2000 SPE. \bar{r}_c is the cross-correlation coefficient, σ_{r_c} is standard error of \bar{r}_c , \bar{t}_c is the time lag, σ_{t_c} is its standard error. r_{crit} denotes the critical correlation coefficient, and β corresponds to the lag-1 autocorrelation value of the NLC albedo time series. The last column indicates whether the NLC albedo and the proton flux time series were smoothed (by a 3-day box-car function) or not.

modelled. Although Jackman et al. (2007) and Krivolutsky et al. (2006) presented model simulations for different SPEs, and the absolute values of the modelled summer mesopause temperature increases are different, both model studies are in qualitative agreement, i.e., both show essentially no temperature changes in the winter hemisphere, but (a) a temperature decrease in the mesosphere caused by a reduction in solar heating due to catalytic ozone destruction, (b) a dynamically induced apparent heating of the summer mesopause region caused by a reduction in adiabatic cooling due to smaller vertical (upward) motion. Unfortunately, there are no published model simulations of the temperature response of the polar summer mesopause during the January 2005 SPE.

We must also point out that satellite observations of NLCs during the July 2000 SPE were also performed by SNOE (Student Nitric Oxide Explorer) (Bailey et al., 2005) and the SNOE NLC occurrence rates do not exhibit a very strong signature in mid-July 2000 that may be a consequence of the energetic particle precipitation. This may be explained by the higher sensitivity of SNOE in comparison to the SBUV/2 instruments, which can detect even faint NLCs, whereas SBUV/2 is only capable of detecting the brightest NLCs. It cannot be excluded, though, that a decline of the NLC occurrence rate at $70 \pm 5^\circ\text{N}$ around July 14 may be related to the SPE. Interestingly, Bailey et al. (2005) find a discontinuity in NLC altitude around the time of the July 2000 SPE, with a sudden decrease of NLC altitudes of about 1 km, but it is not clear how SPE induced effects may introduce a discontinuity in NLC altitude. This effect is possibly due to an SPE induced effect on the tangent height retrievals based on the Rayleigh-knee in the limb radiance profiles at 215 nm (Merkel et al., 2001).

5.5 Conclusions

The effect of energetic solar protons associated with SPEs on NLCs was investigated using the SBUV NLC data set (covering the period from 1978 – 2008) and GOES SEM proton flux measurements available since 1986. Unfortunately, SPEs are rare phenomena and

E[MeV]	\bar{r}_c	σ_{r_c}	$\bar{t}_c[d]$	σ_{t_c}	r_{crit}	β	Smoothing
5-10	-0.65	0.03	6.27	0.02	-0.35	0.29	N
5-10	-0.81	0.03	6.86	0.02	-0.36	0.56	Y
10-30	-0.64	0.01	4.45	0.01	-0.36	0.29	N
10-30	-0.81	0.03	6.82	0.02	-0.36	0.56	Y
30-50	-0.53	0.01	4.52	0.01	-0.35	0.29	N
30-50	-0.81	0.03	6.82	0.02	-0.36	0.56	Y
50-60	-0.42	0.02	2.97	0.71	-0.33	0.29	N
50-60	-0.76	0.03	6.37	0.03	-0.40	0.56	Y
60-100	+0.57	0.01	0.48	0.01	0.30	0.29	N
60-100	-0.63	0.01	5.18	0.03	-0.39	0.56	Y
>100	-0.46	0.02	3.59	0.01	-0.35	0.29	N
>100	-0.70	0.01	4.33	0.01	-0.42	0.56	Y

Table 5.2: Same as Table 5.1 but for the January 2005 SPE.

there were a total of only 12 SPEs occurring during the core NLC season (days 0 to 40 with respect to solstice) in the northern hemisphere and 7 SPE cases in the southern hemisphere for the solar proton energy range of 5 – 10 MeV. Most of these SPEs are associated with a decrease in the NLC occurrence rate and albedo time series. The mean correlation coefficient for all cases with statistically significant negative correlations for the NLC occurrence rate and albedo time series is $R_c = -0.62$ and the time lag is in the range of $T_c = 0 - 8$ days (Table 5.6). With few exceptions, all of the statistically significant cross-correlation coefficients are negative. But the overall number of significant cases is limited, i.e., 67 % for the northern hemisphere and 57 % for the southern hemisphere.

The evidence provided by the SBUV observations and the physical mechanism leading to a mesopause temperature increase during SPEs established with model simulations (see Becker and von Savigny (2010)) may suggest that a depletion of NLCs during SPEs is likely a frequent phenomenon. However, considering (a) the high intrinsic variability of the thermal conditions at the polar summer mesopause, (b) the fact that for most of the SPEs the observed reduction in NLC occurrence rate or albedo is not very strong, we cannot claim that our study shows that NLCs are affected by every SPE. The reasons for why this effect has not been observed much earlier are probably the limited number of SPEs during NLC seasons, and the relatively large intrinsic variability of the summer mesopause region, particularly in the southern hemisphere. Further and detailed model simulations are required in order to quantify the different contributions of direct heating by dissipating gravity waves, heating/cooling by advection and adiabatic heating due to a dynamically induced reduction in adiabatic cooling near the summer mesopause. NLCs may then be employed to study dynamically induced temperature responses to energetic particle preprecipitation.

(Day) [drs]	Year	Data	$E_{ch.}$	\bar{r}_c	σ_{r_c}	$\bar{t}_c[d]$	σ_{t_c}	r_{crit}	β
(10)	1990	NLC	2	+0.51	0.01	4.56	0.01	0.40	0.53
(10)	1990	ALB	2	+0.51	0.02	4.56	0.02	0.44	0.54
(35)	1990	ALB	2	-0.51	0.08	0.39	0.02	-0.43	0.41
(10)	1991	NLC	2	-0.56	0.04	1.12	0.01	-0.44	0.54
(17)	1991	NLC	2	-0.84	0.11	8.48	0.01	-0.40	0.56
(17)	1991	ALB	2	-0.51	0.02	3.27	0.02	-0.44	0.52
(4)	1992	ALB	2	-0.58	0.04	4.26	0.08	-0.50	0.70
(25)	2000	NLC	2	-0.66	0.03	-0.50	0.01	-0.47	0.60
(25)	2000	ALB	2	-0.70	0.04	0.31	0.04	-0.42	0.65
(22)	2002	NLC	2	-0.55	0.07	5.24	0.15	-0.42	0.68
(22)	2002	ALB	2	-0.58	0.04	3.18	0.08	-0.47	0.74
(33)	2002	NLC	2	-0.59	0.06	1.26	0.12	-0.42	0.34
(33)	2002	ALB	2	+0.54	0.21	2.00	7.36	0.40	0.35
(34)	2004	NLC	2	-0.59	0.10	7.69	0.42	-0.35	0.49
(34)	2004	ALB	2	-0.65	0.12	7.81	0.52	-0.36	0.49
(23)	2005	NLC	2	-0.57	0.13	9.79	0.16	-0.42	0.64
(23)	2005	ALB	2	-0.58	0.18	3.68	5.07	-0.43	0.51
(38)	2005	NLC	2	+0.63	0.19	10.12	2.10	0.39	0.66
(38)	2005	ALB	2	-0.73	0.02	1.44	0.02	-0.50	0.56

Table 5.3: Analysis results for the SPEs that occurred during the northern hemisphere NLC seasons for proton energy channel 2 (5 – 10 MeV) and smoothing with a 3-day boxcar, which have passed the statistical test. drs stands for day relative to solstice. NLC (ALB) refers to the NLC occurrence rate (albedo) time series.

Day [drs]	Year	Data	$E_{ch.}$	\bar{r}_c	σ_{r_c}	$\bar{t}_c[d]$	σ_{t_c}	r_{crit}	β
(13)	1987/88	NLC	2	-0.78	0.03	-0.50	0.01	-0.44	0.61
(13)	1987/88	ALB	2	-0.68	0.02	2.94	0.01	-0.41	0.56
(40)	1990/91	ALB	2	-0.56	0.06	5.80	0.04	-0.37	0.61
(5)	2001/02	NLC	2	-0.66	0.20	8.27	2.13	-0.40	0.56
(5)	2001/02	ALB	2	+0.80	0.09	10.03	2.01	-0.42	0.45
(10)	2001/02	NLC	2	-0.53	0.12	7.58	0.02	-0.39	0.44
(10)	2001/02	ALB	2	+0.67	0.08	10.94	0.18	0.18	0.53
(21)	2001/02	NLC	2	-0.45	0.07	7.87	7.07	-0.39	0.58
(21)	2001/02	ALB	2	-0.55	0.13	5.14	6.29	-0.42	0.55
(29)	2004/05	NLC	2	-0.70	0.12	5.98	1.12	-0.39	0.56
(29)	2004/05	ALB	2	-0.75	0.09	6.06	1.08	-0.36	0.56

Table 5.4: Same as Table 5.3 but for the SPEs that occurred during the southern hemisphere NLC seasons.

Energy Range [MeV]	Channel	N_{SPE}	N_{core}	N'_{NLC} (N^*_{NLC})	N'_{ALB} (N^*_{ALB})
North. Hem.					
5-10	2	20	12	4 (7)	5 (8)
10-30	3	20	9	4 (6)	4 (6)
30-50	4	20	1	- (1)	1 (1)
50-60	5	20	1	1 (1)	1 (1)
60-100	6	20	1	1 (1)	1 (1)
>100	7	20	1	1 (1)	1 (1)
South. Hem.					
5-10	2	13	7	4 (5)	4(4)
10-30	3	13	6	3(3)	4(4)
30-50	4	13	2	1 (1)	2(1)
50-60	5	13	1	1 (1)	1(1)
60-100	6	13	1	1(1)	-(1)
>100	7	13	1	1(1)	1()

Table 5.5: Results of the NLC data analysis. N_{SPE} is the total number of SPEs occurring during all NLC season considered (Channel 2); N_{core} is the number of SPEs occurring during the all core NLC season (with proton flux $Ev_{prot} \geq 50$ counts $\text{cm}^{-2} \text{s}^{-1} \text{sr}^{-1}$) and N'_{NLC} (N^*_{NLC}) corresponds to the number of statistically significant cases with negative correlation coefficients for unsmoothed (smoothed) NLC occurrence rate time series. The corresponding numbers for the NLC albedo time series are N'_{ALB} (N^*_{ALB})

Hemisphere	Data	R_c	T_c
North	NLC	-0.62 ± 0.08	4.73 ± 4.11
North	ALB	-0.61 ± 0.08	3.04 ± 2.44
South	NLC	-0.62 ± 0.13	5.84 ± 3.65
South	ALB	-0.64 ± 0.10	4.99 ± 1.42

Table 5.6: The correlation coefficients R_c and time lags T_c are averages for all cases with statistically significant negative correlation coefficients. NLC and ALB refers to NLC occurrence rate time series and NLC albedo time series, respectively.

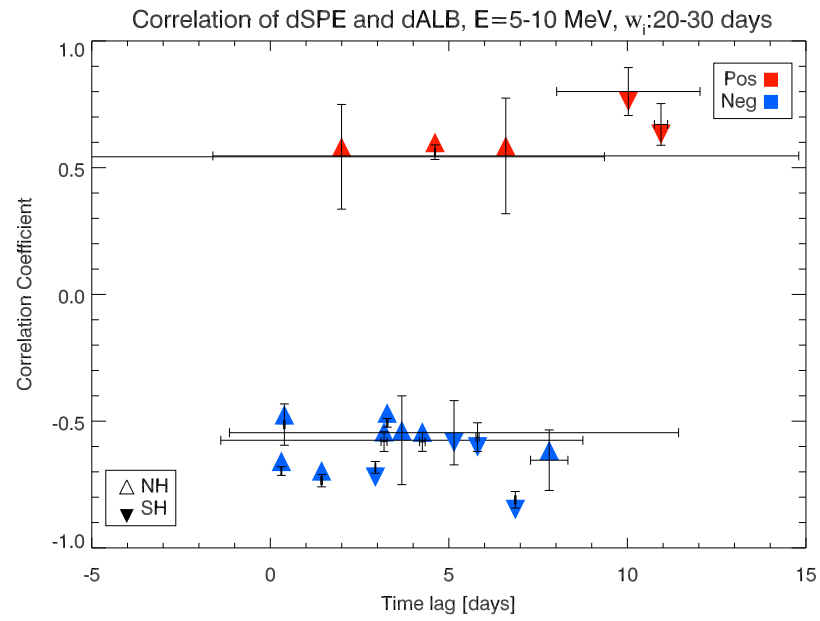


Figure 5.10: Scatter plot of \bar{r}_c (correlation coefficient) and \bar{t}_c (time lag) for all the SPEs during the NLC core season (days 0 to 40 with respect to solstice), for the NLC albedo time series and for energy channel 2.

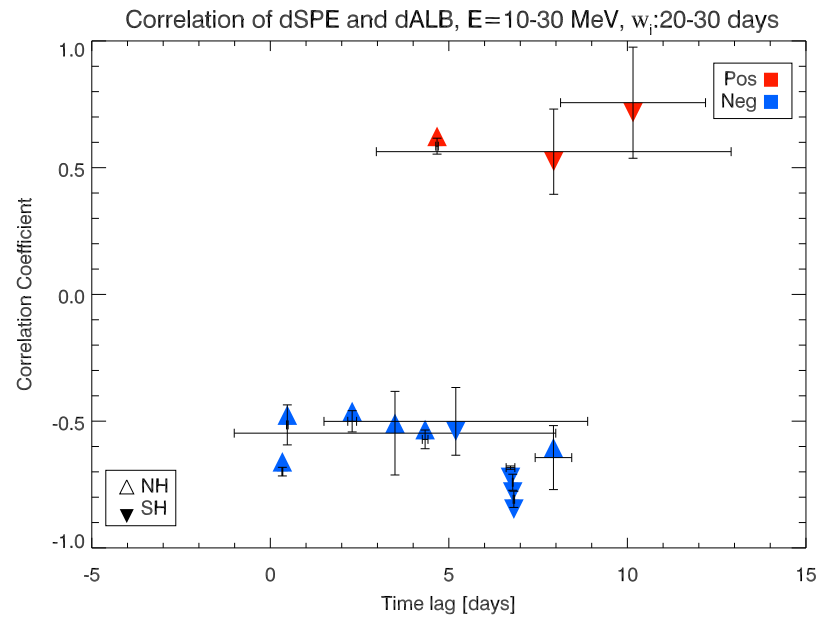


Figure 5.11: Same as figure 5.10 but for energy channel 3.

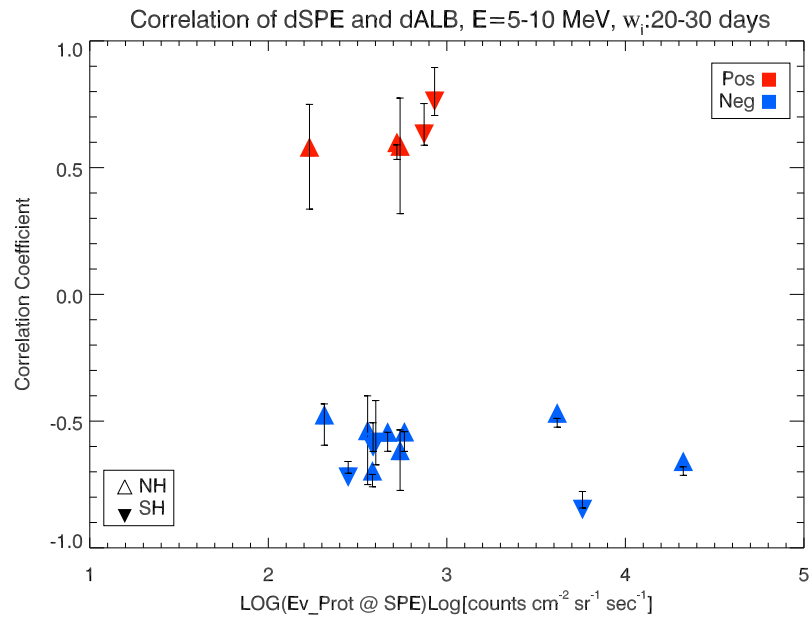


Figure 5.12: Scatter plot of \bar{r}_c (correlation coefficient) and proton flux $E_{v_{prot}}$ for all the SPEs during the NLC core season, for the NLC albedo time series and for proton energy channel 2.

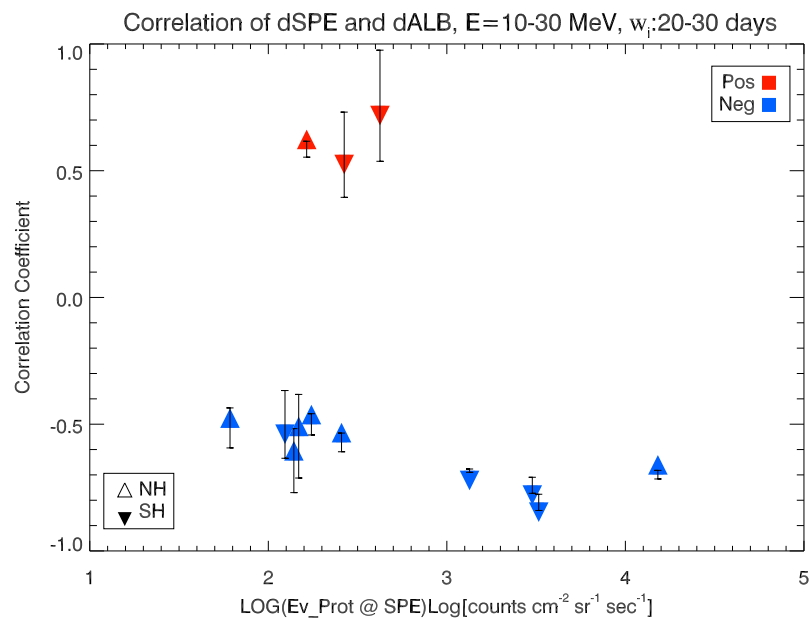


Figure 5.13: Same as figure 5.12 but for proton energy channel 3.

Chapter 6

Planetary Wave Activity in the Mesopause Region

The results of an analysis of temperature data from MLS (Microwave Limb Sounder), NLC occurrence frequency, NLC albedo residuals and NLC radiance from two independent satellite instruments (SCIAMACHY on Envisat and SBUV/2 on NOAA) between the years 2004 – 2009 are presented and discussed. The analysis during the summer hemisphere seasons indicates the presence of characteristic temperature peaks at the polar summer mesopause typically occurring at the end of January/July each year in the southern/northern hemisphere. We find that these temperature peaks coincide with enhanced quasi 2-day wave activity showing maximum amplitudes up to 9 K at mid-latitudes in the southern hemisphere. The effect is consistent with the idea that the quasi 2-day wave slows down the residual meridional circulation, leading to reduced adiabatic cooling at the polar summer mesopause. Since NLCs react sensitively to temperature changes, planetary wave (PW) activity may be another important driver for variations in NLCs, particularly during the second half of the NLC season.

6.1 Introduction

Investigations of Q2DW (quasi-2 day wave) signatures in temperature, zonal and meridional wind components in the middle atmosphere were made by different groups over the past 4 decades (Muller and Kingsley, 1974; Glass et al., 1975; Craig et al., 1985; Clark, 1989; Harris, 1994; Poole and Harris, 1995; Meek, 1996; Azeem et al., 2001; Gurubaran et al., 2001; Namboothiri et al., 2002; Nozawa et al., 2003; Schröder and Schmitz, 2004; Limpasuvan et al., 2005; Baumgaertner et al., 2008). These studies showed clearly that the Q2DW is a member of large scale planetary wave class which occurs in the summer hemisphere after summer solstice. The Q2DW has been assumed to be one of the resonant eigenmodes or Rossby gravity normal modes in a windless isothermal atmosphere (Salby, 1981). Another explanation for the excitation of planetary waves has been suggested by Plumb (1983). They analysed the dynamical effect of meridional winds that is dependent on the mean zonal wind perturbations, which can lead to baroclinic instability in the upper stratosphere and thus lead to excitation of planetary waves. The source for the Q2DW is then thought to be coming from instability of the polar jet (Prata, 1984). There are radar wind measurements from the ground as well as temperature measurements in the upper stratosphere and mesosphere showing similar Q2DW effects (Rodgers and Prata, 1981; Burks and Leovy, 1986), as well as rocketsonde wind measurements near the stratopause.

Wu et al. (1993) found a strong occurrence of the Q2DW in mesospheric winds using the High-Resolution Doppler Imager (HRDI) onboard the Upper Atmosphere Research Satellite (UARS). The characteristics of the 2-day wave simulated in numerical studies are in good agreement with the observations (Hunt, 1981; Hagan et al., 1993). These experiments suggest that the Q2DW is a westward traveling wave phenomenon with a zonal wavenumber 3 ($S = 3$). Herein the Q2DW is not restricted to $S = 3$, since Q2DWs with $S = \pm 2$ and 4 have been found as well. The Q2DW amplitude in the southern hemisphere is stronger by a factor of 2 compared to its northern hemisphere summer counterpart. The observed period was found to vary from 42 to 55 hours, and phase locking to local time has been found in both hemispheres (Craig and Elford, 1981; Clark, 1989).

The objective of this chapter is to investigate the wave patterns in mesospheric temperature data retrieved from the MLS (Microwave Limb Sounder) on the Aura satellite at mid-latitudes in the summer hemisphere and to compare them with the temperature increase in the polar summer mesopause region. This is motivated by a model calculation of planetary wave activity by Norton and Thuburn (1996) showing the 2-day wave at mid-latitudes affecting the Eliassen-Palm flux divergence (See Fig. 6.1). The impact of the PWs opposes the effect of GW drag and accelerates the westward zonal flow which leads to weakening of the meridional wind and warming of the polar mesopause region due to reduced upwelling (See Chapter 2.2).

Since the NLC's response to temperature variation is very strong, we expect to find similarities in the wave patterns in temperature and NLC albedo residuals or NLC radiance. We focus mainly on the planetary scale waves, e.g. the westward propagating Q2DW with ($S = 2; 3$) and Q5DW (Quasi 5-day wave) with ($S = 1$) around the mesopause. The MLS temperature data set that we use extends from the year 2004 to 2009 and the same time period is used for the SCIAMACHY and SBUV/2 NLC data. Since NLCs occur only during the summer period, we restrict the analysis to the period between June – August in the northern hemisphere and December – February in the southern hemisphere.

6.2 Wave Analysis

In this section we provide an overview of the analysis method we have been using to extract the wave signatures in temperature and NLC data.

6.2.1 Least Square Fitting

We employ a spectral analysis procedure based on least-squares fitting (LSF) as described in Wu et al. (1995). If we assume that temperature and NLC time series y_i for a given space-time period have wave-like structures, then fitting of a wave function allows to extract wavelength, wavenumber and the direction of the propagation of the wave signatures. In Figure 6.2 an example of wave pattern in temperature data is shown, which have been derived directly from the data. The temperature values correspond to the deviation from the mean. A wave pattern can be observed also at larger longitudes for the days 387 – 390. The propagation of the 3 wave crests is westward and with a time interval of ≈ 2 days between two maxima at a constant longitude. This wave pattern is referred to the westward propagating quasi 2-day wave with wavenumber 3 (Q2DW, $S = 3$). We employ a length of 10 days for the fitting window. This is a compromise between time resolution

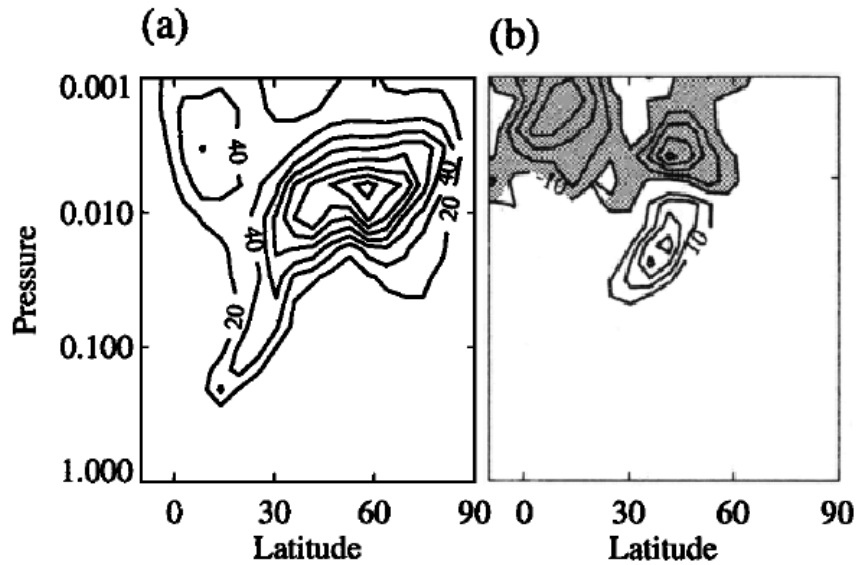


Figure 6.1: For 1 July: (a) zonal mean gravity wave drag, contour interval 20 m/s/day; (b) EP flux divergence, contour interval 10 m/s/day. Shaded region less than -10 m/s/day. Taken from Norton and Thuburn (1996).

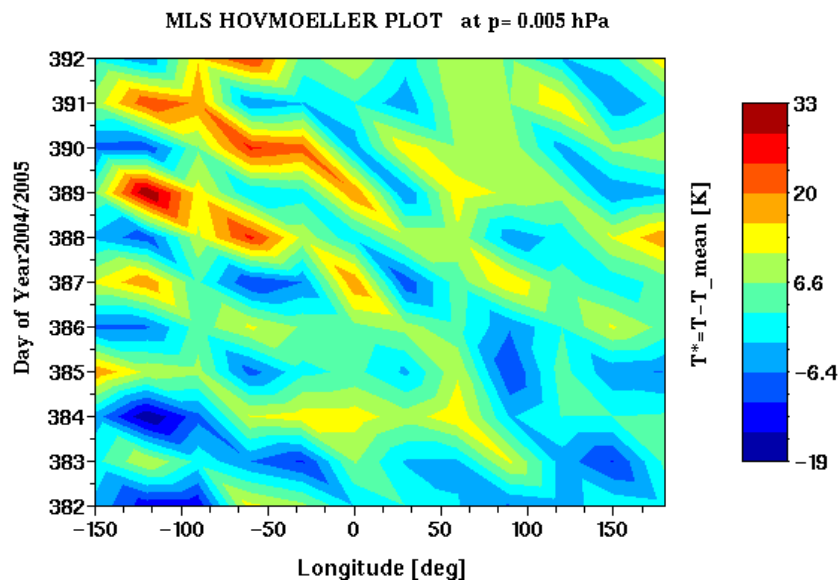


Figure 6.2: Hovmöller plot of temperature signatures around day 387 of the season 2004/05 in the southern hemisphere for the latitude band 35°S – 40°S. The wave pattern with 3 maximas moves westward. The temperature crests seen as local maxima in the wave pattern have a time difference of ≈ 2 days. Thus we observe a quasi 2-day wave propagating westward with wavenumber 3.

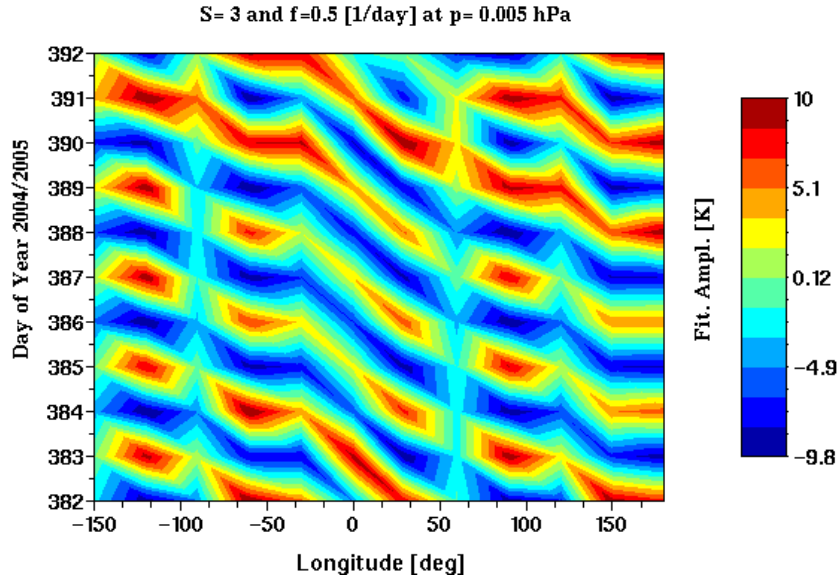


Figure 6.3: Hovmöller plot of fitted model parameters for a given combination of $f=0.5$ [1/day] and $S=3$ to the original temperature deviation values as shown in Fig. 6.2.

and frequency in the accounted wave scales, since we are interested in planetary wave activity features having periods on the order of several days (Baumgaertner et al., 2008). By fitting the model with apriori given parameters like frequency f and wavenumber S to the data y_i (See Fig. 6.3), the unknown coefficients A and B of the model can then be extracted by χ^2 -minimization of the following relation:

$$y_i = A \cdot \sin(2\pi(ft_i + S\lambda_i)) + B \cdot \cos(2\pi(ft_i + S\lambda_i)) \quad (6.1)$$

Here t_i and λ_i are the Universal Time (UT) in days and longitude of each data point $y(\lambda_i, t_i)$ scaled to cover the range $\lambda_i = 0 \dots 1$. The results are the fitted coefficients A and B which are used to calculate the amplitude of the wave for a given pair of frequency and wavenumber. The amplitude of the wave is defined as:

$$Amp(f, S) = \sqrt{A^2 + B^2} \quad (6.2)$$

The same procedure has been applied on temperature precision values for the estimation of errors of the wave amplitudes for a given wavenumber and frequency combination. A maximum error on the order of ≈ 0.65 K and ≈ 0.42 K have been estimated for the Q2DW and Q5DW respectively. Thus a wave amplitude on the order of > 1.67 K and > 1.07 K is highly significant at a confidence level of 99% for the Q2DW and Q5DW, respectively.

6.2.2 Application of the LSF-Method

The temperature data that we have used span the time period between Dec 2004 – Aug 2009. In this case we have a total of 5 southern hemisphere NLC seasons and 5 northern hemisphere NLC seasons. For the northern hemisphere we used the time period between days 145 – 235 of year and days 340 – 415 of year for the southern summer hemisphere. In Figure 6.4 we can see the two prominent Rossby normal mode candidates, the Q2DW

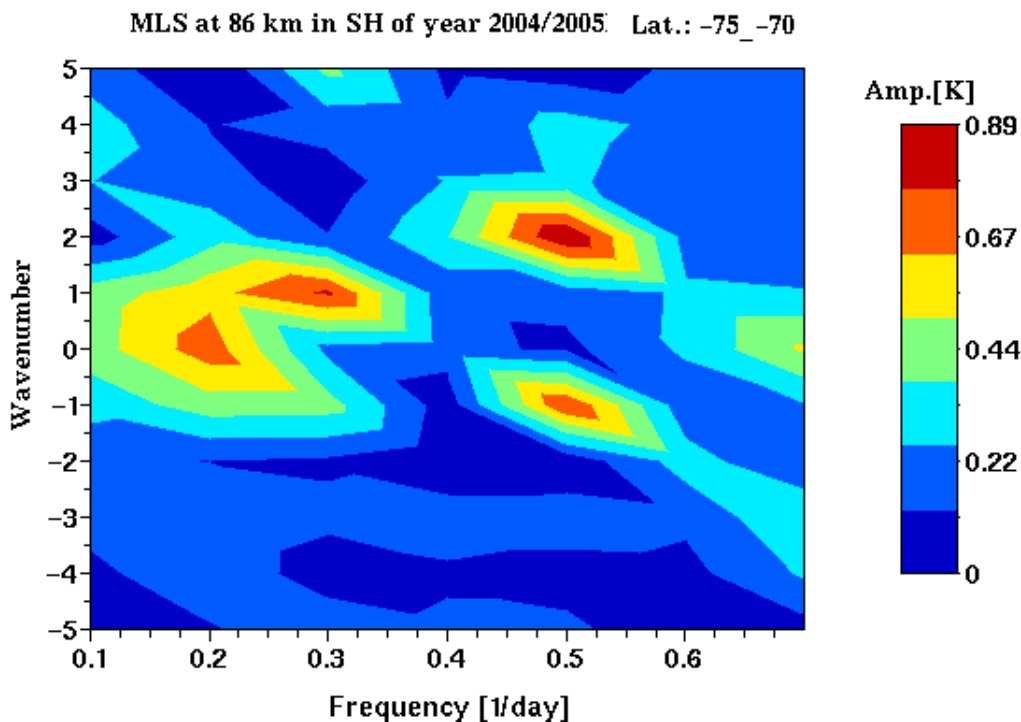


Figure 6.4: Appearance of wave signatures in temperature data using MLS Aura for days 377 – 383 of the season 2004/05 in the southern hemisphere at 60°S – 75°S.

propagating with wavenumbers $S = (\pm 2; -1)$ and the Q5DW with $S = (0; 1)$ during the days 377 – 383. A spectral peak signal of wave signature is statistically significant at confidence level of 95%, if the ratio of its magnitude to that of the local background spectrum is > 2.1 (See Wilks (2006), chapter 8 and Table B.3) for degrees of freedom of $DOF > 6$. In Fig. 6.5 the same is plotted for different sub-periods of the period day 377 to day 408 of the season 2004/05 in the southern hemisphere. The plots illustrate the range of variability in Q2DW activity over periods of a few days. Weaker aliases can be seen in the spectrum such as the counterpart of Q2DW eastward propagating wave with $S = -2$. The aliases are either real signatures of eastward propagating wave patterns, an information leakage from the $S = (2; 3)$ Q2DW signatures or originates from the spectrum analysis itself (See Wu et al. (1993)). The temperature Q2DW shows westward/eastward propagating waves with wavenumbers $S = 2$ and $S = -1$ respectively in the mid of January 2005 (Fig. 6.5 panel a – c). At the end of January 2005 there is a wavenumber transition of westward propagating Q2DW from $S = 2$ to $S = 3$ and $S = -1$ to $S = -2$ in temperature data (Fig. 6.5 panel e – f).

Similar wave features can be seen in NLC radiance and albedo residuals data if we apply the same wave fitting procedure (See Fig. 6.6 – 6.8). The two strong features, i.e. the westward propagating Q5DW and Q2DW which are significant at 95% confidence level can be observed in the SCIAMACHY data in Fig. 6.6. In SCIAMACHY NLC radiance data the wavenumber transition for the Q2DW is not as prominent as in MLS temperature data. A range of different wavenumbers for the Q2DW can be observed with peak signals at $S = (-1; \pm 2; 3)$ in the mid of January and $S = (2; 3)$ at the end of January/begin of February (Fig. 6.7 panels a – f).

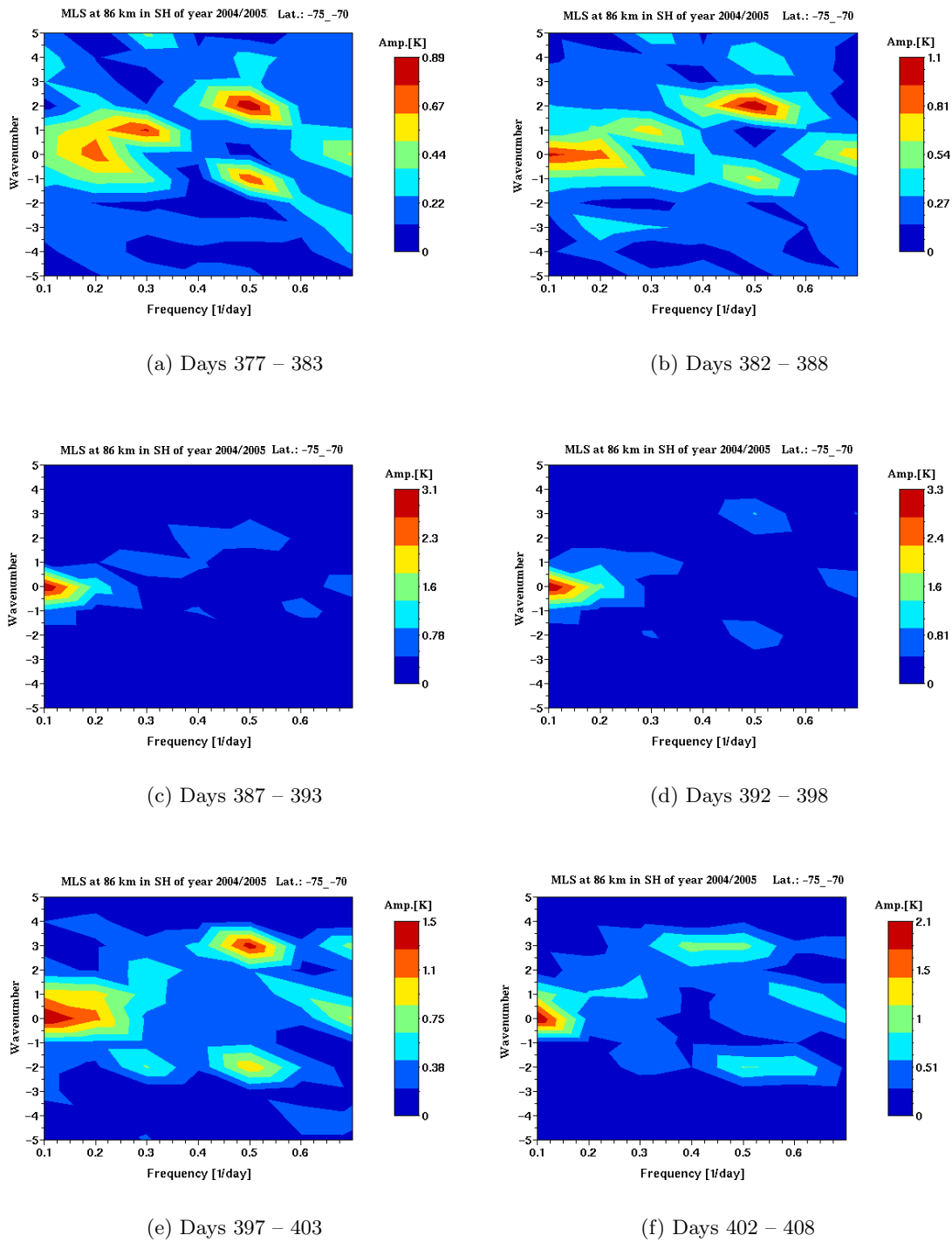


Figure 6.5: Wavenumber frequency plot of MLS Aura temperature data for different days of the season 2004/05 in the southern hemisphere of 65°S – 75°S latitude.

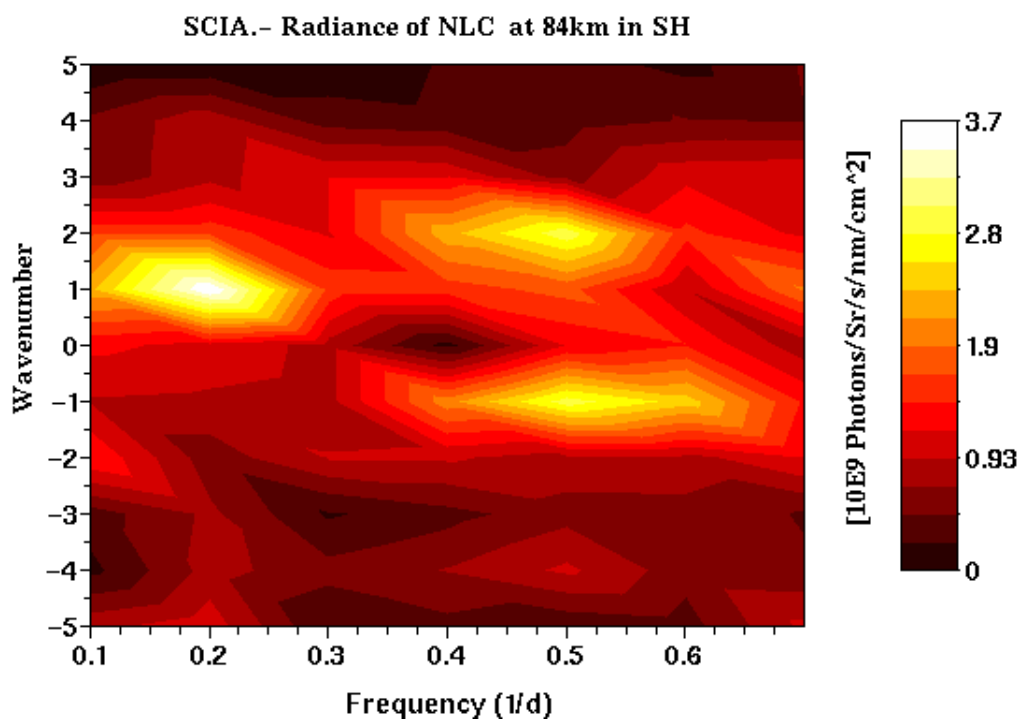


Figure 6.6: Wavenumber frequency plot of NLC radiance using SCIAMACHY data for days 392 – 398 of the season 2004/05 in the southern hemisphere and in 65°S – 75°S latitude range.

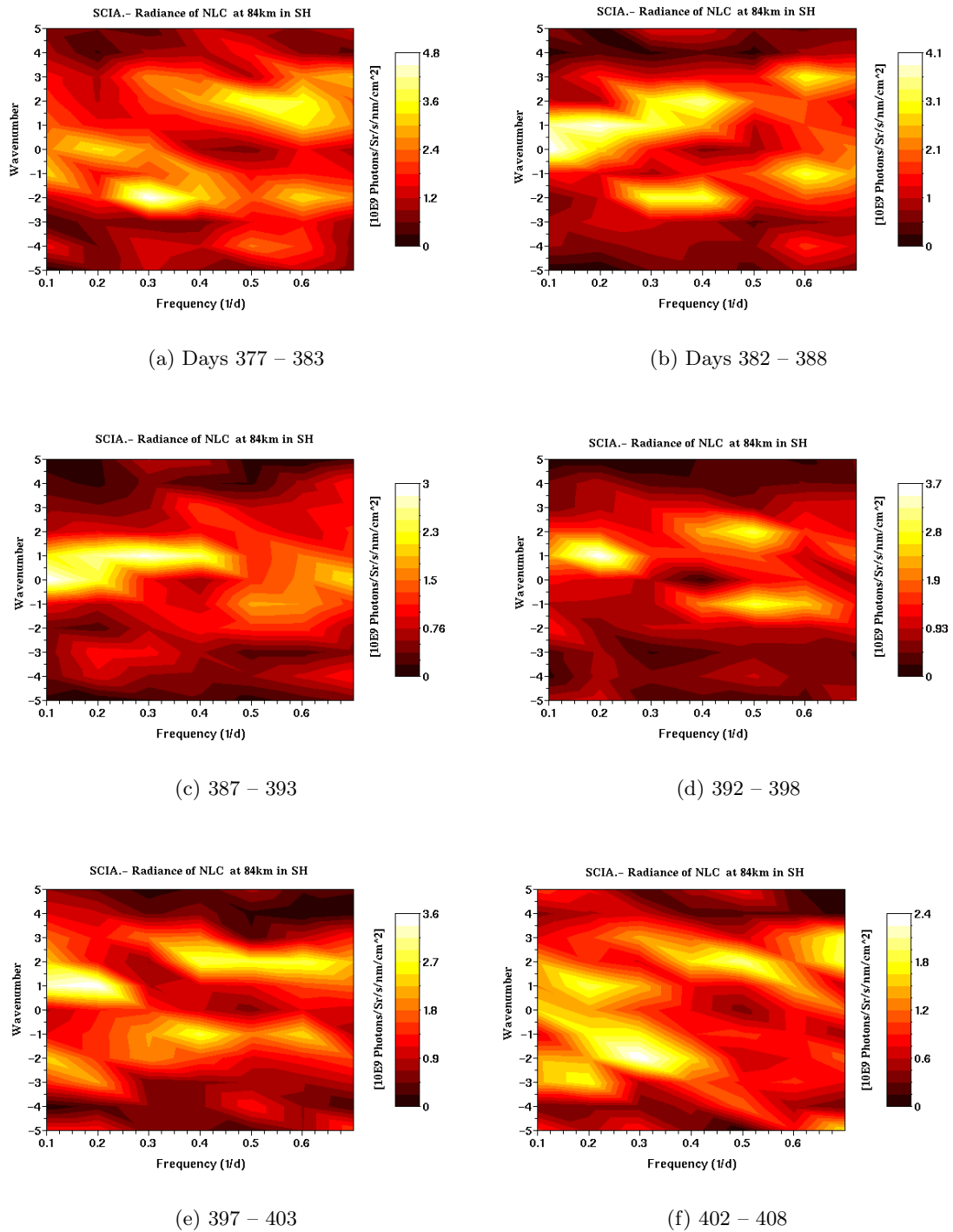


Figure 6.7: Same as Fig. 6.6 but for different days from top left to bottom right.

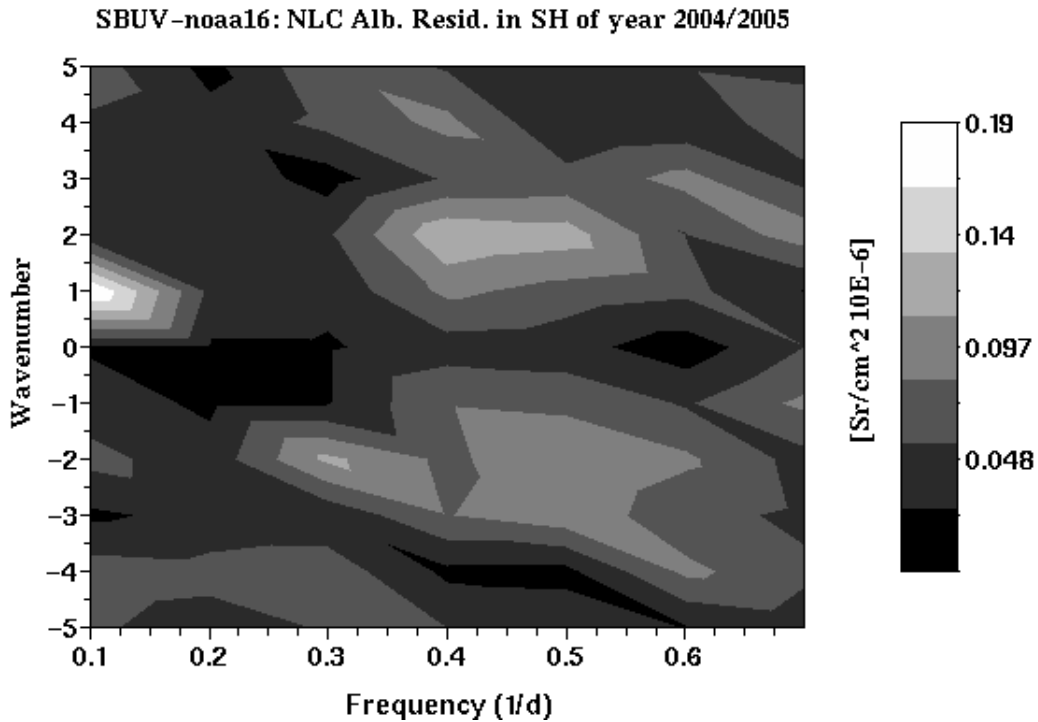


Figure 6.8: Wavenumber frequency plot of NLC residual albedo using SBUV/2 NOAA – 16 data for days 387 – 392 of the season 2004/05 in the southern hemisphere.

In SBUV/2 NLC albedo residual data the Q5DW is observable (Fig. 6.9 panel a) but it is not as pronounced as in SCIAMACHY data. The reason, why the Q5DW signature is visible in the analysis of SCIAMACHY data and not in the SBUV data, is most likely, that SCIAMACHY performs observations in limb mode and is much more sensitive than the nadir-viewing SBUV instruments. The eastward component of the Q2DW counterpart with $S = (-1; -2)$ can be observed in both independent NLC data (Fig. 6.9 panels a – c). The Q2DW in the SBUV/2 data shows peak signatures with wavenumbers $S = (2; -1)$ in the mid of January and $S = \pm 2$ at the end of January. There is no Q2DW peak observable at the beginning of February 2005 in SBUV/2 data (Fig. 6.9 panels e – f), since SBUV/2 with its nadir-viewing geometry is less sensitive to the NLC signal in comparison to the SCIAMACHY limb measurements.

The non-linear interaction of the Q2DW with diurnal tides can lead to a range of further wavenumbers, i.e., Q2DW eastward wave $S = (-1; -2)$ which originates from the superposition of Q2DW westward $S = (2; 3)$ and diurnal tide (Palo et al., 2007). A westward/eastward propagating Q2DW with $S = \pm 2$ have been found by Morris et al. (2009) using the groundbase PMSE data (Davis, Antarctica) and MLS data and by Merkel et al. (2008) who used the NLC data from the SNOE satellite. In a test analysis only MLS observations made on the sunlit side of the Earth were used ($SZA < 90^\circ$) in order to mimic the sampling of the NLC measurements. This, however, had no effect on the extracted wavenumbers. Since the NLC measurements are dependent on the NLC signal, in opposite to MLS temperature measurements which do not depend on NLC behaviour, this can be regarded as a crucial difference in reproducing same wavenumbers for the same

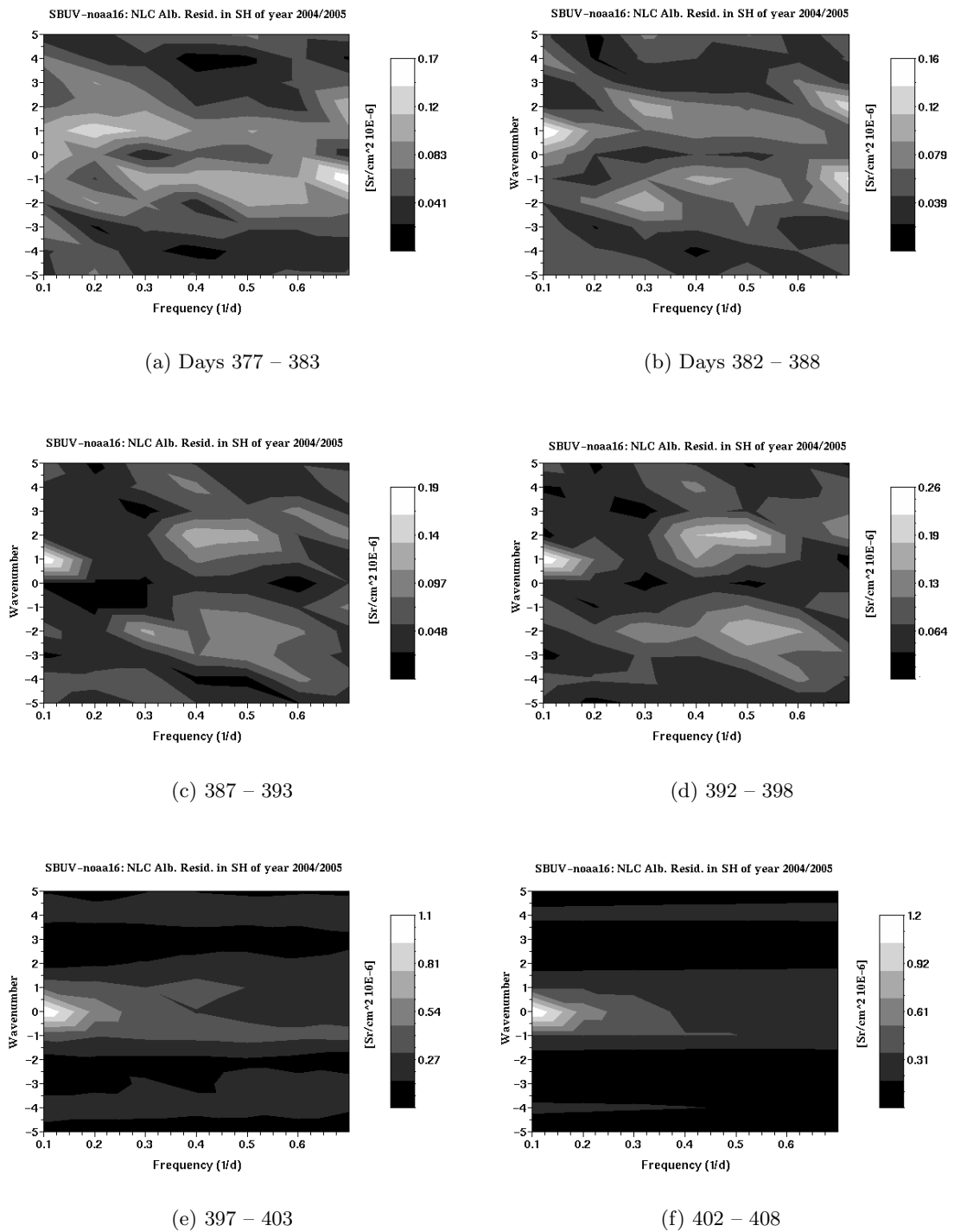


Figure 6.9: Wavenumber frequency plot of planetary wave amplitudes in NLC residual albedo measured with SBUV/2 from SBUV/2 NOAA – 16 data for days 377 – 408 of the season 2004/05 in the southern hemisphere and for the $65^\circ\text{S} - 75^\circ\text{S}$ latitude band.

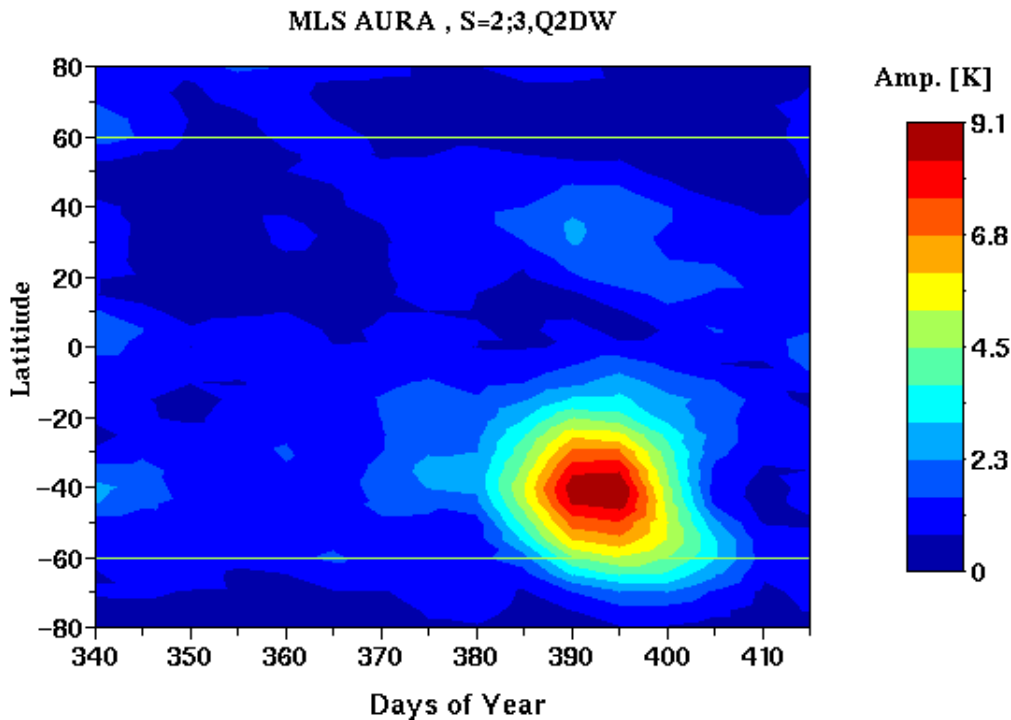


Figure 6.10: Latitudinal extent of the Q2DW for the days 340 – 415 of the season 2004/05. The amplitude of the westward propagating Q2DW ($S = 2; 3$) signature is depicted.

sub-periods. Another aspect must be pointed out, that the SBUV/2 is not sensitive to weak NLC signals, and thus it is impossible to observed wave patterns at the end of the NLC season by SBUV/2 satellite.

6.3 Latitudinal Extent of Q2DW activity

In order to further investigate the association of the observed waves with the mid-latitude Q2DW, the latitudinal extent of the wave is examined. The average amplitude of waves with a period of $T = (40 \text{ h} - 60 \text{ h})$ and wavenumber $S = (+2; +3)$ (westward phase propagation) is depicted and plotted as a function of latitude and days (Fig. 6.10) for the southern NLC season 2004/2005.

In this plot a pronounced Q2DW event can be observed at the end of January 2005 in the southern hemisphere which extends to the beginning of February. For January 2005 the beginning of the wave activity is around the day 382, i.e. January 17. The maximum of the wave amplitude is about 9 K and is assumed on day 395 at $\approx 40^\circ\text{S}$. There is no Q2DW activity after the day 410 of the year 2004. This phenomenon seems to recur every year after summer solstice in the southern hemisphere as has already been reported in several studies (Salby and Callaghan, 2003; Rojas and Norton, 2007; Morris et al., 2009). In Fig. 6.11 (panels a – e) the same characteristics are shown for the five seasons 2004/05 to 2008/2009. A similar pattern of the Q2DW can be observed for all other seasons.

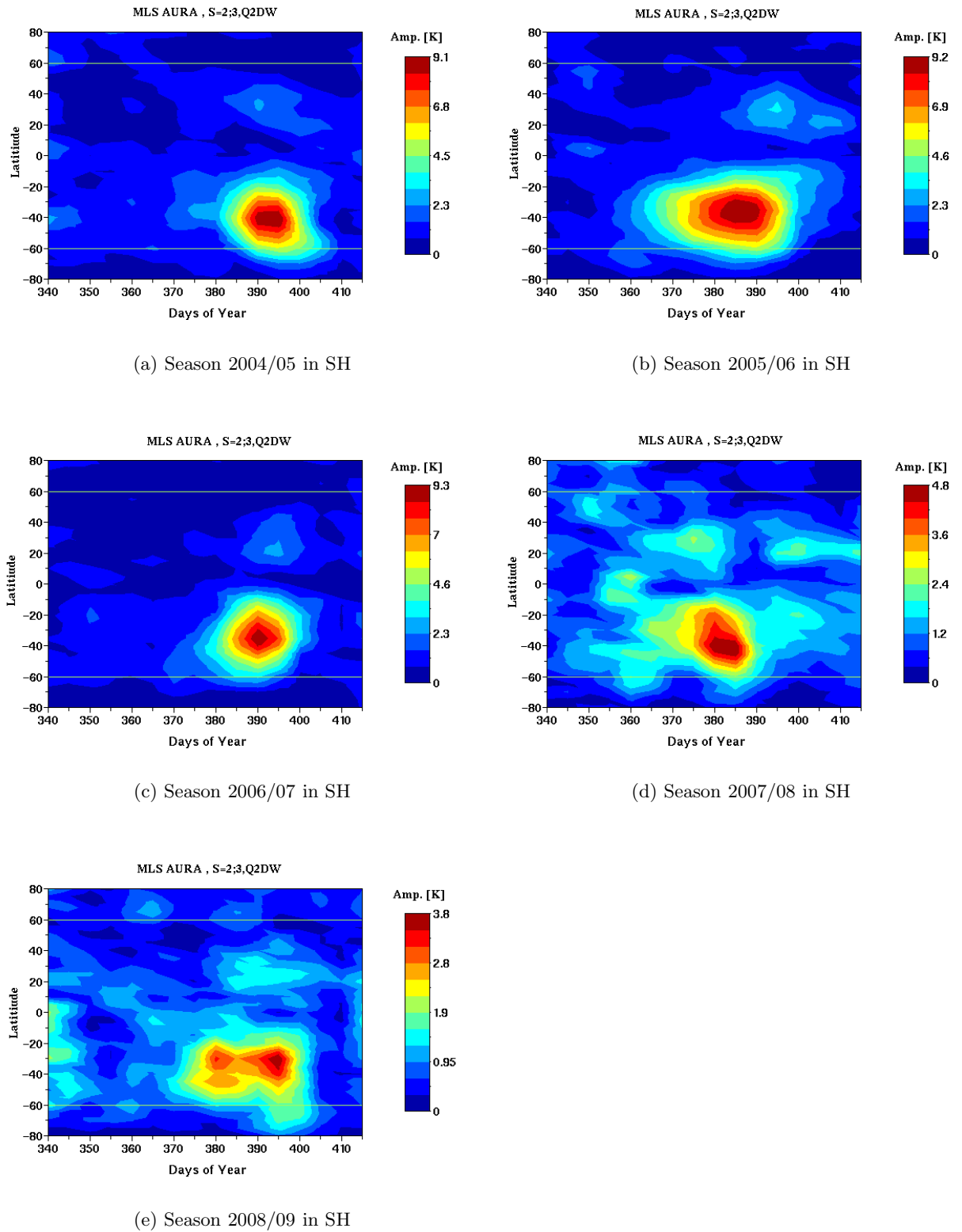


Figure 6.11: Same as Fig. 6.10 but for different seasons in the southern hemisphere.

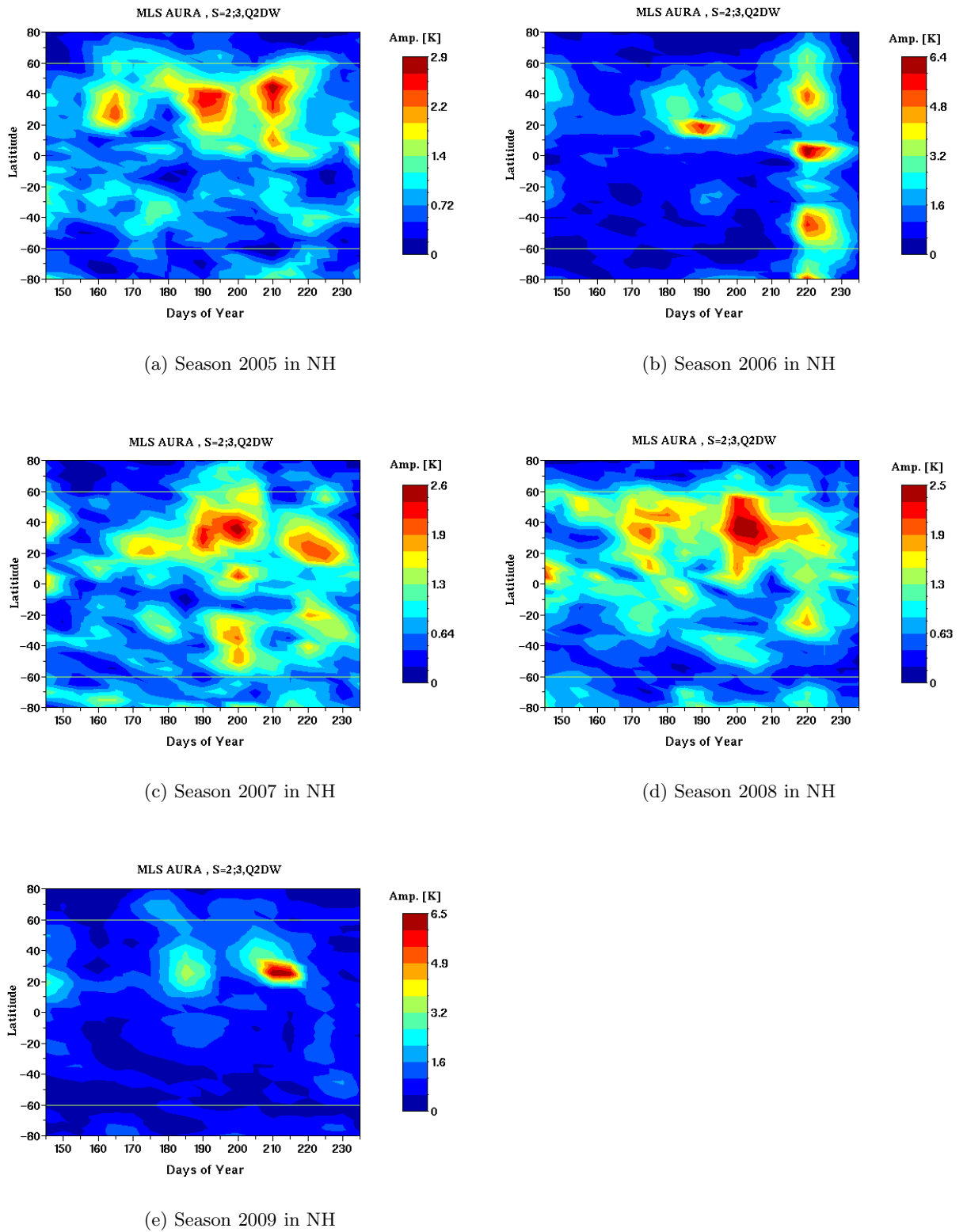


Figure 6.12: Same as Fig.6.11 but for the northern hemisphere.

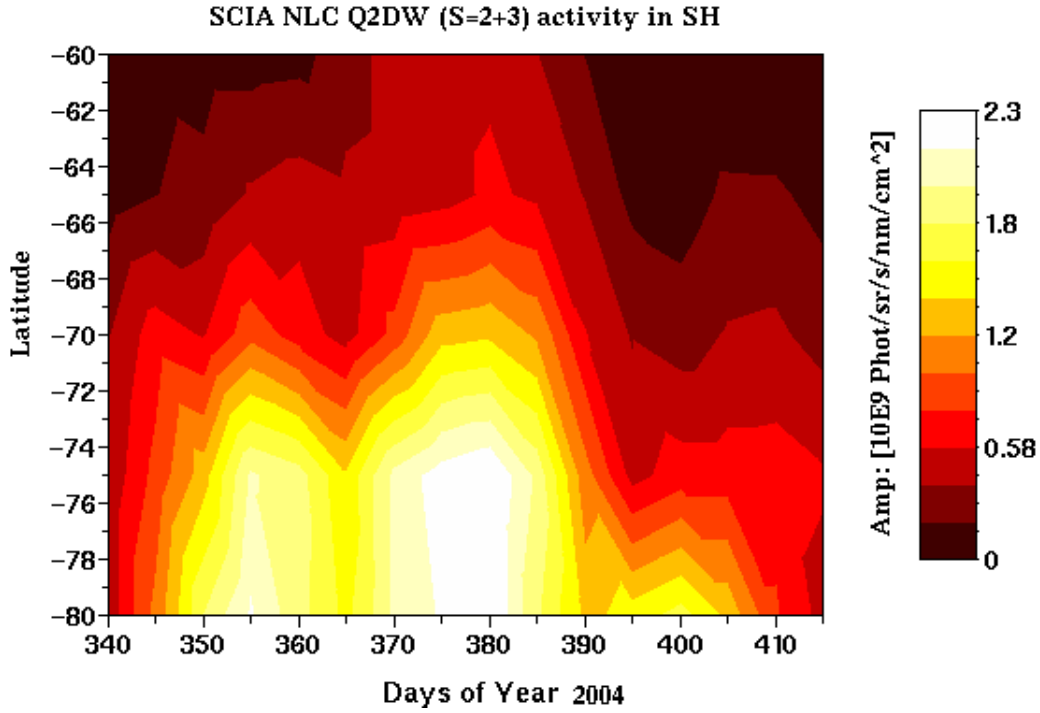


Figure 6.13: Latitudinal extent of the Q2DW for the days 340 – 415 of the season 2004/05 in NLC radiance data from SCIAMACHY. The amplitude of the westward propagating Q2DW (S = 2; 3) activity is depicted from the Figures 6.7 for all latitude and days available.

The wave cell (wave activity period) has different shapes in each season. For the seasons 2004/05 and 2006/07 the cell is regularly shaped and starts around day 380. For the seasons 2005/06 the wave cell is observed ≈ 10 days earlier. In addition the latter wave cell has an elongated shape. Thus the wave activity period seems to be longer in this case. For the seasons 2007/08 and 2008/09 the maximum amplitude is reduced by $\approx 50\%$ compared to earlier seasons and a double structure can be observed in the season 2008/09. The maximum of the wave cell decreases from the season 2004/05 of $T_{max} \approx 9$ K to 3.8 K for the season 2008/09. This may be related to the decrease in solar activity, but since we do not have enough data to make such a statement about solar cycle patterns this is pure speculation. Such clear 2-day wave signatures can not be observed in the northern hemisphere (Fig. 6.12 panels a – e), because the peak wave amplitudes are nearly on the same order as the background noise. At the same time the wave activity period does not seem to occur in the same time period as it is the case in the southern hemisphere. Nevertheless the wave cells can be observed with smaller maxima and several wave cells for the same summer season and at different latitude bands (Seasons 2006/2007/2008).

Since NLCs occur only at polar latitudes, we restricted the latitude range to $\phi = 60^\circ - 80^\circ$ when studying wave signatures in NLCs. The wave signatures in NLCs are controlled by temperature variation and PW activity. Therefore an extended wave period in temperature may result in extended wave activity periods in NLC signatures. In Figure 6.13 we plotted the Q2DW amplitude in NLC radiance for the latitude range of $60^\circ - 80^\circ$ and the season 2004/2005 using the SCIAMACHY data. The Q2DW activity (mainly S = 2; 3) has its maximum on day 380 and begins around day 375 and extends to day 390

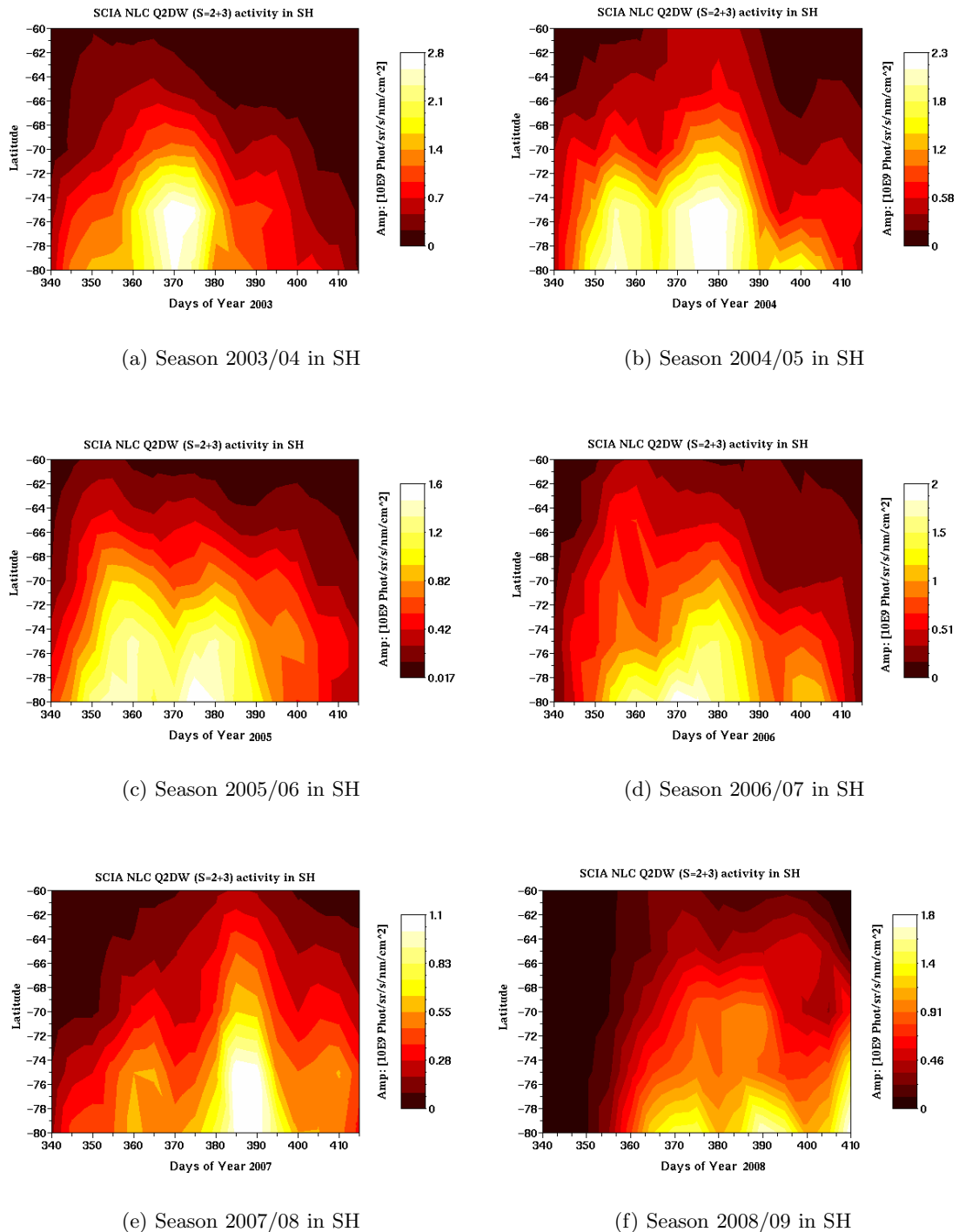


Figure 6.14: Same as Fig. 6.13 but for the summer seasons 2003/04 – 2008/09.

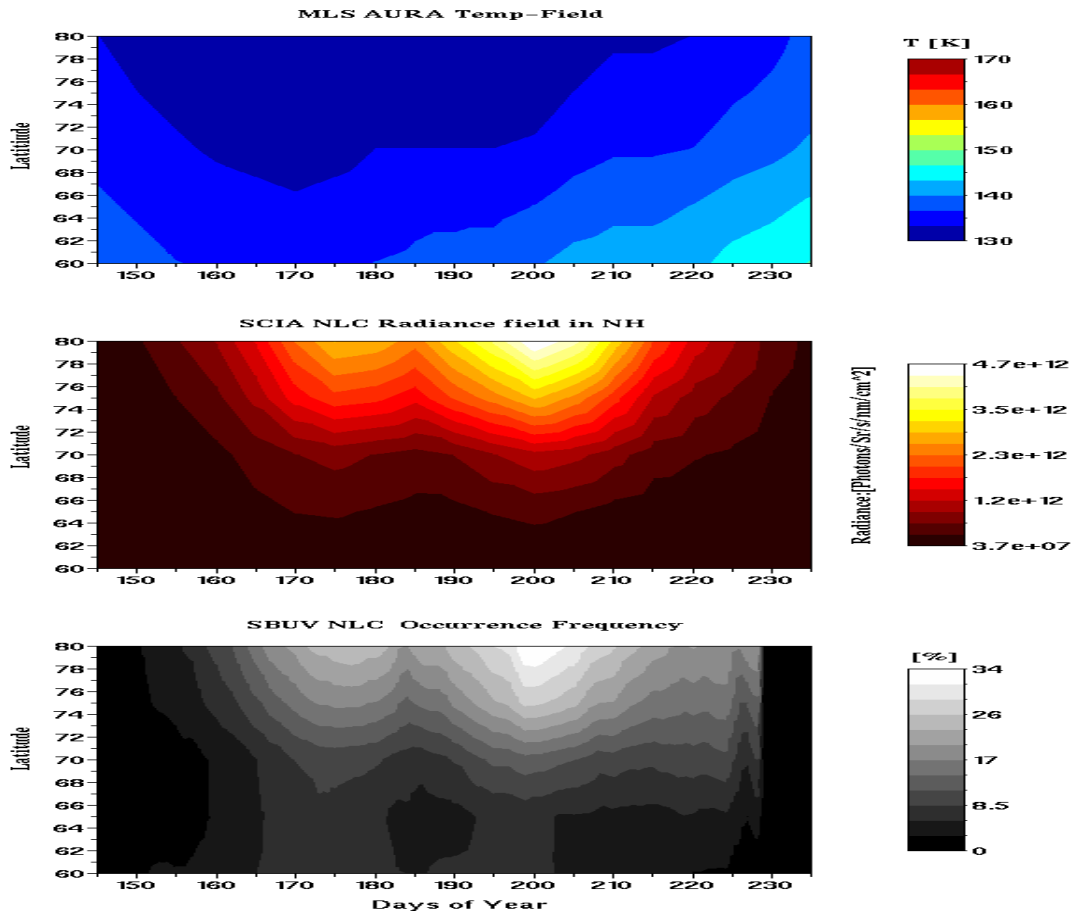


Figure 6.15: Mesopause temperature condition in the northern polar summer hemisphere for the year 2007 at the pressure level of ≈ 0.005 hPa (top panel), NLC radiance measured by SCIAMACHY (middle panel) and NLC Occurrence frequency measured by SBUV/2 NOAA – 16 (bottom panel) for the same time period and hemisphere.

with a secondary small peak around the day 400. No wave activity can be observed for the lower latitudes due to depletion of NLCs. The strongest signal is observed at higher latitudes $> 70^\circ\text{S}$. The NLC wave activity with $S = 2; 3$ appears in the same time period of temperature wave activity of $S = 2; 3$ at polar latitudes. As it has been shown earlier, the wave cell is extended for the seasons 2005/2006 and limited for the season 2004/2005, 2006/07 and 2007/2008 (Fig. 6.14). The double wave cell structure as it has been observed in the Q2DW temperature signature for the season 2008/09, can be observed in NLC radiance signals as well (Fig. 6.14 panel e). The peak amplitude of the Q2DW decreases from the season 2003/04 with 2.8 to 1.1×10^9 Photons/Sr/s/nm/cm² for the season 2007/08.

6.4 Dynamical effect of PWS on Temperature variations

NLCs can only form where the temperature drops down below the water vapor saturation temperature of about 150 K dependent on pressure. In this environment, there is a high probability that the water vapor nucleates into ice crystals, which are observed as NLCs. An example for the season 2007 in the northern hemisphere showing the temperature field from Aura MLS record and NLCs by using the SCIAMACHY and SBUV/2 data is presented in Fig. 6.15. There is a good agreement between low temperatures recorded and high NLC radiance signal or NLC occurrence frequency observed. The sudden warming starting around the day 180 of the year 2007 at high latitudes is seen as a depletion of NLCs in SCIAMACHY and SBUV/2 data.

The temperature distribution for the altitude range of 70 km to 100 km for the four southern NLC seasons is shown in Fig. 6.16. It is obvious from these temperature contour plots, that the warming at the NLC altitude of 82 – 86 km is not a result of downward shift of the mesopause, but due to the increase of temperature that seems to originate from the lower mesosphere and propagate up to the NLC heights. A temperature increase can be observed for the January 2005, 2006 and 2007 (Fig. 6.16 panels a – c) (Day 385 of the year) at NLC altitudes where the temperatures exceed the frost point temperature. For the season 2007/08 this situation occurs 10 days later (Fig. 6.16 panel d). The high temperature values in the polar mesopause region (from day 385 on) for the January 2005 (Fig. 6.16 panel a) may also be related to the strong SPE recorded and observed the NLC depletion (von Savigny et al., 2005; Rappoe et al., 2010).

6.4.1 PW activity and Temperature increase in the Polar Mesopause

In Fig. 6.17 (panels a – e) the wave amplitudes of the Q2DW and Q5DW at southern summer mid-latitudes (35°S – 45° S) are plotted together with the temperature evolution at polar latitudes (65°S – 75° S) for each individual season. Enhancements in temperature values on the order of $\delta T > 5$ K are observed during the strong PW activities. Peak amplitudes exceeding 4.4 K are highly significant at the 99.9% confidence level since the error is on the order of $\sigma \approx 0.65$ K.

For the seasons 2004/05, 2005/06 and 2006/07 (Fig. 6.17 panels a – c) the temperature increase coincides with the strong 2-day activity of up to ≈ 9 K, whereas the 5-day wave amplitude for these seasons are relatively weak and on the order of ≈ 3 K during the strong 2-day wave activity. For the seasons 2007/08 and 2008/09 (Fig. 6.17 panels d – e), the opposite is the case. Here the 5-day wave activity (amplitudes on the order of $\approx 6 - 7$ K) appears to coincide with the observed temperature increase. For the two latter seasons, the 2-day wave activity is weaker (≈ 4 K) in comparison to the seasons 2004/05 – 2006/07. These results suggest that periods with large Q2DW activity are associated with low Q5DW activity. The reasons for this behaviour are unclear.

In Fig. 6.18 a summary of all of the summer seasons in the southern hemisphere of the temperature values in the polar mesopause region and the corresponding Q2DW (Fig. 6.19 left panel) and Q5DW (Fig. 6.19 right panel) amplitudes at mid-latitude are shown. A climatological approach should be useful to depict the maximum of the wave activities at mid and polar latitudes and compare the inter-annual evolution of peak PW amplitudes with each other.

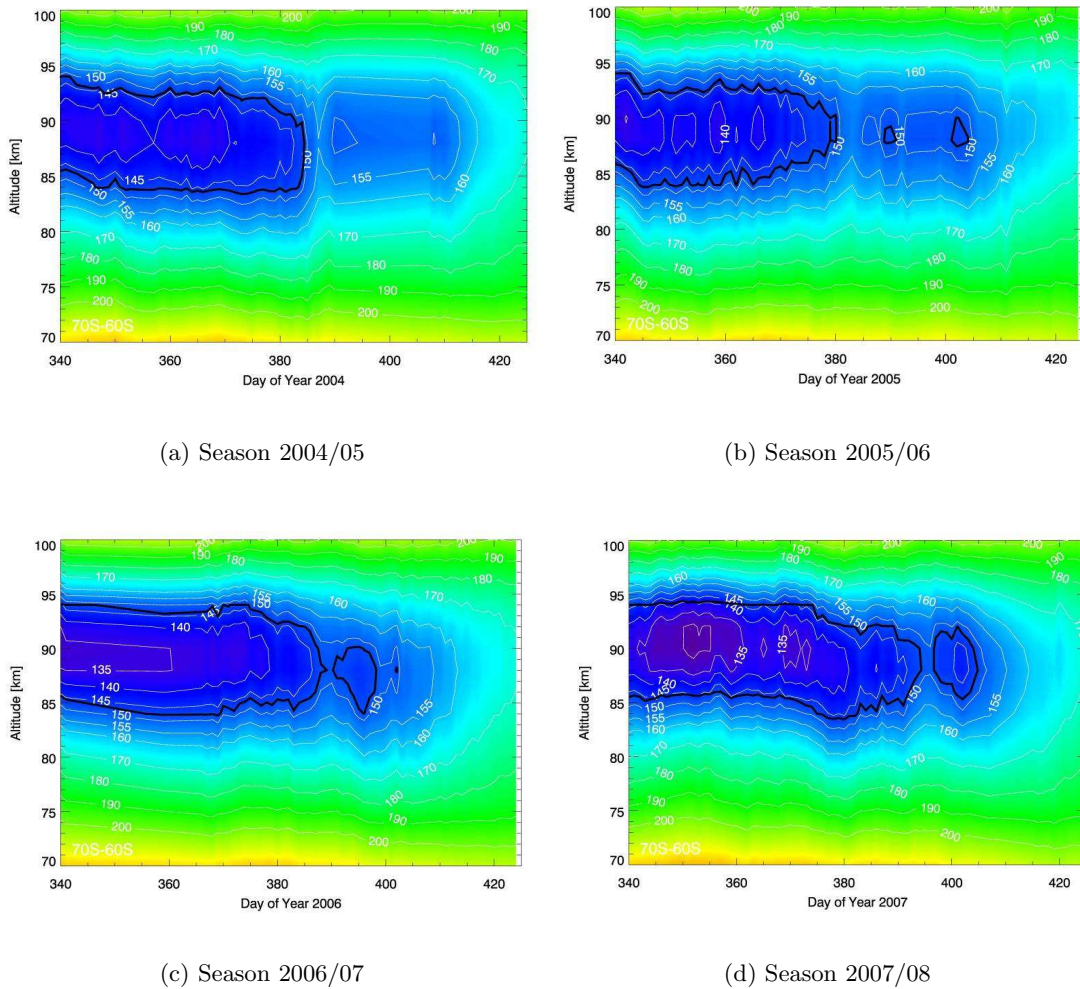
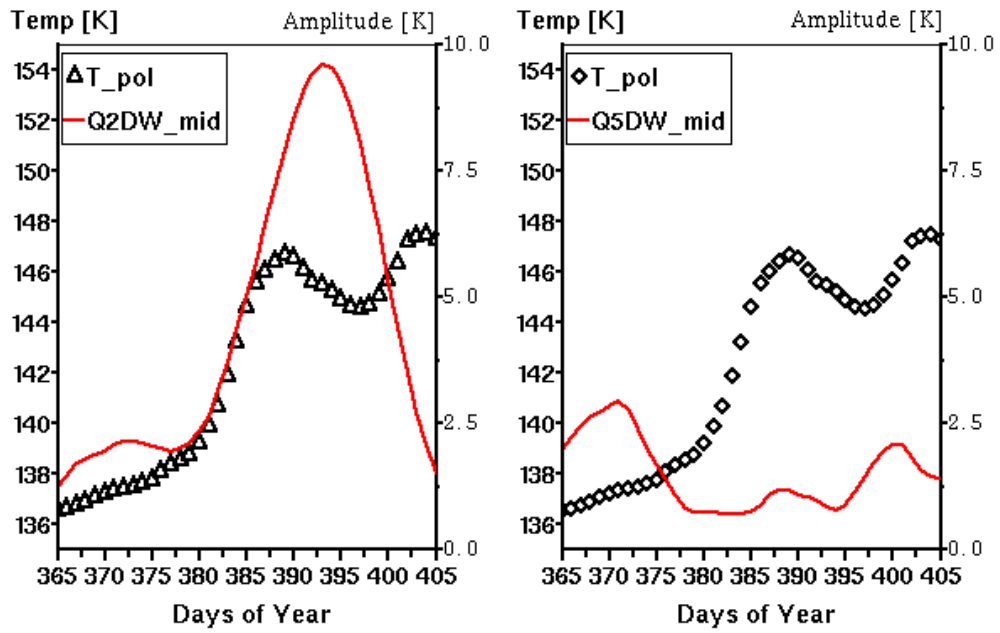
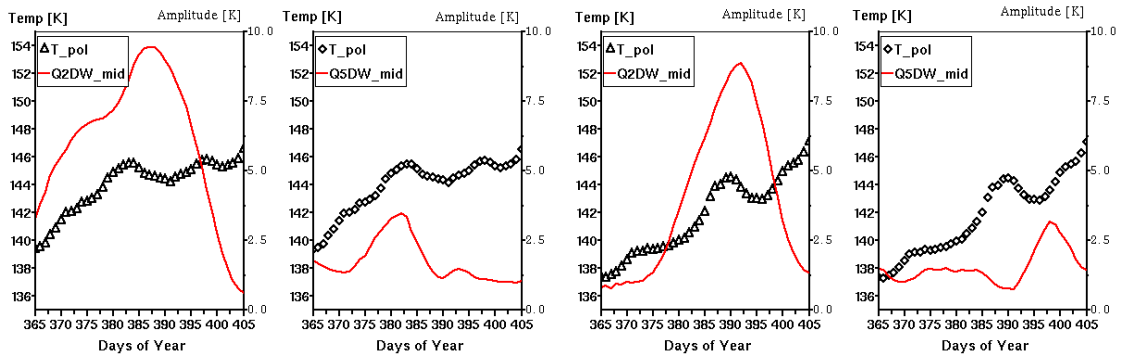


Figure 6.16: MLS temperature distribution at polar latitudes ($60^{\circ}\text{S} - 70^{\circ}\text{S}$) for altitude range 70 km – 100 km in the southern hemisphere for the seasons 2004/05 – 2007/08. Black solid line is the H_2O frost point at volume mixing ratio (VMR) 4. Taken from von Savigny et al. (2008).

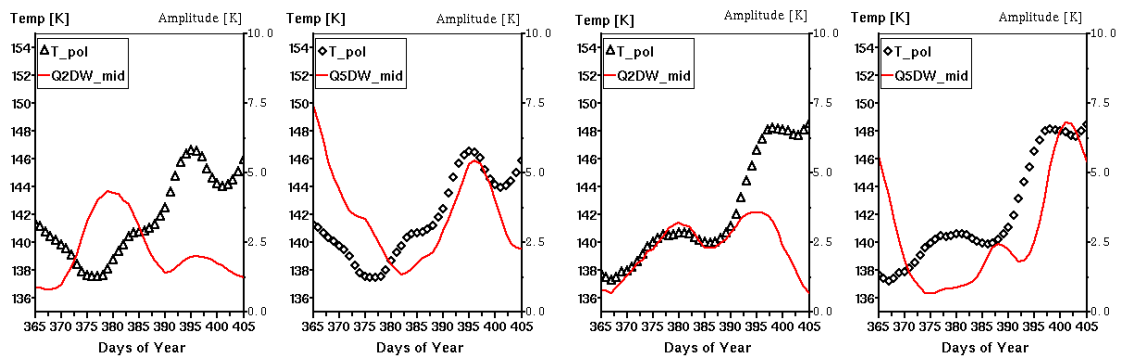


(a) Season 2004/05



(b) Season 2005/06

(c) Season 2006/07



(d) Season 2007/08

(e) Season 2008/09

Figure 6.17: Temperature evolution (left Y-axis) at polar latitudes ($65^{\circ} - 75^{\circ}$) and amplitude of the 2/5-day wave (right Y-axis) at mid-latitudes ($35^{\circ} - 45^{\circ}$) in the southern hemisphere for seasons 2004/05 – 2008/09.

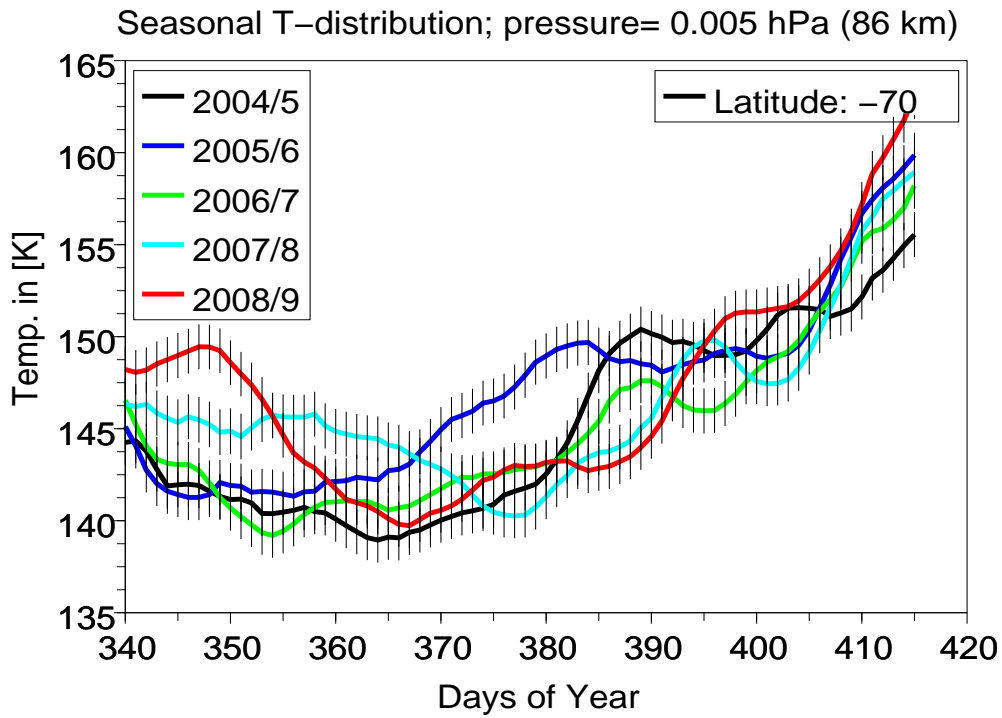
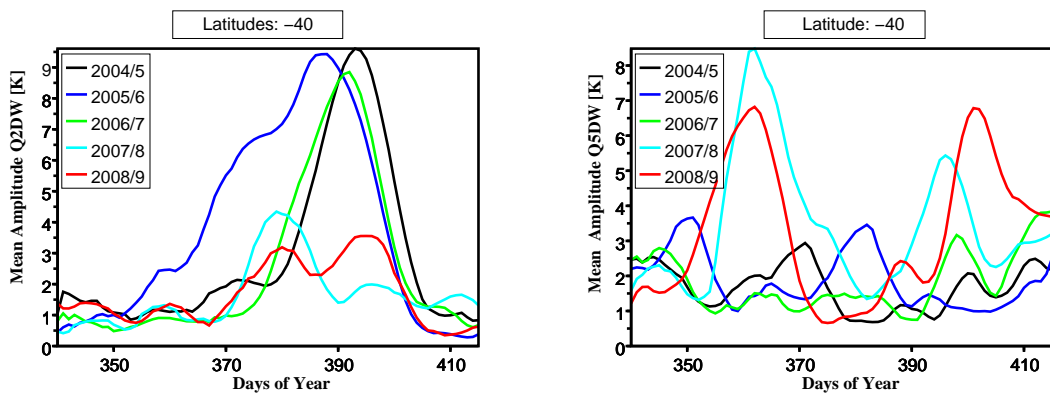


Figure 6.18: Temperature evolution in the polar summer mesopause region at $65^{\circ}\text{S} - 75^{\circ}\text{S}$.



(a) Amplitude of the Q2DW at mid-latitudes $35^{\circ}\text{S} - 40^{\circ}\text{S}$.

(b) Amplitude of the Q5DW at mid-latitudes $35^{\circ}\text{S} - 40^{\circ}\text{S}$.

Figure 6.19: Amplitudes of Q2DW and Q5DW at mid-latitudes.

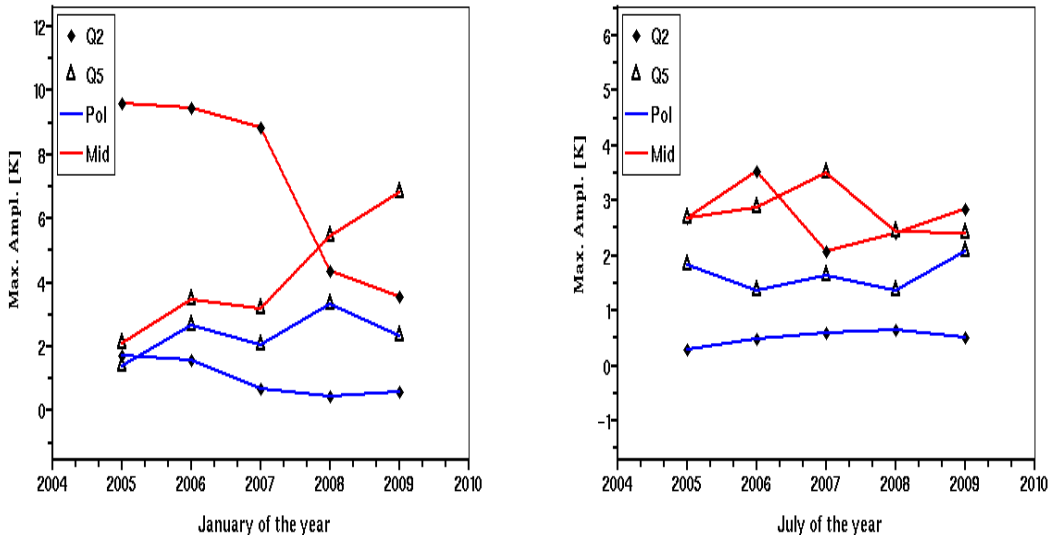


Figure 6.20: Maximum of wave amplitudes at mid and polar latitudes in the southern hemisphere at the end of January (left panel) and northern hemisphere at the end of July (right panel).

6.4.2 Climatology of the PW Activity

The temperature increase at polar latitudes seems to follow the 2/5-day wave activity at mid-latitudes as it has been shown in the last section, at least for the southern hemisphere. The maximum amplitudes of the 2-day and 5-day waves at mid and polar latitudes for the southern and northern hemisphere are shown in Fig. 6.20. There seems to be an anti-correlation between the 2-day and 5-day wave activity for the southern hemisphere at mid-latitudes (Fig. 6.20 left panel). The peak PW amplitudes are higher at mid-latitudes in comparison to polar latitudes. The peak 2-day wave amplitudes at polar latitudes follow the variation of the peak wave amplitudes at mid-latitudes. This behaviour can not be confirmed for the 5-day wave at mid and polar latitudes.

Such anti-correlation between 2-day and 5-day wave peak amplitudes can be observed in the northern hemisphere as well but with rather small variations (Fig. 6.20 right panel). The amplitudes of the waves occurring in the northern hemisphere are a factor of 2 weaker. The stable temperatures in the northern summer mesopause region may be a result of rather low PW activity at mid-latitudes. This is also observed in the higher and stable NLC occurrence rate in the northern hemisphere.

An interesting feature for both hemispheres is the fact that the 5-day wave peak amplitudes are always higher at polar latitudes compared to the 2-day wave peak amplitudes (except for the January 2005). Another speculative relationship is visible if we look at the 5-day wave peak amplitudes at polar latitudes for different years, which show a biennial oscillation pattern. Such feature is also observable in the northern hemisphere at polar latitudes but with rather smaller values.

6.5 Discussion and Conclusions

In this chapter we describe the observation of an annually recurring wave activity using MLS temperature measurements and NLC data from SBUV/2 and SCIAMACHY measurements. Wave analysis showed coincident occurrence of planetary wave activity in temperature and NLC signals for the southern hemisphere 2004/05 – 2008/09. Two dominant and prominent features of PWs, the westward propagating Q5DW and the westward/eastward propagating Q2DW are observed in mid-January in the southern hemisphere. The 2-day and 5-day waves with weaker peak amplitudes are observed in June – August in the northern hemisphere as well. The amplitudes of the southern PWs are higher compared to their northern counterpart by about a factor of 2. The possible physical mechanism for the temperature increase in the polar summer mesopause region associated with enhanced Q2DW and Q5DW activity is mainly driven due to change of the atmospheric dynamics. The main mechanism proposed so far (Holton, 1983; Andrews, 1987; Norton and Thuburn, 1996; McLandress et al., 2006) is the weakening of meridional winds due to enhanced wave activity.

As discussed by Norton and Thuburn (1996) and McLandress et al. (2006) the effect of the PWs opposes the decelerating effect on the zonal mean wind executed by breaking GWs by about 20%. GWs lead to the meridional circulation at the mesopause and the subsequent adiabatic cooling at the polar summer mesopause. Therefore, the indirect effect of PWs is to reduce adiabatic cooling of the polar summer mesopause, as it was mentioned in Chapter 2. Using temperature data one can see that wave activity at mid-latitudes occurs in the same time period as temperature increase in the polar summer mesopause. Moreover this result is consistent with the observation of a possible linear superposition of the warm phase of the 5-day and 2-day planetary waves during the 2004/05 and 2005/06 summer seasons in the southern hemisphere and increase of temperature in the mesopause region (Morris et al., 2009), which is in line with enhanced meridional flow in the 2-day planetary waves ($S = 2$ and $S = 3$) as reported by Limpasuvan and Wu (2009). As described by Rojas and Norton (2007) the 2-day wave appears each year in January – February in temperature, meridional and zonal wind data after summer solstice. The same feature is observed with weaker amplitudes in the northern hemisphere in July and August after the summer solstice.

The 2-day wave is identified as planetary normal baroclinic mode of wave number 3 ($S = 3$) (Salby and Roper, 2008). As already described by Lieberman (1999), Lieberman et al. (2002), Norton and Thuburn (1996) and McLandress et al. (2006) the 2-day wave mainly occur due to instability of the background state that generates unstable normal modes that grow in time. The annual amplification of 2-day wave is thought to be related to annual instability of the summer easterly jet (Plumb, 1983). The 2-day wave grows by extracting energy from the zonal mean flow (Salby and Callaghan, 2003).

The vertically propagating planetary waves like 2-day and 5-day waves in the summer mesosphere are excited due to baroclinic instability of the easterly flow (Norton and Thuburn, 1996). The PW forcing results in weakening of the meridional circulation and adiabatic compression of the air and warming of the mesopause region (Salby and Callaghan, 2008). The PW activity at mid-latitudes accompanied with warming or temperature increase at polar latitudes at the end of the southern summer season in the mesopause region is observed and showed in this work using the MLS temperature data. After the summer solstice the NLC reduction is mainly driven by the temperature increase, and the variability of the NLCs at the end of the summer season is in part a result of the planetary wave activity. The planetary wave signatures can be observed as well by using

the NLC data of SCIAMACHY and SBUV/2. The westward propagating 2-day and 5-day waves and eastward propagating 2-day wave in NLC signals are observed. The dissipation or energy flux interaction of the Q2DW which is related to the non-linear interaction can lead to superposition of $S = (+2; +3)$ with diurnal tide which explains the occurrence of $S = (-1; -2)$ Q2DW (Palo et al., 2007). A westward and eastward propagating Q2DW with $S = |2 + 3|$ have been found by Morris et al. (2009) by using the groundbase PMSE (Davis, Antarctica) and MLS wind data and by Merkel et al. (2008) who used the NLC data from SNOE satellite, which confirms our results.

We suggest that the planetary wave activity explains the variation and reduction in NLC observed in the southern hemisphere due to warming of the polar mesopause region. However, von Savigny et al. (2007a) proposed a similar indirect adiabatic warming of the mesopause region due to January 2005 SPE in the southern hemisphere. The rather strong depletion of NLCs and strong temperature increase in the mid of January 2005 could be a result of combined effects of 2-day wave activity and strong SPE observed in the same period (von Savigny et al., 2007a; Rahpoe et al., 2010). Since the southern summer mesopause is warmer compared to the northern summer mesopause, this explains the rather greater effect of temperature deviations on NLCs in the southern hemisphere due to planetary wave activity.

We conclude that the PW (mainly Q2DW and Q5DW) activity at mid-latitudes influence the polar latitude mesopause region temperatures due to dynamical effects, which are observed as temperature increases at polar latitudes, and manifest themselves in NLC occurrence rate reduction and PW wave features in NLC radiance and residual albedo signals.

Chapter 7

Concluding Remarks

This thesis consists of two main parts. In the first part we were investigating the relationship between the occurrence of solar proton events (SPEs) and the depletion of noctilucent clouds (NLCs). The second part of the work is related to the planetary wave activity during the NLC season at mid-latitudes and its relationship to the temperature and the NLC variation observed in the polar summer mesopause region.

We presented a possible connection between the SPEs and NLCs. The correlation of the two independent time series have been determined using the derivatives of proton flux and the derivatives of the NLC residual albedo and occurrence rate time series. The derivative method improved significantly the estimation of the derived time lags. The number of significant SPE cases, which lead to reduction of NLCs is dependent on the proton flux energy channel. Such a dependency is not observed for the two strong cases, e.g. for July 2000 SPE in the northern hemisphere and January 2005 SPE in the southern hemisphere. The enhancement of proton flux during the SPE is anti-correlated to NLC occurrence rate time series in the northern hemisphere with $R = -0.62 \pm 0.08$ with a timelag of $T = 4.73 \pm 4.11$ days. For the NLC albedo time series a shorter time lag on the order of $T = 3.04 \pm 2.44$ days is observed. The time lag for all SPE cases is found in the southern hemisphere with $T = 5.84 \pm 3.65$ days and $T = 4.99 \pm 1.42$ days for the NLC occurrence rate and albedo residuals respectively. Merging of data sets and the discretized definition of occurrence rate signature leads to the relatively large errors in the estimation of time lags from the NLC occurrence rate time series. Nevertheless the derived time lags are within the time frame of dynamical forcing which can last for several days during and after the SPE. Our result shows clearly, that SPEs are a part of the external forcing, and contribute significantly to the perturbation in the dynamics of the Earth's atmosphere.

In the second part of the thesis the dynamical effects in the mesopause region have been studied. The planetary wave activity of the prominent candidates, the westward propagating 2-day and 5-day waves have been observed using three independent data sets, i.e., MLS temperature, SCIAMACHY NLC radiance and SBUV residual albedo time series. In all of these data sets the 2-day and 5-day waves were present with enhanced amplitudes after the summer solstice. The hemispherical difference in peak signal of the 2-day wave has been confirmed with higher peak amplitudes of PWs in the southern hemisphere. Moreover, the peak amplitudes of the 2-day wave and 5-day wave at mid-latitudes and their occurrence have been compared with the temperature increase at polar latitudes during the same time period. The strong tendency of wave activity at mid-

latitudes leading to a temperature increase at polar latitudes on the order of $\approx 5 - 6$ K in the southern mesopause region has been demonstrated. This polar summer mesopause warming is expected from model simulations, because the PWs oppose the decelerating effect of the GW-drag on the zonal mean flow and lead to a reduced meridional circulation, and in consequence to reduced adiabatic cooling of the polar summer mesopause. Beside the fact that the temperature increase at polar latitudes is well correlated with the 2-day wave activity at mid-latitudes, it has been shown, that the 5-day wave activity can influence the temperature increase at the southern polar latitudes as well. Temperature increase on the order of ≈ 8 K at polar latitudes and 0.005 hPa pressure level corresponding to an altitude of ≈ 86 km has been found for the January 2005. One can assume that this warming is a combination of SPE forcing due to solar proton precipitation in the mid-January and relatively strong 2-day wave activity for the same time period at mid and polar latitudes.

Outlook

The next step in the investigation of NLCs and SPEs would be to use different satellite data like AIM/CIPS, SCIAMACHY and SBUV/2 which observe independently the noctilucent clouds together with ground based measurements. A comparison of different data sets will allow more reliable results on the expected effects of an SPE during the active phase of the Sun. The NLCs then can be used as an additional dynamical and extra terrestrial proxy in the polar summer mesopause region. In this way an extended climatological link can be established between the past and future SPEs and NLCs.

Better time resolution is required for the upper mesosphere in order to be able to investigate in more detail which reacts very sensitively toward temperature perturbations and affect NLCs. Independent temperature data sets with better coverage of the polar region would be useful to detect dynamical forcings such as planetary wave and gravity wave effects in this part of our Earth's atmosphere. Numerical models such as KMCM (Kühlungsborn Mechanistic general Circulation Model) are suited for investigating the relationship between planetary wave activity and the temperature increase in the polar summer mesopause region and may allow a more detailed physical interpretation of the dynamical processes behind these impacts. The KMCM model will be used in the near future to further improve the understanding of the relationship between mid-latitude planetary wave activity in the summer hemisphere and the temperature changes at the polar summer mesopause.

List of Figures

1.1	A sketch drawing of the inner structure of the Sun.	4
1.2	Magnetic field line evolution as a function of time.	6
1.3	Scenario for the formation of an arch-filament system.	6
1.4	Three possible configurations for ICMEs.	7
1.5	Idealized, cartoon sketches of interplanetary coronal mass ejections (ICMEs).	8
1.6	Plots of different parameters recorded by SEM onboard GOES – 10 the month July 2000.	9
1.7	A sketch of the possible chemical reactions during solar proton event for the N_2	10
1.8	Same as Fig. 1.7 but for the production of HO_x during the solar proton event.	11
2.1	Vertical thermal structure of Earth’s atmosphere up to 120 km.	13
2.2	Positions of jet streams in the meridional circulation.	15
2.3	Difference between pure radiative equilibrium (A and C) for the Earth’s atmosphere and real observed temperature (B+D) distribution.	16
2.4	Geostrophic wind flow parallel to straight isobars, which is maintaining the balance between horizontal pressure gradient force (PGF) and the Coriolis Force (CF).	16
2.5	Schematic streamlines of the solstice diabatic circulation in them middle atmosphere.	17
2.6	Representative trajectories (model) for the stratosphere and mesosphere.	18
2.7	Propagation characteristics of Rossby waves in the southern hemisphere.	20
2.8	An example of 2-day wave with wavenumber 3 showing the potential vorticity on a stereographic projection for the northern hemisphere.	21
2.9	Condition for the vertical propagation of gravity waves.	22
2.10	Illustrating the behaviour of a gravity wave as it propagates upward into the mesosphere.	22
3.1	NOAA-9 SBUV/2 252 nm albedo values for all measurements northward of $50^\circ N$ on 1985 day 180.	26
3.2	Time history of equator-crossing times for SBUV and SBUV/2 instruments.	28
4.1	Averaged occurrence rate of all NLC seasons (blue cross) from SBUV/2 data for the satellites NIMBUS 07 – NOAA 18.	34
4.2	Contour plot of NLC occurrence rate as a function of longitude and time for the season 2000 in the northern hemisphere and for the latitude band $60^\circ - 70^\circ$	35

4.3	An example of zonal mean NLC occurrence rate for the season 2004/05 in the southern hemisphere and three different latitude bands.	36
4.4	A contour plot of the SCIAMACHY NLC radiance field and SBUV/2 NLC residual albedos during the NLC season.	37
4.5	Mean altitude (daily zonal mean) of NLC with backscatter coefficients.	37
4.6	Particle radius vs. day from solstice for the northern hemisphere of the year 2000.	38
4.7	Distribution of NLC altitudes for each hemisphere.	39
4.8	The seasonal distribution of NLC altitude for all NLCs observed by HALOE from 1991 to 2005 and latitudes between 55° and 70°.	39
4.9	Hourly centroid altitudes z_c (upper panel, circles) and hourly maximum backscatter ratios R_{max} (middle panel, triangles) of NLCs observed during June/July 1997.	40
4.10	Mean seasonal variation of the NLC particle size retrieved using different PSD assumptions.	42
4.11	The variation in number of nights with noctilucent clouds from the year 1949 to year 1980.	43
4.12	The solid curve shows the number of nights during which noctilucent clouds were sighted versus year.	45
5.1	Zonally and daily averaged NLC occurrence rate time series and SPE time series.	48
5.2	Penetration and ionization altitude range of energetic proton particles depending on the kinetic energy in MeV.	49
5.3	Sample normalized dALB and dSPE time series for a window of width 25 days and for the July 2000 SPE.	51
5.4	Sample cross-correlations of proton flux and albedo time series (derivatives dSPE & dALB) as a function of time lag for the July 2000 SPE.	52
5.5	Same as 5.4 but for the January 2005 in the southern hemisphere.	53
5.6	Dependence of the obtained time lag of the negative correlation extremum on window widths (here 15 – 30 days) for the January 2005 SPE and no derivation of the time series.	54
5.7	Example of resampled dALB and dSPE time series for a window of width 25 days.	55
5.8	Comparison of negative r_c and r_{crit} for different widths of the scanning window for the January 2005.	56
5.9	Same as Fig. 5.6 except for the derivative of the NLC albedo time series and for a window width range from 15 to 30 days.	57
5.10	Scatter plot of \bar{r}_c (correlation coefficient) and \bar{t}_c (time lag) for all the SPEs during the NLC core season (days 0 to 40 with respect to solstice) and energy channel 2.	62
5.11	Same as figure 5.10 but for energy channel 3.	62
5.12	Scatter plot of \bar{r}_c (correlation coefficient) and proton flux $Ev_{prot.}$	63
5.13	Same as figure 5.12 but for proton energy channel 3.	63
6.1	Zonal mean gravity wave drag and EP flux divergence.	66
6.2	Hovmöller plot of temperature signatures around day 387 of the season 2004/05 in the southern hemisphere.	66
6.3	Hovmöller plot of fitted model parameters.	67

6.4	Appearance of temperature wave signatures in MLS Aura data.	68
6.5	Wavenumber frequency plot of MLS Aura temperature data.	69
6.6	Wavenumber frequency plot of NLC radiance using SCIAMACHY data. . .	70
6.7	Same as Fig. 6.6 but for different days.	71
6.8	Wavenumber frequency plot of NLC residual albedo using SBUV/2 NOAA – 16 data.	72
6.9	Same as Fig. 6.8 but for different days.	73
6.10	Latitudinal extent of the Q2DW for the days 340 – 415 of the season 2004/05.	74
6.11	Same as Fig. 6.10 but for different seasons in the southern hemisphere. . .	75
6.12	Same as Fig.6.11 but for the northern hemisphere.	76
6.13	Latitudinal extent of the Q2DW for the days 340 – 415 of the season 2004/05 in NLC radiance data from SCIAMACHY.	77
6.14	Same as Fig. 6.13 but for the summer seasons 2003/04 – 2008/09.	78
6.15	Mesopause temperature condition, NLC radiance and NLC occurrence rate in the northern polar summer hemisphere for the year 2007.	79
6.16	MLS temperature distribution at polar latitudes (60°S – 70°S) for altitude range 70 km – 100 km in the southern hemisphere for the seasons 2004/05 – 2007/08.	81
6.17	Temperature evolution at polar and mid-latitudes.	82
6.18	Temperature evolution in the polar summer mesopause region at 65°S – 75°S.	83
6.19	Amplitudes of Q2DW and Q5DW at mid-latitudes.	83
6.20	Maximum of wave amplitudes at mid and polar latitudes in the southern and northern hemisphere.	84

List of Tables

3.1	SBUV/2 Instrument Observations based on DeLand et al. (2007).	25
3.2	Standard SBUV/2 Wavelengths.	25
3.3	Energy ranges for the Energetic Particles Sensor (EPS).	30
3.4	Summary of MLS Temperature product.	31
3.5	SCIAMACHY spectral coverage and resolution for channels 1-8.	31
5.1	Correlation results of NLC albedo time series and proton fluxes for different proton energies and for the July 2000 SPE.	58
5.2	Same as Table 5.1 but for the January 2005 SPE.	59
5.3	Analysis results for the SPEs that occurred during the northern hemisphere NLC seasons for proton energy channel 2 (5 – 10 MeV).	60
5.4	Same as Table 5.3 but for the SPEs that occurred during the southern hemisphere NLC seasons.	60
5.5	Results of the NLC data analysis.	61
5.6	The correlation coefficients R_c and time lags T_c are averages for all cases with statistically significant negative correlation coefficients.	61

Bibliography

- Alpers, M., Gerding, M., Höffner, J., von Zahn, U., 2000. NLC particle properties from a five-color lidar observation at 54°N. *J. Geophys. Res.*, 105(D10), 12, 235 – 240.
- Andrews, D. G., 1987. The influence of atmospheric waves on the general circulation of the middle atmosphere. *Phil. Trans. R. Soc., A* 323, 693 – 705.
- Andrews, D. G., Holton, J. R., Leovy, C. B., 1987a. Middle Atmosphere Dynamics. *Academic Press, New York*.
- Azeem, S. M. I., Palo, S., E., Wu, D. L., Froidevaux, L., 2001. Observations of the 2-Day Wave in UARS MLS Temperature and Ozone Measurements. *Geophys. Res. Lett.*, Vol. 28, No. 16, 3147 – 3150.
- Backhouse, T. W., 1885. The luminous cirrus cloud of June and July. *Meteo. Mag.*, 20:133.
- Bailey, S. M., Merkel, A. W., Thomas, G. E., Carstens, J. N., 2005. Observations of polar mesospheric clouds by the Student Nitric Oxide Explorer. *J. Geophys. Res.* 110, D13203, doi:10.1029/2004JD005422.
- Baumgaertner, A. J. G., McDonald, A. J., Hibbins, R. E., Fritts, D. C., Murphy, D. J., Vincent, R. A., 2008. Short-Period Waves in the Antarctic Middle Atmosphere. *J. Atmos. Sol.-Terr. Phys.*, doi:10.1016/j.jastp.2008.04.007.
- Baumgarten, G., Fiedler, J., 2008. Vertical structure of particle properties and water content in noctilucent clouds. *Geophys. Res. Lett.*, 35(L10811).
- Beer, T., 1974. Atmospheric Waves. *Adam Hilger Ltd., Bristol, England*.
- Becker, E., and Fritts, D., 2006. Enhanced gravity-wave activity and interhemispheric coupling during the MaCWAVE/MIDAS northern summer program 2002. *Ann. Geophys.*, 24(4), 1175.
- Becker, E., von Savigny, C., 2010. Dynamical heating of the polar summer mesopause induced by solar proton events. *J. Geophys. Res.* 115, D00I18, doi:10.1029/2009JD012561.
- Berger, U., and von Zahn, U., 2002. Icy particles in the summer mesopause region: Three-dimensional modeling of their environment and two-dimensional modeling of their transport. *J. Geophys. Res.*, 107(A11), 1366, doi: 10.1029/2001JA000316.
- Bhartia, P. K., McPeters R. D., Mateer, C. L., Flynn, L. E., and Wellemeyer, C., 1996. Algorithm for the estimation of vertical ozone profile from the backscattered ultraviolet technique. *J. Geophys. Res.*, 101, 18, 793-806.

- Bovensmann, H., Burrows, J. P., Buchwitz, M., Frerick, J., Noël, S., Rozanov, V. V., Chance, K. V., and Goede, A. P. H., 1999. SCIAMACHY: Mission Objectives and Measurement Modes. *J. Atmos. Sci.*, 56(2), 127 – 150.
- Brandon, J.: Recreational Aviation Australia, Lecture Notes on Aviation Meteorology, Met Images (<http://www.auf.asn.au/metimages/rossby1.gif>).
- Brasseur, G., and Solomon, S., 1984. Aeronomy of the Middle Atmosphere. *D. Riedel Publishing Company, Dordrecht*.
- Burlaga, L. F., Lepping, R. P., and Jones, J. A., 1990. Global Configuration of a Magnetic Cloud, Physics of Magnetic Flux Ropes. *Geophys. Monogr., AGU*, 58, pp. 373 – 377.
- Burks, D., and Leovy, C., 1986. Planetary waves near the mesospheric easterly jet. *Geophys. Res. Lett.*, 13, 193 – 196.
- Cahen, S., Doom, C., and Casse, M., 1986. '86 Massive Neutrinos in Astrophysics and Particle Physics. *Editions Frontieres*, p. 83.
- Carbary, J. F., Morrison, D., Romick, G.J., 2002. Particle characteristics from the spectra of polar mesospheric clouds. *J. Geophys. Res.*, 107(D23), 4686, doi:10.1029/2001JD001115.
- Charney, J. G., and Drazin, P. G., 1961. Propagation of planetary-scale disturbances from the lower into the upper atmosphere. *J. Geophys. Res.*, 66, 83.
- Chesters, D., 1996. GOES I/M Databook.
Weblink: www.rsd.gsfc.nasa.gov/goes/text/goes.databook.html
- Chu, X., and Gardner, C. S., 2003. Lidar studies of interannual, seasonal, and diurnal variations of polar mesospheric clouds at the South Pole. *J. Geophys. Res.*, 108(D8).
- Clark, R. R., 1989. The quasi-2-day wave at Durham (43N); solar and magnetic effects. *J. Atmos. Sol.-Terr. Phys.*, 51, 617 – 622.
- Craig, R. L., Elford, W. G., 1981. Observations of the Quasi 2-Day Wave near 90 km Altitude at Adelaide (35S). *J. Atmos. Terr. Phys.*, 43 (10), 1051 – 1056.
- Craig, R. L., Vincent, R. A., and Plumb, R. L., 1985. On the interaction between the quasi-2-day wave and the mean flow. *Handb. MAP*, 18, 76 – 79.
- Crutzen, J., Isaksen, I. S. A., Reid, G. C., 1975. Solar Proton Events: Stratospheric Sources of Nitric Oxide. *Science*, Vol. 189, No. 4201, pp. 457 – 459.
- DeLand, M. T., Shettle, E. P., Thomas, G. E., Olivero, J. J., 2003. Solar backscatter ultraviolet (SBUV) observations of polar mesospheric clouds (PMCs) over two solar cycles. *J. Geophys. Res.*, 108(D8), 8445.
- DeLand, M.T., Shettle, E.P., Thomas, G. E., Olivero, J. J., 2006a. Latitude-dependent long-term variations in polar mesospheric clouds from SBUV version 3 PMC data. *J. Geophys. Res.* 112, D10315, doi:10.1029/2006JD007857.
- Dryer, M., 1994. Interplanetary studies: Propagation of disturbances between the sun and the magnetosphere. *Space Sci. Rev.*, 67, 363 – 419.

- Dryer, M., Wu, S. T., Gislason, G., Han, S. M., Smith, Z. K., Wang, J. F., Smart, D. F., and Shea, M. A., 1984. Magnetohydrodynamic Modeling of Interplanetary Disturbances between the Sun and Earth. *Astrophys. Space Sci.*, 105, 187.
- Dunkerton, T., 1979. On the Mean Meridional Mass Motions of the Stratosphere and Mesosphere. *Americ. Meteo. Soc.*, 22, 2325 – 2333.
- Ebisuzaki, W., 1997. A method to estimate the statistical significance of a correlation when the data are serially correlated. *J. of Climate* 10(9), 2147-2153.
- Eliassen, A., and Palm, E., 1960. On the transfer of energy in stationary mountain waves. *Geophys. Norv.*, 22, 1.
- Flynn, L. E., Kondragunta, S., Horvath, K., and Beach, H., 2000. Internal validation of SBUV/2 ozone vertical profile data sets, paper presented at Quadrennial Ozone Symposium. *Int. Ozone Comm., Sappora, Jpn.*, 3-8 July 2000.
- Fogle, B., and B. Haurwitz, 1966. Noctilucent clouds. *Space Sci. Rev.*, 6, 279 – 340.
- Frederick, J. E., Cebula, R. P., and Heath, D. F., 1986. Instrument characterization for the detection of long-term changes in stratospheric ozone: An analysis of the SBUV/2 radiometer. *J. Atmos. Oceanic Technol.*, 3, 472 – 480.
- Frederick, J. E., 2008. Principles of Atmospheric Science. *Jones and Bartlett Publishers, Inc., The University of Chicago.*
- Fritts, D. C., 1984. Gravity Wave Saturation in the Middle Atmosphere: A Review of Theory and Observations. *Rev. Geophys. and Space Phys.*, 22, 3, 275 – 308.
- Froidevaux, L., et al., 2006. Early validation analyses of atmospheric profiles from EOS MLS on the Aura satellite. *IEEE Transactions on Geoscience and Remote Sensing*, 44(5), 1106 – 1121.
- Gadsden, M., 1982. Noctilucent Clouds. *Space Sci. Rev.*, 33, 279 – 334.
- Gadsden, M., 1998. The North-West Europe data on noctilucent clouds: a survey. *J. of Atmos. Terr. Phys.*, 60, 1163 – 1174.
- Garcia, R., 1989. Dynamics, Radiation, and Photochemistry in the Mesosphere: Implications for the Formation of Noctilucent Clouds. *J. Geophys. Res.*, 94(D12), 605 – 615.
- Glass, M., Fellous, J. L., Massbeuf, M., Spizzichino, A., Lysenko, I. A., and Portnyagin, Yu., I., 1975. Comparison and interpretation of the results of simultaneous wind measurements in the lower thermosphere at Garchy (France) and Obninsk (USSR) by meteor radar technique. *J. Atmos. Sol. Terr. Phys.*, 37, 1077 – 1087.
- Gumbel, J., and Witt, G., 1998. In Situ Measurements of the Vertical Structure of a Noctilucent Cloud. *Geophys. Res. Lett.* 28(7), 1053 – 1058.
- Gurubaran, S., Sridharan, S., Ramkumar, T. K., Rajaram, R., 2001. The mesospheric quasi-2-day wave over Tirunelveli (8.7N). *J. Atmos. Sol.-Terr. Phys.*, 63, 975 – 985.

- Hagan, M. E., Forbes, J. M., and Vial, F., 1993. Numerical investigation of the propagation of the quasi-two-day wave into the lower thermosphere. *J. Geophys. Res.*, *98*, 23, 193 – 205.
- Harris, T. J., 1994. A long-term study of the quasi-two-day wave into the lower thermosphere. *J. Atmos. Sol. Terr. Phys.*, *56*, 569 – 579.
- Harrison, R. A, and Sime, D. G., 1989. Comments on Coronal Mass Ejection onset Studies. *Astron. Astrophys.*, *208*, 274.
- Harrison, R. A., 1991. Coronal transients and their relation to solar flare. *Adv. Space Res.*, *11*(1), 25.
- Heath, D. F., C. L. Mateer and A. J. Krueger, 1973. The Nimbus 4 backscatter ultraviolet atmospheric ozone experiment. Two year's operation. *Pure Appl. Geophys.*, 106 – 108, 1238 – 1253.
- Hervig, M., Siskind, D., 2005. Decadal and inter-hemispheric variability in polar mesospheric clouds, water vapor, and temperature. *J. Atmos. Sol.-Terr. Phys.*, doi:10.1016/j.jastp.2005.08.010.
- Holton, J. R., 1983: The influence of gravity wave breaking on the general circulation of the middle atmosphere. *J. Atmos. Sci.*, *40*, 2497 – 2507.
- Holton, J. R., 2004. An Introduction to Dynamic Meteorology, fourth edition. *Elsevier Academic, Burlington*.
- Houghton, J., 2002. The Physics of Atmospheres. *Cambridge University Press, Cambridge, UK*.
- Hunt, B. G., 1981. The 2-day wave in the middle atmosphere as simulated in a general circulation model extending from the surface to 100 km. *J. Atmos. Sol.-Terr. Phys.*, *43*, 1143 – 1154.
- Jackman, C. H., and McPeters, R. D., 1985. The response of ozone to solar proton events during solar cycle 21: A theoretical interpretation. *J. Geophys. Res.*, *90*, 7955 – 7966.
- Jackman, C. H., McPeters, R. D., Labow, G. J., Fleming, E. L., Praderas, C. J., and Russell, J. M., 2001. Northern hemisphere atmospheric effects due to the July 2000 solar proton events. *Geophys. Res. Lett.* *28*, 2883 – 2886.
- Jackman, C. H., McPeters, R. D., 2004. The effect of solar proton events on ozone and other constituents. In: Solar variability and its effects on climate. *Geophys. Monogr.* *141*, AGU.
- Jackman, C. H., Roble, R. G., Fleming, E. L., 2007. Mesospheric dynamical changes induced by the solar proton events in October-November 2003. *Geophys. Res. Lett.* *34*, L04812.
- Jensen, E., Thomas, G. E., Toon, O. B., 1989. On the diurnal variation of noctilucent clouds. *J. Geophys. Res.*, *94*, 14,693-14,702.
- Jesse, O., 1885. Auffallende Abenderscheinungen am Himmel. *Meteo. Z.*, *2*, 179 – 181.

- Kahler, S. W., Moore, R. L., Kane, S. R., and Zirin, H., 1988. Filament Eruptions and the Impulsive Phase of Solar Flares. *Astrophys. J.*, 328, 824.
- Kahler, S. W., and Reames, D. V., 1991. Probing the Magnetic Topologies of Magnetic Clouds by Means of Solar Energetic Particles. *J. Geophys. Res.*, 96, 9419.
- Karlsson, B., and Rapp, M., 2006. Latitudinal dependence of noctilucent cloud growth. *Geophys. Res. Lett.*, 33(L11812).
- Klenk, K. F., Bhartia, P. K., Fleig, A. J., Kaveeshwar, V. G., McPeters, R. D., Smith, P. M., 1980. Total ozone determination from the Backscattered Ultraviolet (BUV) experiment. *J. Appl. Meteorol.*, 21, 1672-1684.
- Krivolutsky, A.A., Klyuchnikova, A.V., Zakharov, G.R., Vyushkova, T. Yu., Kuminov, A.A., 2006. Dynamical response of the middle atmosphere to solar proton event of July 2000: Three-dimensional model simulation. *Adv. Space Res.*, 37, 1602 – 1613.
- Lean, J., 1987. Solar ultraviolet irradiance variations, A review. *J. Geophys. Res.*, 92, 839 – 868.
- Leslie, R., 1885. Sky glows. *Nature (London)*, 32, 245.
- Lieberman, R. S., 1999. Eliassen-Palm fluxes of the 2-day wave. *J. Atmos. Sci.*, 56, 2846 – 2861.
- Lieberman, R. S., Riggin, D. M., Franke, S. J., Hanson, A. H., Meek, C., Nakamura, T., Tsuda, T., Vincent R. A., and Reid, I., 2003. The 6.5-day wave in the mesosphere and lower thermosphere: Evidence of baroclinic/barotropic instability. *J. Geophys. Res.*, 108, No. D20, 4640, doi:10.1029/2002JD003349.
- Limpasuvan, V., Wu, D. L., Schwartz, M. J., Waters, J. W., Wu, Q., Killeen, T. L., 2005. The two-day wave in EOS MLS temperature and wind measurements. *Geophys. Res. Lett.*, 32, L17809, doi:10.1029/2005GL023396.
- Limpasuvan, V., and Wu, D. L., 2009. Anomalous two-day wave behavior during the 2006 austral summer. *Geophys. Res. Lett.*, 36, L04807, doi:10.1029/2008GL036387.
- Livesey, N. J., et al., 2007. *Version 2.2 Level 2 data quality and description document*.
- Low, B. C., 1993. Mass Acceleration Process: the Case of the Coronal Mass Ejection. *COSPAR Proceedings, Washington, D. C., September 1992, Pergamon Press, London*.
- Lübken, F.-J., 2000. Nearly zero temperature trend in the polar summer mesosphere. *Geophys. Res. Lett.*, 27, 3603 – 3606.
- Lübken, F.-J., and Berger, U., 2007. Interhemispheric comparison of mesospheric ice layers from the LIMA model. *J. Atmos. Terr. Phys.*, 69(17-18), 2292 – 2308.
- Lumpe, J. D., Alfred, J. M., Shettle, E. P., and Bevilacqua, M., 2008. Ten Years of Southern Hemisphere Polar Mesospheric Cloud Observations from the POAM Instruments. *J. Geophys. Res.*, 113(D04205).
- McComas, D. J., and Gosling, J. T., 1988. Magnetic Field Draping about Coronal Mass Ejecta. *Proc. of the Sixth International Solar Wind Conference, NCAR Technical Note – 306, Vol. I, pp. 291 –296*.

- McLandress, C., Ward, W. E., Fomichev, V. I., Semeniuk, K., Beagley, S. R., McFarlane, N. A., and Shepherd, T. G., 2006. Large-scale dynamics of the mesosphere and lower thermosphere: An analysis using the extended Canadian Middle Atmosphere Model. *J. Geophys. Res.*, *111*, D17111, doi:10.1029/2005JD006776.
- McPeters, R. D., Jackman, C. H., and Stassinopoulos, E. G., 1981. Observations of ozone depletion associated with solar proton events. *J. Geophys. Res.*, *86*, 12071 – 12081.
- Meek, C. E., 1996. Global study of northern hemisphere quasi-2-day wave events in recent summers near 90 km altitude. *J. Atmos. Sol.-Terr. Phys.*, *58*, 1401 – 1411.
- Megner, L., Gumbel, J., Rapp, M., and Siskind, D., 2009. Reduced meteoric smoke particle density at the summer pole – Implications for mesospheric ice particle nucleation. *Adv. Space Res.*, *41*, 41 – 49.
- Megner, L., and Gumbel, J., 2009. Charged meteoric particles as ice nuclei in the mesosphere: Part 2 A feasibility study. *Adv. Space Res.*, *31*(9), 2033 – 2043.
- Merkel, A. W., Barth, C., Bailey, S., 2001. Altitude determination of ultraviolet measurements made by the Student Nitric Oxide Explorer. *J. Geophys. Res.*, *106*(A12), doi:10.1029/2001JD001111.
- Merkel, A. W., Garcia, R. R., Bailey, S. M. and Russel III, J. M., 2008. Observational studies of planetary waves in PMCs and mesospheric temperature measured by SNOE and SABER. *J. Geophys. Res.*, *113*(D14202), doi:10.1029/2007JD009396.
- McPeters, R. D., 1980. The behavior of ozone near the stratopause from two years of BUW observations. *J. Geophys. Res.*, **85**, 4545-4550.
- McPeters, R. D., 1989. Climatology of nitric oxide in the upper stratosphere, mesosphere, and thermosphere: 1976 through 1986. *J. Geophys. Res.*, **104**, 19, 3461-3472.
- Mills, M. J., Toon, O. B., and Thomas, G. E., 2005. Mesospheric Sulfate aerosol layer. *J. Geophys. Res.*, *110*, D24, 208.
- Mohanakumar, K., 2008. Stratosphere Troposphere Interactions – An Introduction. *Springer Science + Business Media B.V.*
- Morris, R. J., Klekociuk, A. R., and Holdsworth, D. A., 2009. Low latitude 2-day planetary wave impact on austral polar mesopaus temperatures: revealed by a January diminution in PMSE above Davis, Antarctica. *Geophys. Res. Lett.*, *36*, L11807.
- Muller, H. G., and Kingsley, S. P., 1974. On the scale sizes of wind systems in the meteor zone. *J. Atmos. Sol.-Terr. Phys.*, *36*, 1851 – 1861.
- National Weather Service, Northern hemisphere cross section showing jetstreams and tropopause elevations, NOAA.
Weblink: <http://www.srh.noaa.gov/jetstream/global/image/jetstream3.jpg>.
- Namboothiri, S. P., Kishore, P., and Igarashi, K., 2002. Observations of the quasi-2-day wave in the mesosphere and lower thermosphere over Yamagawa and Wakkanai. *J. Geophys. Res.*, *107*(D16), 4320, doi:10.1029/2001JD000539.
- Norton, W. A., and Thuburn, J., 1996. The two-day wave in a middle atmosphere GCM. *Geophys. Res. Lett.*, *23*, No. 16, 2113 – 2116.

- Nozawa, S., Iwahashi, H., Brekke, A., Hall, C. M., Meek, C., Manson, A., Oyama, S., Murayama, Y., Fujii, R., 2003. The quasi 2-day wave observed in the polar mesosphere: Comparison of the characteristics observed at Tromsø and Poker Flat. *J. Geophys. Res.*, 108(D24), 4748, doi:10.1029/2002JD003221.
- Patterson, J. D., Armstrong, T. P., Laird, C. M., Detrick, D. L., and Weatherwax, A. T., 2001. Correlation of solar energetic protons and polar cap absorption. *J. Geophys. Res.*, 101, 149 – 163.
- Page, D., and Hirsch, J. G., 1999. From the Sun to the great attractor. *Lecture Notes in Physics, Springer Verlag*.
- Palo, S. E., Forbes, J. M., Zhang, X., Russell III, J. M., and Mlynezak, M. G., 2007. An eastward propagating two-day wave: Evidence for nonlinear planetary wave and tidal coupling in the mesosphere and lower thermosphere. *Geophys. Res. Lett.*, 34, L07807, doi:10.1029/2006GL027728.
- Paton, J., 1964. *Met. Mag.*, 93, 161.
- Perot, K., Hauchecorne, A., Montmessin, F., Bertaux, J.-L., Blanot, L., Dalaudier, F., Fussen, D., and Kyrölä, E., 2010. First climatology of polar mesospheric clouds from GOMOS/ENVISAT stellar occultation instrument. *Atmos. Chem. Phys.*, 10, 2723 – 2735.
- Pidwirny, M., 2006. Forces acting to create wind, *Fundamentals of Physical Geography*, 2nd edition, e-book (<http://www.physicalgeography.net/fundamentals/7n.html>).
- Plane, J. M. C., 2000. The role of sodium bicarbonate in the nucleation of noctilucent clouds. *Ann. Geophys.*, 18(7), 807 – 814.
- Poole, L. M. G., and Harris, T. J., 1995. The propagation of the mesospheric two-day wave in the southern hemisphere. *J. Atmos. Terr. Phys.*, Vol. 57, No. 13, pp. 1661 – 1666.
- Plumb, R., 1983. Baroclinic instability of the summer mesosphere: A mechanism for the 2-day wave? *J. Atmos. Sci.*, 40, 262 – 270.
- Prata, A. J., 1984. The 4-day wave. *J. Atmos. Sci.*, 41, 150 – 155.
- Price, J. C., 1991. Timing of NOAA afternoon passes. *Int. J. Remote Sens.*, 12, 193-198.
- Rahpoe, N., von Savigny, C., DeLand, M., Robert, C., Burrows, J. P., 2010. Impact of Solar Proton Events on Noctilucent Clouds. *J. Atmos. Sol.-Terr. Phys.*, , doi:10.1016/j.jastp.2010.07.017
- Rapp, M., Lübken, F.-J., Mülleman, A., Thomas, G. E., Jensen, E. J., 2002. Small-scale temperature variations in the vicinity of NLC: Experimental and model results. *J. Geophys. Res.*, 107(19), 4329, doi:10.1029/2001JD001241.
- Rapp, M., Lübken, and Blix, T. A., 2003. The role of charged ice particles for the creation of PMSE: A review of recent developments. *Adv. Space Res.*, 31(9), 2033 – 2043.
- Rapp, M., and Thomas, G., 2006. Modeling of the microphysics of mesospheric ice particles: Assessment of current capabilities and basic sensitivities. *J. Atmos. Sol.-Terr. Phys.*, 68, 715 – 744.

- Rapp, M., Thomas, G. E., and Baumgarten, G., 2007. Spectral properties of mesospheric ice clouds: Evidence for non-spherical particles. *J. Atmos. Terr. Phys.*, 71 408 – 423, doi:10.1016/j.jastp.2008.10.015
- Remsberg, E. E., Bhatt, P. P., Deaver, L. A., 2002. Seasonal and longer-term variations in middle atmosphere temperature from HALOE on UARS. *J. Geophys. Res.*, 107(D19), 4411.
- Robert, C., von Savigny, C., Burrows, J. P., Baumgarten, G., 2009. Climatology of noctilucent cloud radii and occurrence frequency using SCIAMACHY. *J. Atmos. Sol.-Terr. Phys.*, 71, 408 – 423, doi:10.1016/j.jastp.2008.10.015
- Robert, C., 2009. Investigation of noctilucent cloud properties and their connection with solar activity. *PhD Thesis*.
- Robert, C., von Savigny, C., Rahpoe, N., Bovensmann, H., Burrows, J. P., DeLand, M., Schwartz, M. J., 2010. First evidence of a 27 day solar signature in noctilucent cloud occurrence frequency. *J. Geophys. Res.*, Vol. 115, D00I12, doi:10.1029/2009JD012359
- Rodgers, C. D., and Prata, A., 1981. Evidence for a traveling 2-day wave in the middle atmosphere. *J. Geophys. Res.*, 86, 9661 – 9664.
- Roedel, W., 1992. Physik unserer Umwelt. Die Atmosphäre. *Springer-Verlag Berlin Heidelberg 1992*.
- Rojas, M., Norton, W., 2007. Amplification of the 2-day wave from mutual interaction of global Rossby-gravity and local modes in the summer mesosphere. *J. Geophys. Res.*, 112, D12114, doi:10.1029/2006JD008084.
- Rossby, C. G., 1940. Planetary flow pattern in the atmosphere. *Q. J. Roy. Met. Soc. Supplement*, 66, 68.
- Rusch, D. W., Thomas, G. E., Jensen, E. J., 1991. Particle size distributions in polar mesospheric clouds derived from Solar Mesospheric Explorer measurements. *J. Geophys. Res.*, 96, 12, 933-12,939.
- Rusch, D. W., Bailey, S. M., Thomas, G. E. and Merkel, A. W., 2008. Seasonal-latitudinal variations of PMC particle size from SME measurements for the northern 1983 season and SNOE measurements for the northern 2000 and southern 2000/2001 seasons. *J. Atmos. Terr. Phys.*, 70(1), 71 – 88.
- Sanahuja, B., and Heras, A., 1992. Evolution and Modeling of Low-Energy Particle Events Associated with Interplanetary Shocks up to 1 AU. *Proc. SOLTIP 1 Symposium, Vol. I*, Liblice, Czechoslovak Acad. Sci., pp. 216 – 227.
- Salby, M. L., 1981. Rossby normal modes in nonuniform background conditions. part II: Equinox and solstice conditions. *J. Atmos. Sci.*, 38, 1827 – 1840.
- Salby, M. L., Callaghan, P. F., 2003. Dynamics of the 2-day wave in a nonlinear model of the middle and upper atmosphere. *J. Geophys. Res.*, 108,(D23), 4713.
- Salby, M. L., Callaghan, P. F., 2008. Interaction of the 2-day wave with solar tides. *J. Geophys. Res.*, 113,(D15), doi:10.1029/2006JD007892.

- Salby, M. L., and Roper, R., 1980. Long-period oscillations in the meteor region. *J. Atmos. Sci.*, *37*, 237 – 244.
- Sackmann, I.-J., Boothroyd, A. I., and Kraemer, K. E., 1993. Our Sun. III. Present and future. *The Astrophys. J.*, *418*, 457 – 468.
- Schwartz, M. J., et al., 2008. Validation of the Aura Microwave Limb Sounder temperature and geopotential height measurements. *J. Geophys. Res.*, *113*(D15), 23, doi:10.1029/2007JD008783.
- Schröder, H., Schmitz, G., 2004. A generation mechanism for the 2-day wave near the stratopause: Mixed barotropic-inertial instability. *J. Geophys. Res.*, *109*, D24116, doi:1029/2004JD005177.
- Seele, C., Hartogh, P., 1999. Water vapor of the polar middle atmosphere: annual variation and summer mesosphere conditions as observed by ground-based microwave spectroscopy. *Geo. Res. Lett.*, *26*, 1517 – 1520.
- Shipman, H. L., 1979. Masses and radii of white-dwarf stars. III – Results for 110 hydrogen-rich and 28 helium-rich stars. *Astrophys. J.*, *228*, 240 – 256. doi:1029/2004JD005177.
- Simmons, D. A. R., and McIntosh, D. H., 1983. An analysis of noctilucent clouds over western Europe. *Meteorol. Mag.*, *112*, 289-298, 1983.
- Solomon, S., Rusch, D. W., Gerard, J.-C., Reid, G. C., and Crutzen, P. J., 1981. The effect of particle precipitation events on the neutral and ion chemistry of the middle atmosphere: II Odd Hydrogen. *Planet. Space Sci.*, Vol. *29*, No. 8, pp. 885 – 892.
- Solomon, S., Rusch, D. W., Reid, G. C., and Thomas, R. J., 1983. Mesospheric ozone depletion during the Solar Proton Event of July 13, 1982 Part II. Comparison between theory and measurements. *Geophys. Res. Lett.*, *10*, 257 – 260.
- Sonnemann, G., and Grygalashvily, M., 2005. Solar Influence on Mesospheric water vapor with impact on NLCs. *J. Atmos. Sol.-Terr. Phys.*, *67*, 177 – 190.
- St. Cyr, O. C, and Webb, D. F., 1991. Activity Associated with Coronal Mass Ejections at Solar Minimum: SMM Observations from 1984 – 1986. *Sol. Phys.*, *136*, 379.
- Steinolfson, R. S., and Hundhausen, A. J., 1990. MHD Intermediate Shock in Coronal Mass Ejections. *J. Geophys. Res.*, *95*, 6389.
- Swider, W., and Keneshea, T. J., 1973. Decrease of ozone and atomic oxygen in the lower mesosphere during a PCA event. *Space Sci.*, *21*, 1969 – 1973.
- Thomas, G. E., McPeters, R. D., Jensen, E. J., 1991. Satellite Observations of Polar Mesospheric Clouds by the Solar Backscattered Ultraviolet Spectral Radiometer: Evidence of a Solar Cycle Dependence. *J. Geophys. Res.*, **96**, D1, 927-939.
- Tsurutani, B. T., Gonzalez, W. D., Tang, F., and Lee, Y. T., 1992. Great Magnetic Storms *Geophys. Res. Lett.*, *19*, 73.
- Twomey, S., 1961. On the deduction of the vertical distribution of ozone by ultraviolet spectral measurements from a satellite. *J. Geophys. Res.*, **66**, 2153-2162.

- von Cossart, G., Fiedler, J., von Zahn, U., 1999. Size distributions of NLC particles as determined from 3-color observations of NLC by ground-based lidar. *Geophys. Res. Lett.*, *26*, 1513 – 1516.
- von Savigny, C., Petelina, S. V., Karlsson, B., Llewellyn, E. J., Degenstein, D. A., Lloyd, N. D., and Burrows, J. P., 2005. Vertical variation of NLC particle sizes retrieved from Odin/OSIRIS limb scattering observations. *Geophys. Res. Lett.*, *32*(L07806).
- von Savigny, C., and Burrows, J. P., 2007. Latitudinal variation of NLC particle radii derived from northern hemisphere SCIAMACHY/Envisat limb measurements. *Adv. Space. Res.*, *40*(6), 765 – 771.
- von Savigny, Sinnhuber, M., Bovensmann, H., Burrows, J. P., Kallenrode, M.-B., and Schwartz, M., 2007a. On the disappearance of noctilucent clouds during the January 2005 solar proton events. *Geophys. Res. Lett.*, *34*(L02805).
- von Savigny, C., Robert, C., Bovensmann, H., Burrows, J. P., Schwartz, M. J., 2007b. Satellite observations of the quasi 5-day wave in noctilucent clouds and mesopause temperatures. *Geophys. Res. Lett.*, *34*, L24808, doi:10.1029/2007GL.
- von Savigny, C., Robert, C., Rahpoe, N., Burrows, J. P., Morris, R., Schwartz, M. J., DeLand, M. T., Petelina, S., Llewellyn, E. J., 2008. Impact of Solar Proton Events on Noctilucent Clouds. *HEPPA workshop, May 28 – 30, 2008, Helsinki*.
- von Zahn, U., von Cossart, G., and Fiedler, J., 1998. Tidal variations of noctilucent clouds measured at 69N latitude by groundbased lidar. *Geophys. Res. Lett.*, *25*(9), 1289 – 1292.
- Verronen, P. T., Rodger, C. J., Clilverd, M. A., Pickett, H. M., and Turunen, E., 2007. Latitudinal extent of the January 2005 solar proton event in the Northern Hemisphere from satellite observations of hydroxyl. *Ann. Geophys.*, *25*, 2203 – 2215.
- Waters, J. W., et al., 2006. The Earth Observing System Microwave Limb Sounder (EOS MLS) on the Aura Satellite. *IEEE Trans. Geosci. Rem. Sens.*, *44*(5), 1075-1092.
- Weeks, L. H., Cuikay, R. S., and Corbin, J. R. L., 1972. Ozone Measurements in the Mesosphere During The Solar Proton Event of 2 November 1969. *J. Atmos. Sci.*, *29*, 1138.
- Wilks, D. S., 2006. *Statistical Methods in the Atmospheric Sciences*, 2nd ed., Elsevier, Burlington, Mass.
- Witt, G., 1969. The nature of noctilucent clouds. *Space Research IX*.
- Wrotny, J. E., Russell III, J. M., 2006. Interhemispheric differences in polar mesospheric clouds observed by the HALOE instrument. *J. Atmos. Sol.-Terr. Phys.*, *68*, 1352 – 1369.
- Wu, S. T., Hu, Y. Q., Nakagawa, Y., and Tandberg-Hanssen, E., 1983. Induced Mass and Wave Motions in the Lower Solar Atmosphere. I. Effects of Shear Motion of Flux Tubes. *Astrophys. J.*, *266*, 866.
- Wu, S. T., Song, M. T., Martens, P. C., and Dryer, M., 1991. Shear-Induced Instability and Arch Filament Eruption: A Magnetohydrodynamic (MHD) Numerical Simulation. *Solar Phys.*, *134*, 353.

Wu, D. L., Hays, P. B., Skinner, W. R., Marshall, A. R., Burrage, M. D., Lieberman, R. S., and Ortland, D. A., 1993. Observations of the quasi-2-day wave from the high resolution Doppler imager on UARS. *Geophys. Res. Lett.*, *20*, 2853 – 2856.

Wu, D. L., Hays, P. B., Skinner, W. R., 1995. A Least-Squares Method for Spectral-Analysis of Space-Time Series. *J. Atmos. Sci.*, *52* (20), 3501 – 3511.

Last words.....

After the 3.219 years at the IUP Bremen, I would like to thank Prof. John Burrows for accepting this project and supporting it throughout all the years. His continuous efforts and visions to the scientific world are well accepted in the global climate research scene. I would recommend for any PhD and Master student his speeches during the seminars which can give a push in the right direction at the right time.

Special and great thanks goes to my advisor PD Christian von Savigny, who is one of the top scientists in our group. His ambition and steady support with remarkable sense for small errors in one's thinking process makes the working easier and comfortable. I learned from him how to deal with difficulties in scientific work and writing a paper and to never give up. I am glad that he had always enough time for my stupid questions. Christian's other students and post-docs comprise a superb working group. My most intense collaboration was with Charles Robert whose clarity, persistence and wit was always helpfull. I would like to thank Matthew DeLand for his support and contribution to the SBUV/2 data set and its maintenance.

I also thank my room mate Vladimir Rozanov, with whom I am sharing the small nest on the 4th S-floor, and I am always happy to exchange my 'lost' Russian words with him. The 12:30 Mensa-Group I thank for the come-together and exchange of news and ideas.

Last but not least I would like to thank my family, my parents Seddiq and Najwa my sister Nisa and my brother Amo. The eternal love of them and their support is priceless. This work would not have been possible without the kindness and patience of my lovely wife Maihan. She was always there for me and if there were a moment that could last for ever it would pass like a minute with her.

Erklärung

Hiermit erkläre ich, dass ich die Arbeit ohne Zuhilfenahme von andere Quellen und Hilfsmittel als die der angegebenen angefertigt habe. Die wörtlich und inhaltlich benutzten Stellen in der Arbeit sind unter Angabe der Referenzquellen kenntlich gemacht worden.

Nabiz Rahpoe

Bremen, 23 December 2010